Design and optimization of vertex detector foils by superplastic forming

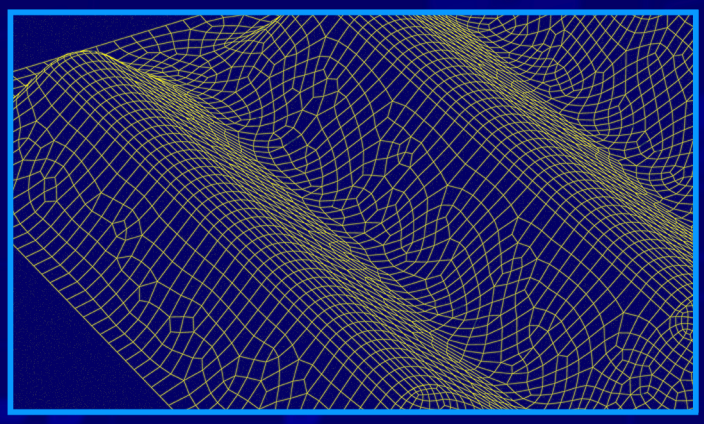

Corijn Snippe

Design and optimization of vertex detector foils by superplastic forming

Corijn Snippe

This work is financially supported by the National Institute for Subatomic Physics (Nikhef) in Amsterdam, and is part of the LHCb Vertex Locator program.

Samenstelling van de promotiecommissie:

voorzitter en secretaris:	
Prof. dr. F. Eising	Universiteit Twente
promotor:	
Prof. dr. ir. J. Huétink	Universiteit Twente
assistent promotor:	
Dr. ir. V.T. Meinders	Universiteit Twente
leden:	
Prof. dr. ir. R. Akkerman	Universiteit Twente
Prof. dr. ing. B. van Eijk	Universiteit Twente / Nikhef Amsterdam
Prof. dr. M.H.M. Merk	Nikhef Amsterdam / VU Amsterdam
Dr. R.D. Wood	University of Swansea, Wales (UK)

ISBN 978-90-8570-723-3

1st Printing February 2011

Keywords: superplasticity, constitutive modeling, aluminum, metal forming

This thesis was prepared with LaTeX by the author and printed by Wöhrmann Print Service, Zutphen, from an electronic document.

DESIGN AND OPTIMIZATION OF VERTEX DETECTOR FOILS BY SUPERPLASTIC FORMING

PROEFSCHRIFT

ter verkrijging van
de graad van doctor aan de Universiteit Twente,
op gezag van de rector magnificus,
prof. dr. H. Brinksma,
volgens besluit van het College voor Promoties
in het openbaar te verdedigen
op woensdag 16 maart 2011 om 15.00 uur

door

Quirin Hendrik Catherin Snippe

geboren op 21 juni 1969
te Maastricht

Dit proefschrift is goedgekeurd door de promotor:
Prof. dr. ir. J. Huétink
en de assistent promotor:
Dr. ir. V.T. Meinders

Contents

Summary

The production of one of the parts in a particle detector, called the RF Foil, has been a very intensive process in the past. The design and production process, which had a trial and error character, led eventually to an RF Foil that met the most important requirement: a sufficient leak tightness value. Since these kinds of foils have to be produced in the future, it is desirable to shorten the development stage with a view to cost reduction. This research project investigates how this part can be optimized with respect to the radiation length. An important limiting factor within this optimization process is the leak tightness of the foil. The intended production method this research will investigate is superplastic forming (SPF). On the one hand, the goal is to use finite element calculations to predict the forming behavior. The leak tightness of the formed foil must also be predicted within these calculations. On the other hand, an optimization strategy is necessary to reduce the radiation length of the RF Foil while maintaining the leak tightness.

The material that will be used throughout this research is ALNOVI-1, a material which is based on AA5083. This material shows optimal superplastic properties at a temperature of 520 °C and an equivalent plastic strain rate of $8.3 \cdot 10^{-4}$ s^{-1}. Different types of experiments have been done to obtain as much information as possible concerning the mechanical behavior of the material.

To determine the uniaxial behavior of the material, tensile experiments have been performed. The first series of tests was intended to determine the optimal temperature at which the highest value of the equivalent plastic strains could be reached. In the second series of tensile experiments, specimens were tested until fracture at different tensile velocities. From these tests, a high strain rate sensitivity was measured. In the third series of tensile experiments, specimens were strained until a predefined value of the tensile force. The results of these tests were used to determine the void volume fraction in the material as a function of the plastic strain.

Free bulge experiments have been performed where circular sheets of ALNOVI-1 were blown. The goal of these experiments was to study the material behavior in a plane stress situation. The application of a backpressure during forming appeared to have a positive effect on the void volume fraction evolution. In turn, this had

a beneficial effect on the maximum attainable plastic strain in the material before failure due to a gas leak. Leak tightness experiments showed that with the application of a 30 bar backpressure, it is possible to attain much higher bulges with the same leak rate value as bulges formed without a backpressure application.

A third type of experiment that has been done is the forming of the same circular sheets within a die. The goal of these experiments was to investigate the frictional behavior between ALNOVI-1 and the die material, AISI 321L. Molykote was used as a lubricant, which is a mixture of molybdenum sulphide and graphite. The complete setup of the bulge experiments was an in-house design, where it was possible to control the pressures on both sides of the sheet as a function of time. The shape of the pressure-time profiles was such that a predefined target plastic strain rate in the material would not be exceeded.

The results of all experiments have been used to develop a user-defined material to be used in ABAQUS. With this phenomenological constitutive model, it is possible to simulate the forming behavior of ALNOVI-1 as a function of a set of parameters. These parameters describe the uniaxial behavior in terms of:

- an initial flow stress which is dependent on the equivalent plastic strain rate;
- a hardening stress due to an increasing equivalent plastic strain;
- void volume fraction evolution in the material as a function of the equivalent plastic strain. These form a bilinear relationship with each other;
- a multiplication factor (between 0 and 1) to account for the reduction in stress due to the void volume fraction in the material.

The behavior in a plane stress situation is described by the Hosford flow criterion with exponent $n = 8$, and taking into account the Lankford strain ratio R. The material behavior also takes into account the influence of a hydrostatic pressure during forming. The leak rate of the formed sheet can be expressed in terms of the void volume fraction and the resulting sheet thickness.

This constitutive model has been used to perform forming analyses of the RF Foil in view of the optimization of this foil. To perform an optimization procedure, the following ingredients are necessary to solve the problem:

- minimization of the objective function. In this project, this means a minimization of the radiation length of the product;
- the leak tightness is the most important constraint. Also some mechanical constraints were applied, such as an upper value for the stresses and elastic deformations in the material due to an overpressure in the operating conditions (room temperature). A minimum value for the first natural frequency was also applied;

- determination of the design variables and their ranges. To limit the amount of design variables, a parameterization of the current design is necessary.

Within the range of the design variable limits, a metamodeling algorithm using the Response Surface Methodology and Kriging was used to find the global optimum. The current RF Foil has a radiation length of 8.2% X_0, the optimized RF Foil has a radiation length of 4.6% X_0. This means that the optimized RF Foil has a radiation length which is 43% lower than the radiation length of the current RF Foil. Hence, the objective of this research was met, the optimized RF Foil is a better design than the current one.

Samenvatting

De produktie van een van de onderdelen in een deeltjesdetector, het zogeheten RF-folie, is in het verleden een zeer arbeidsintensief proces geweest. Door het trial-and-error-karakter van het ontwerp- en produktieproces is uiteindelijk een RF-folie geproduceerd dat aan de belangrijkste eis voldoet: een goede lekdichtheid. In het geval er in de toekomst dit soort folies geproduceerd moeten worden, moet dit ontwikkelingstraject verkort worden met het oog op kostenbesparing. In dit project wordt onderzocht hoe dit onderdeel geoptimaliseerd kan worden met betrekking tot de stralingslengte, waarbij de lekdichtheid een belangrijke limiterende factor is. De beoogde produktiemethode die hier wordt onderzocht is die van het superplastisch vervormen (SPF). Doel is enerzijds om het vervormingsgedrag te kunnen voorspellen aan de hand van eindige elementenanalyses en daarmee ook een voorspelling te kunnen doen omtrent de lekdichtheid van het gevormde folie. Anderzijds is het de bedoeling een optimalisatiestrategie te ontwikkelen om de stralingslengte van het RF-folie te verlagen met behoud van de lekdichtheid.

Het materiaal dat gebruikt wordt voor dit onderzoek is ALNOVI-1, een materiaal gebaseerd op AA5083. Dit materiaal vertoont optimale superplastische eigenschappen bij een temperatuur van 520 °C en een equivalente plastische reksnelheid van $8.3{\cdot}10^{-4}$ s^{-1}. Verschillende typen experimenten zijn uitgevoerd om een zo volledig mogelijk beeld te krijgen van het mechanisch gedrag van dit materiaal.

Om het uniaxiale gedrag van het materiaal te bepalen zijn trekproeven uitgevoerd. De eerste serie proeven hiervan had als doel om de temperatuur te bepalen waarbij de hoogste plastische rekken haalbaar zijn alvorens het materiaal faalt door breuk. Bij de tweede serie trekproeven zijn proefstukken bij deze optimale temperatuur getest tot breuk, bij verschillende treksnelheden. Uit deze proeven bleek onder andere een hoge mate van reksnelheidsafhankelijkheid. De derde serie trekproeven bestond uit experimenten waarbij de proefstukken werden getrokken tot een vooraf ingestelde waarde van de trekkracht. Aan de hand van deze proeven is de mate van holtevorming in het materiaal bepaald als functie van de plastische rek.

Blaasvormtesten zijn uitgevoerd waarbij cirkelvormige plaatjes ALNOVI-1 onder overdruk tot een bolle vorm zijn geblazen. Deze experimenten hadden als doel om het materiaalgedrag te bestuderen onder een vlakspanningstoestand. Het

aanleggen van een hydrostatische druk tijdens het vervormingsproces bleek een gunstige uitwerking te hebben op het holtevormingsgedrag, en daarmee op de maximaal haalbare plastische rek in het materiaal alvorens falen optreedt in de vorm van een gaslek. Gasdichtheidsproeven hebben aangetoond dat onder invloed van een hydrostatische druk van 30 bar het mogelijk is om blaasvormen te maken die een stuk verder vervormd zijn bij eenzelfde lekdichtheid dan zonder deze druk.

Een derde type experiment dat is uitgevoerd is het blaasvormen van dezelfde cirkelvormige plaatjes in een mal. Deze proeven hadden als doel om het wrijvingsgedrag te onderzoeken tussen ALNOVI-1 en de mal, gemaakt van AISI 321L. Het gebruikte smeermiddel om deze wrijving te bereiken was Molykote, een mengsel van molybdeensulfide en grafiet.

Voor alle blaastesten is gebruik gemaakt van een zelf ontworpen proefopstelling waarbij het mogelijk was om de vervormingsdruk op de plaat te variëren als functie van de tijd. De druk-tijdprofielen hiervoor waren zodanig dat tijdens dit vervormingsproces een vooraf bepaald doelwaarde voor de equivalente plastische reksnelheid nergens in het materiaal werd overschreden.

De resultaten van alle proeven zijn verwerkt in een *User-defined material model* in ABAQUS. Met dit fenomenologische materiaalmodel is het mogelijk om het vervormingsgedrag van ALNOVI-1 te simuleren als functie van een set parameters. Deze parameters beschrijven het uniaxiale gedrag in termen van:

- een initiële vloeispanning die afhankelijk is van de equivalente plastische reksnelheid;
- een spanningstoename als gevolg van een toenemende equivalente plastische rek;
- holtevorming in het materiaal als functie van de equivalente plastische rek. Dit is een bilineaire relatie;
- een vermenigvuldigingsfactor (tussen 0 en 1) die de spanningsreductie aangeeft als gevolg van holtevorming in het materiaal.

Het gedrag onder een vlakspanningstoestand is beschreven middels het Hosford vloeicriterium met exponent $n = 8$, met inachtneming van de rekverhouding R. Tevens is het gedrag beschreven onder invloed van een hydrostatische druk. De lekdichtheid van het materiaal kan worden uitgedrukt in termen van de holtevorming en de resulterende dikte van de plaat.

Dit materiaalmodel is gebruikt om vervormingsanalyses te doen met betrekking tot het RF-folie met het oog op optimalisatie van dit folie. Om een optimalisatieprocedure uit te voeren is het probleem beschreven in de volgende termen:

- minimalisatie van de doelfunctie, in dit geval houdt dit een minimalisatie van de stralingslengte van het produkt in;

- de lekdichtheid is de belangrijkste randvoorwaarde. Daarnaast zijn mechanische eigenschappen vereist, zoals een grenswaarde voor de spanningen en elastische vervormingen in het materiaal als gevolg van een overdruk op het folie in de gebruiksomstandigheden (kamertemperatuur). Tevens is een minimale waarde vereist voor de eerste eigenfrequentie van het folie;

- aangeven van de ontwerpvariabelen met elk hun bereik. Hiervoor is een parametrisatie van het huidige ontwerp noodzakelijk.

Binnen het bereik van de ontwerpvariabelen wordt een metamodelleringsalgoritme (gebruikmakend van de Response Surface Methodolgy en Kriging) gebruikt om het globale optimum te vinden. Het huidige folie heeft een stralingslengte van 8.2% X_0, het geoptimaliseerde RF-folie heeft een stralingslengte van 4.6% X_0. Dit betekent dat het geoptimaliseerde folie een stralingslengte heeft die 43% lager ligt dan die van het huidige folie. Daarmee kan dus gezegd worden dat het doel van dit onderzoek is behaald, het geoptimaliseerde RF-folie is beter dan het huidige folie.

Nomenclature

Roman symbols

A	atomic weight
A_i	area of surface i
$\mathbf{C}$	elasticity tensor (second-order)
${}^4\mathbf{C}$	elasticity tensor (fourth-order)
$\mathbf{D}$	rate-of-deformation tensor
d	grain size (Chapter 2)
d	displacement
d_c	channel diameter
E	Young's modulus
F	force
F_j	view factor
F_{obj}	objective function value
G	shear modulus
g_i	inequality constraint i
h_j	equality constraint j
I_1, I_2	stress invariants
k	Boltzmann constant
k_s	stress concentration factor
L	leak rate
l	(effective/channel) length
M	grain boundary mobility
m	strain rate sensitivity
N_A	Avogadro constant
n	Hosford exponent
p	pressure
p_h	hydrostatic pressure
Q	fluid flow rate
Q_n	quality factor
R_{s}	shunt impedance
R	Lankford strain ratio

R_0, R_{45}, R_{90}	direction dependent strain ratios
$\bar{R}$	average strain ratio
ΔR	strain ratio sensitivity
R^2	coefficient of multiple determination
R^2_{adj}	adjusted coefficient of multiple determination
$\mathbf{r}$	vector of residuals
S	distance
s_{ij}	deviatoric stress components
$\mathbf{s}$	deviatoric stress tensor
T	temperature
t	thickness
t_{s}	time (in seconds)
$\hat{t}$	average traversed path
v	drawing velocity
X_0	radiation length
W	void aspect ratio
Z	atomic number

Greek symbols

α	electromagnetic interaction constant
γ_{xy}	engineering shear strain
$\boldsymbol{\varepsilon}$	strain vector
$\dot{\boldsymbol{\varepsilon}}$	strain rate vector
$\bar{\varepsilon}^{\text{p}}$	equivalent plastic strain
$\dot{\bar{\varepsilon}}^{\text{p}}$	equivalent plastic strain rate
ε_{tr}	transition strain
η	dynamic viscosity
κ	loss factor
λ	stretch
$\dot{\lambda}$	plastic multiplier
ν	Poisson's ratio
ξ, ξ_{v}	void volume fraction
ξ_{a}	void area fraction
Σ_{h}	hydrostatic stress
σ_{e}	equivalent stress
σ_{f}	macroscopic flow stress
σ_{m}	matrix material yield stress
σ_{surf}	grain boundary energy density
σ_{y}	yield stress
σ_1, σ_2, σ_3	principal stress components
$\Delta\sigma$	saturation stress

$\boldsymbol{\sigma}$	stress vector
$\boldsymbol{\sigma}^{\mathrm{tr}}$	trial stress vector
$\tau_{\max}$	maximum shear stress
ϕ	flow function value
Ω	vacancy volume
ω	radial frequency

Abbreviations

ARB	Accumulative Roll Bonding
BP	Backpressure
CERN	European Organization for Nuclear Research
CGBS	Cooperative Grain Boundary Sliding
CP	Charge Parity
CTE	Coefficient of Thermal Expansion
DOE	Design of Experiments
ECA	Equal Channel Angular Extrusion
EM	Electro-Magnetic
FE(M)	Finite Element (Method)
GBS	Grain Boundary Sliding
GEANT	GEometry ANd Tracking
LHC	Large Hadron Collider
LHCb	Large Hadron Collider B detector
RF	Radio Frequency
RMSE	Root Mean Square Error
RSM	Response Surface Methodology
SPF	Superplastic Forming
UMAT	User-Defined Material Model
VeLo	Vertex Locator

1. Introduction

At the end of 2009, the Large Hadron Collider (LHC) particle accelerator at the European Organization for Nuclear Research (CERN) in Geneva was started up, being the world's largest scientific experiment at that moment. In the upcoming years research will be carried out in the field of subatomic physics, involving high precision particle trajectory measurements. This scientific experiment aims at a better understanding of the subatomic structure of matter and its interactions.

One of the four detectors positioned in the accelerator is the LHCb experiment. The main goal of this experiment is to understand why there exists a large asymmetry between the existence of matter and antimatter. A necessary ingredient to explain this asymmetry is the existence of so-called CP violation, where CP stands for charge and parity. To do this, LHCb aims at measuring the decay time of particles which show a relatively high amount of CP violation, so-called B mesons and anti-B mesons. These are unstable particles that are, among others, products of proton-proton collisions within the accelerator.

Before these B and anti-B mesons decay into lighter particles, they travel up to a few centimeters. These newly created particles often decay in more stable particles. One of the functions of a detector is to determine the production and decay point of a particle, i.e. a vertex. To make a precise measurement, a piece of detecting equipment has therefore to be situated close to the beam line. The principle of vertex detection is described in Section 1.1. Some physical phenomena related to the design of parts used in a particle detector are explained in Section 1.2. In the case of the LHCb experiment, the detector covered in this research is called a Vertex Locator (VeLo), which is described in Section 1.3. This detector consists of a set of 23 silicon strip detectors on both sides of the beam line situated behind each other, and perpendicular to the accelerator beam line, as shown in Figure 1.1. In this figure, an RF Box is visible, which is a thin-walled aluminum box, containing these silicon strip detectors. The main problems that arose during the manufacturing of the RF Box are described in Section 1.4. The biggest challenge was to produce a gas leak-tight construction, which led to many problems. A project description with the goal to solve these problems is presented in that section. The set of requirements is covered in Section 1.5. A description of the methods followed in this project is explained in Section 1.6. The general solution for the structure surrounding the

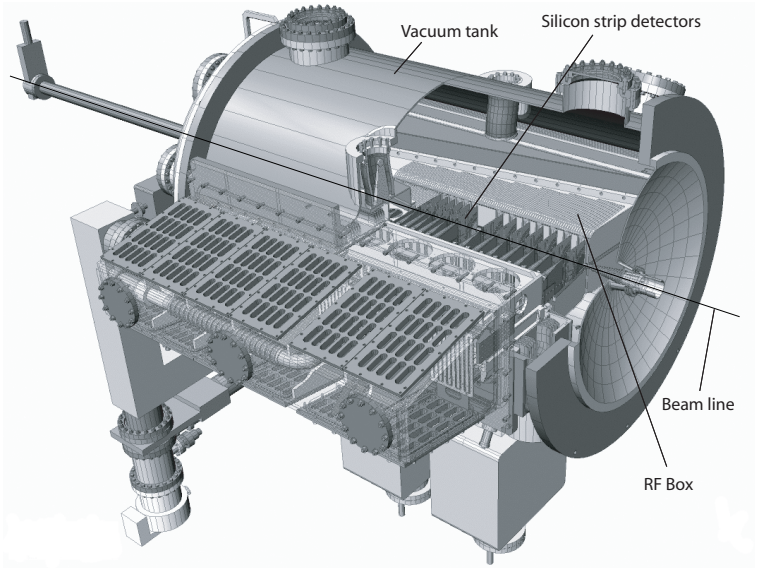

Figure 1.1: Placement of the silicon strip detectors in a vacuum tank, surrounding the accelerator beam.

detectors is called an *RF Shield*, RF standing for Radio Frequency. The solution chosen in the current design is a box, called the (already mentioned) *RF Box*. The top sheet of this box, which is closest to the beam line, is the *RF Foil*.

1.1 Vertex detection

The main purpose of the silicon strip detectors, see Figure 1.2, is to determine the originating point (vertex) of a traversing particle. This origin can be the interaction point of the initial collision or the decay point of an unstable particle that was created in the collision. This decay point can be reconstructed with these detectors, provided that a sufficient amount of points was measured where the particle traversed the detectors. This section focuses on the basic physics concepts (CP violation) behind the phenomena to be measured in the LHCb detector. Also, the method of vertex reconstruction will be described here.

1.1.1 Basics of CP violation

Each subatomic particle has its own corresponding antiparticle, which usually has either identical, or opposite properties (quantum numbers). For instance, the

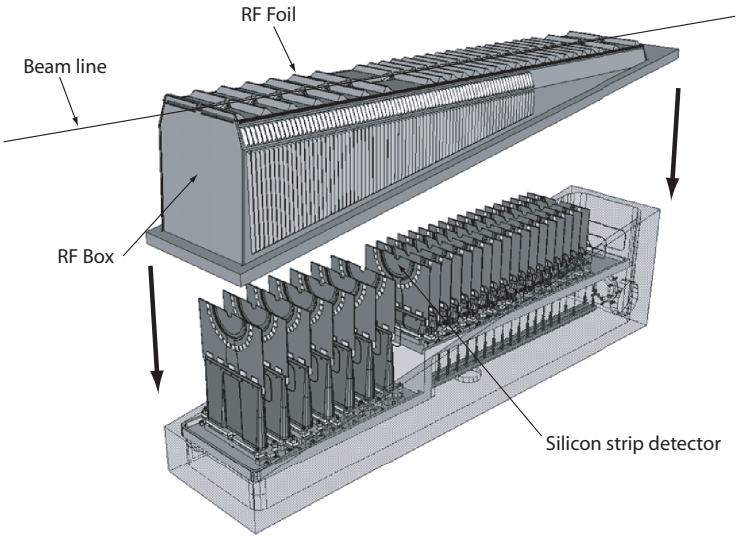

Figure 1.2: Placement of one row of silicon strip detectors within the RF Box.

charge of the antiparticle is always the opposite of the charge of the corresponding particle, but the mass of both particle and antiparticle is the same. The antiparticle of the electron, which has one unit negative charge, has one unit positive charge and is called an anti-electron or *positron*, but both have the same mass. It is to be expected that both particle and antiparticle also obey either the same or mirrored physical laws.

A mirrored particle is called parity or P transformed with respect to the original particle. The transformation involves the change of a right-handed coordinate system into a left handed one. This can be imagined by mirroring a particle two times: a vertical-mirror deflection followed by a top-bottom switch. A charge or C transformation changes the sign of the electric charge of the particle. If both C and P transformations act onto a particle, then this would lead to the corresponding antiparticle, which should have identical properties to those of the particle.

In the 1960s, experiments with particles called kaons showed that occasionally particles behave differently than their CP mirrored particles, the anti-kaons. Both particles can decay the same way in two other particles, but experiments show that the probability for these kaons and anti-kaons to decay were slightly different. This meant that particles and antiparticles can behave or decay differently. This phenomenon is called *CP violation*, see for instance [84], and this is thought to be the main reason why there is an abundance of matter in the universe above

antimatter.

To find the underlying mechanism for this phenomenon to occur, experiments will be performed with the LHCb detector which studies the CP violation in B-mesons. These particles are largely produced in proton-proton colliders, such as the LHC, and it is expected that these mesons show a larger CP violation effect than kaons. By reconstructing the decay point of the B-mesons and its antiparticles, further proof and quantization of CP violation is then possible. The reconstruction of these decay points is done using the LHCb Vertex Locator.

1.1.2 Vertex reconstruction

In order to trace the particles coming from a collision between two accelerated particles, a detector has to be placed around the interaction point. A particle detector generally consists of a layered structure of different kinds of detectors, since it is not possible to detect all sorts of particles with one single detector. Each layer has its own characteristics and measurement accuracy, which is not only able to distinguish the particle type, but can also be used to measure the particle momentum and/or charge.

In semiconductor materials like silicon, the energy required to create an electron-hole pair is very low, about 3 eV. Semiconductor detectors are typically built out of 20 to 50 μm wide and 300 μm thin silicon strips or pixels bonded on a hybrid (a low thickness avoids multiple scattering). Traversing elementary charged particles of high energy can easily create tens of thousands electron-hole pairs to obtain a signal. A stack of silicon strip detectors can then be used to determine the trajectories of charged particles to a high degree of accuracy. Therefore they are used to detect whether a particle originates from the initial collision point or from a secondary point, (i.e. a *vertex*, depending on other particles emerging from the same point which are measured at the same time). This secondary point can be the originating point of a decay product, and is then a measure for the lifetime of the decayed particle.

1.2 Physical phenomena

Besides the physical phenomenon of CP violation, which has already been discussed, two other phenomena will be covered here, because they both have an influence on the design of the RF Shield. The first one is the so-called *multiple scattering*, which is related to the fact that charged particles deviate from their trajectory inside a material, because of the electro-magnetic interaction with the charged particles in this material. All these summed interactions influence the trajectory of the traveling particle through the detector, which in its turn influences the physical particle measurement in terms of kinetic energy and position.

The amount of energy loss is expressed in a term called radiation length and is a material and geometrical property.

The other physical aspect which influences the design of the RF Shield is wake field suppression. In the LHC, protons are accelerated; a consequence is that in the wall of the beam pipe, particles with opposite charge (electrons) will follow the accelerated proton bunches. If this cloud of mirror charge electrons cannot follow the corresponding proton bunch closely enough, the next proton bunch will be influenced, thereby losing part of its energy. This can happen if the electrons cannot travel straight ahead through the beam pipe, but are deviated from their path. Deviated charged particles give off radiation; this is called a wake field.

1.2.1 Radiation length

In order to be detected, an object must leave a trace inside matter as proof of its presence. This means that this particle must leave some energy in its wake, decreasing the kinetic energy of the particle itself. To accurately measure all the desired properties of this particle, the deposited energy must be low (or predictable) compared to its own energy in order not to disturb the particle trajectory too much. At very high energies, above 100 MeV (which is the case in LHC), charged particles traveling in matter lose energy. These particles are accelerated and decelerated in matter because of the electromagnetic interaction with the atomic magnetic fields. This energy loss as function of the traveling length through the matter is predictable, and can therefore be corrected for within the measurements. Electrons, which are very light charged particles, suffer in addition from a phenomenon called *bremsstrahlung* ('brake radiation'). These electrons also give off energy by radiating electromagnetic waves as bremsstrahlung photons.

Bremsstrahlung is not predictable. When a charged particle travels through matter, the trajectory will deviate from the original trajectory, because charged particles inside this matter will disturb the traversing charged particle. Each time this charged particle passes a charged particle inside the traversed matter, single scattering will occur. The sum of all the single scatterings inside the material is the amount of multiple scattering. Therefore, the total amount of traversed matter should be as low as possible. Both the effects of bremsstrahlung and multiple scattering are covered in the *radiation length* value of a material.

This radiation length is dependent on some properties of the material and of the radius of the electron, r_e, having a value of 2.818 fm. The magnetic fields inside the material are dependent on the atomic number Z, which is an indicator of charge, and the atomic weight A, which is an indicator of volume. Also the coupling constant for the electromagnetic interaction, α (equal to 1/137), is involved in this relationship. There are many empirical laws derived from these basic properties, but a few empirical formulas, developed by data fit, are common. The one which

Table 1.1: Radiation length of some materials.

Material	Symbol	Z	A	X_0 g/cm^2	X_0 cm
Beryllium	Be	4	9.012	65.19	35.28
Carbon	C	6	12.01	42.70	18.8
Aluminum	Al	13	26.98	24.01	8.9
Titanium	Ti	22	47.87	16.17	3.56
Iron	Fe	26	55.85	13.84	1.76
Copper	Cu	29	63.55	12.86	1.43
Lead	Pb	82	207.2	6.37	0.56

gives the best results is [27]

$$\frac{1}{X_0} = 4\alpha r_e^2 \frac{N_A}{A}\big(Z(Z+1)\frac{\ln 287}{Z^{\frac{1}{2}}}\big) \tag{1.1}$$

in which N_A is the Avogadro Constant, which has a value of $6.022{\cdot}10^{23}\text{mol}^{-1}$. According to this equation, the dimensions of X_0 are mass per length squared. Dividing this number by the density of the material results in a length dimension. Both numbers are designated with the term 'radiation length' and both are often represented by the same symbol X_0, so it is always necessary to specify the units.

Table 1.1 shows the radiation length for some constructing materials. It is common in particle physics to express the radiation length using the length dimension cm. Sometimes the radiation length is chosen unitless (or in a percentage), meaning the decay probability of an electron through a certain amount of matter. So a material thickness equal to the corresponding lengths shown in this table has a radiation length, expressed as a probability, of $1 - 1/e$, which is about 63.2 %. In constructing detector parts, an important rule is that in general, materials must be chosen with a large X_0 in order to let the electrons traverse the material without an unacceptable disturbance. In that case, the detector part contributes only to a small percentage of X_0. The radiation length of a detector part becomes more important if the distance to the interaction point decreases, because the view angle increases with decreasing distance, and thus the chance of traversing this part increases. This means that a thin foil close to the interaction point covering the whole view from this point performs worse with respect to radiation length than, say, an M12 bolt at several meters distance. Particle physics deals much about statistics, the chance that this bolt is traversed by an electron is very low, compared to the almost 100% chance that the foil will be traversed. Spreading out detector parts over the whole view angle is a good approximation of the importance of this part with respect to radiation length.

1.2.2 Wake fields

If a bunch of charged particles moves along a piece of material, mirror currents with the opposite charge will start to appear in this material. This is constantly the case in the beam pipe of LHC. These mirror currents move just behind the bunch, but will not influence the next bunch of particles. However, if geometrical obstacles are present, the mirror current cannot follow the original particle bunch, because the path to travel will become longer with each deviation from the beam path [6]. These mirror currents then create electro-magnetic fields, called *wake fields*, which have to be suppressed because of two main reasons:

- wake fields can damage the environment by heating;
- wake fields degrade the next bunches in the beam, because of the generated EM fields.

For these reasons, besides some other reasons not dealing with wake field suppression, detector modules may not be placed inside the beam vacuum.

The energy of a wake field is the same as the energy loss of the beam, which is expressed by using a longitudinal loss factor $\kappa_{\parallel}$. This factor is dependent on the distance from the beam to the surrounding structure and on the charge distribution in the bunch, and has to be solved numerically in case of obstacles. This loss factor is then used in an expression which can be interpreted as an extra impedance on the bunch, the *shunt impedance* R_{s}, expressed in the frequency domain [7]

$$R_{\mathrm{s}} = 2\kappa_{\parallel n}\frac{Q_n}{\omega_n} \quad \Omega \tag{1.2}$$

in which $\kappa_{\parallel n}$ is the loss factor for eigenmode n with frequency ω_n and Q_n is a quality factor dependent on the geometry of the cavity.

1.3 LHCb Vertex Locator

The main function of the structural parts in a particle detector is to hold all the detection devices in place and keep them in good condition. To avoid internal stresses as much as possible, it is frequently desirable to ensure that that supporting constructions are kinematically supported, i.e. there are no redundant degrees of freedom in the structure. This is not only to make up for manufacturing tolerances, but also to take into account occasional temperature differences as time progresses during operation.

The Vertex Locator in the LHCb detector consists of two rows of 23 silicon strip detectors, each row situated on either side of the accelerator beam. These rows of strip detectors are placed within a vacuum tank, as was shown in Figure 1.1.

The vacuum space in which the detector rows are situated is separated from the accelerator beam vacuum by means of a thin aluminum shield, the RF Shield. This shield has three main functions:

- it protects the beam pipe vacuum against pollution from the detector vacuum, caused by outgassing of the detector hybrids;
- it serves as a wake field suppressor, see Section 1.2.2;
- it protects the sensors against the high EM frequency in the RF spectrum at which the proton bunches pass by (40 MHz), hence the abbreviation 'RF' in the names 'RF Shield', 'RF Box' and 'RF Foil'.

1.3.1 Mechanical construction

A picture of the two RF Boxes is shown in Figure 1.3(a) [40]. In the final setup each box will contain one row of 23 silicon strip detectors. The two rows are shifted with respect to each other in the direction of the beam, so these rows can then be situated such that the detectors partly overlap, see Figure 1.3(b) for a cross section of this setup. The two RF Boxes were designed in a way that they each cover one row of detectors, hence their wave-like structure. The reason for overlapping of the detectors is that in this way all (charged) particles emerging from a collision will be detected. In addition, the overlapping detectors provide a means to determine their relative alignment.

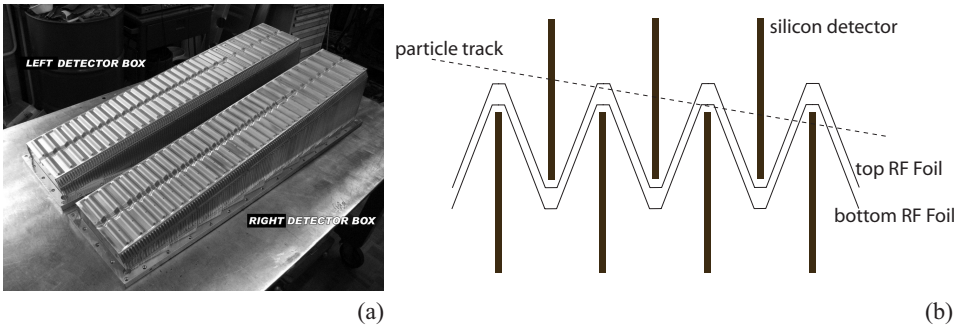

Figure 1.3: (a) Two RF Boxes (left and right) which have to cover both rows of silicon detectors; (b) Cross section view showing the necessity of the wave-like structure of the RF Boxes.

The RF Boxes are made from an aluminum based on AA 5083, an Al-Mg alloy. Sheets of this material that were used for the manufacturing of the RF Foil, had

an initial thickness of 0.3 mm. These sheets were heated up to a temperature between 315 and 350 °C, then gas pressure was applied such that each 15 minutes the pressure was instantaneously increased by 1 bar, until a value of 12 bar was reached. Subsequently, the pressure was increased instantaneously until a value of 20 bar, which was held for one hour before the formed sheet was taken out of the die.

Besides the top foil, the side foils were also manufactured in this way. The particles to be measured always cross the top foil first one ore more times before the detectors are hit. This means that the top foil construction is critical in terms of radiation length. The side walls of the RF Box are only hit just after the detectors are hit, so the construction in terms of radiation length is less critical. The five foils are connected to each other by a welding procedure.

1.3.2 Properties of the RF Box

The dimensions of the RF Box are presented in Figure 1.4 [40]. The RF Foil, which is the top sheet of the RF Box, measures 1120 by 200 mm.

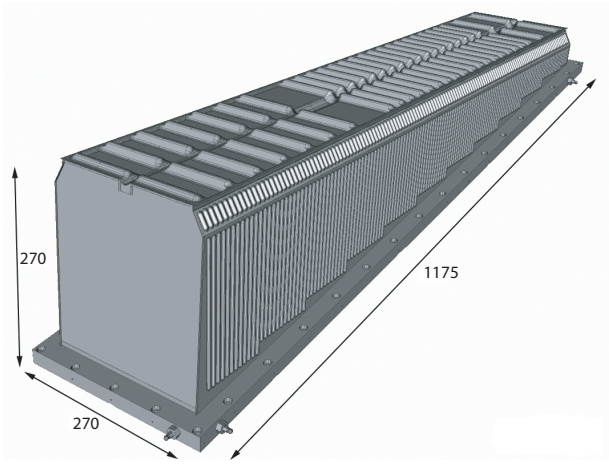

Figure 1.4: Dimensioning of the RF Box.

Two main properties of the RF Box, and in particular the RF Foil, are defined in terms of the wake field suppression and the radiation length. Wake fields are suppressed by the Toblerone-like shape of the RF Foil, the corrugation depth of the wave structure is less than 20 mm [8], which is known to result in a sufficient wake field suppression.

The total radiation length of the Vertex Locator is 19% X_0 [49], this value means that an electron has a probability of 19% that it will decay, and so will not be detected in the detector parts outside the Vertex Locator. Almost half (8.2% X_0) of this probability is consumed by the RF Foil. Optimizing this foil with respect to radiation length can improve the detection accuracy considerably. In the final product, the RF Foil thickness varies between 0.17 mm in the tops of the corrugations and 0.3 mm in the zones where there is not much deformation. The average thickness of the current product is about 0.25 mm. For the upgrade of the Vertex Locator it is desirable that a thinner RF Foil can be used to improve the radiation length. A thinner foil has a higher chance of showing a gas leak which is too high for the application. The leak can be measured globally with a leak tester, local measurements are possible with a so-called sniffer.

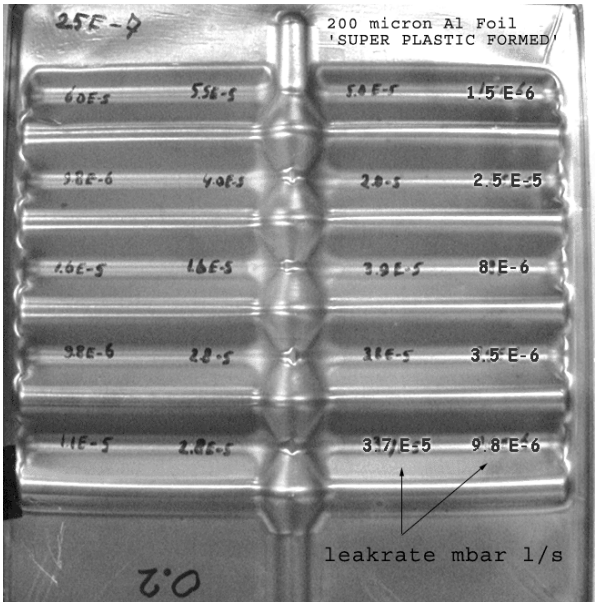

Figure 1.5: Local leak values of a part of the RF Foil.

Leak results from part of a formed sheet are presented in Figure 1.5. The values are expressed in mbar·l/s. The dimension mbar·l is a value for the amount of helium which flows through the sheet per time unit. The global leak rate is dependent on the helium pressure difference between both sides of the sheet and the geometry. The maximum allowable leak rate at an overpressure of 25 mbar helium is $1{\cdot}10^{-8}$ mbar·l/s, so the sheet tested here has an unacceptably high leak value.

In normal operation conditions, the pressure difference between the two sides of the RF Foil is less than 1 mbar. Under the load of this pressure difference, the deflection of the RF Foil may not exceed 1 mm, since both RF Foils may not come into contact with each other. It is calculated that the shield will show irreversible deformation at a pressure difference of 17 mbar [14], which is considered sufficient for this design. It was tested that in case of an emergency, the maximum pressure difference will be 6 mbar, before an overpressure valve opens. This pressure only occurs in case of a sudden air inlet into the RF Box. Further, it is of crucial importance that the first natural frequency of the RF Box is high enough to avoid resonance at external transient inputs from moving parts, such as rotating parts of a pump. The first natural frequency of the current RF Box is calculated at 107 Hz [14], which is high enough to avoid resonating with the input frequencies. It is a general rule that the first resonance frequency is always higher than 50 Hz.

1.4 Problem description

Together with the Vertex Locator, an RF Box is integrated which separates the vacuum, in which the silicon detectors are present, from the beam pipe vacuum. This shield serves two main purposes. Firstly, a boundary is necessary between the two vacua to prevent the occurrence of outgassing from the silicon detectors into the beam pipe vacuum. A vitally important point that has to be mentioned in this context is that this shield has to prevent a gas leak between these two vacua from arising under any circumstances whatsoever. Secondly, this shield should suppress wake fields as much as possible, as was explained in Section 1.2.2. It is important that the electric conductance of the beam pipe itself may not be interrupted, this shield therefore also has the function of a surrogate beam pipe section.

1.4.1 Project motivation

The shield is manufactured by means of Hot Gas Forming, a process where a heated thin sheet of aluminum is pressed into a one-sided die by means of an increasing gas pressure. This has been mainly a lengthy trial-and-error process for several years in terms of material type, forming temperature, and gas pressure. This process resulted in a product which more or less meets the requirement of leak-tightness. The shield has been optimized mainly on the run, solving forming problems on this trial-and-error basis.

Because the shield is positioned very close to the interaction point, it has a very wide view angle, almost 100%, as seen from this point. This means that this shield consumes a major part of the radiation length of the LHCb detector, a phenomenon which was explained in Section 1.2.1. In summary, optimizing with respect to this quantity means in general a mass minimization problem.

Accurate vertex detection is expected to be necessary also in future detectors, requiring a similar protection shield. It would then be advantageous if the design process can be reduced significantly by simulating the forming process of the shield together with an optimization procedure with respect to the radiation length quantity.

It is known that a forming process called *Superplastic Forming* (SPF) can be advantageous in cases of low series production where high plastic strains are to be expected. Since only two RF Shields are necessary inside the particle detector, superplastic forming seems a highly attractive manufacturing method for these shields. It is not only to be expected that in the future more of these shields are to be made for future particle detectors, but also for an upgrade of the LHCb Vertex Locator. Combining this manufacturing process with a means of predicting leak instead of a trial-and-error production, this may lead to a better, optimized RF Box, produced at lower costs.

1.4.2 Project goal

In order to evaluate the design numerically, simulating the actual forming process of superplastic forming can reduce the development time significantly. Materials which are designated as superplastic only behave this way in a very narrow region of temperature and strain rate. Accurate material data concerning superplasticity are very cumbersome to obtain, either from the manufacturer (which generally does not even have these data) or from experiments. A well-designed method has to be found to test some materials in their superplastic regime and fit the results to a physical or phenomenological material model, in order to obtain an accurate input for the forming simulations.

In order to incorporate a method to predict the leak rate of a superplastically formed product, leak rate measuring experiments have to be carried out on formed specimens. The results of these measurements are used in the model to make leak rate predictions of formed RF Boxes.

The shield is situated close to the collision point, also called the interaction point, in the accelerator beam. This means that this part of the detector consumes a relatively large part of the radiation length. This relative radiation length X_0 is a function of two variables. Firstly, the geometry is important, in terms of a path length traversed by a particle through a piece of material. Decreasing wall thickness is beneficial in terms of radiation length. On the other hand, a lower wall thickness can be a disadvantage in terms of leak rate. Secondly, the material type determines the radiation length, see Section 1.2.1, which covers the physical phenomena radiation length and wake field suppression.

The goals of this project are to predict the leak rate of a superplastically formed product and to calculate its radiation length. With this information, an optimization method can be set up in order to develop better RF Shields: a formed sheet having a low relative radiation length which is gas leak-tight.

1.5 Requirements

The design of RF Foils, and the one of the LHCb Vertex Locator in particular, is restricted to a set of constraints of which the wake field suppression has already been mentioned. The constraint which will have the main focus in this project is the leak-tightness of the formed sheet. This means that the leak should be accurately predicted by simulation techniques. Besides this important requirement, another demand is that the wake field suppression is sufficient enough that beam pollution will not take place. Furthermore, as mentioned in the previous section, some mechanical constraints must be met in terms of deformation, damage and natural frequency. These constraints must be met during the optimization procedure in which the percentual radiation length must be minimized. A method must be developed to determine the radiation length of a formed sheet.

1.5.1 Leak requirement

In the case of superplastic materials, internal voids start to arise inside the material upon deformation. These voids grow if the applied plastic strain increases, followed by a process of coalescence between the voids. Void initiation will not lead directly to leak, but if the voids coalesce, through-thickness channels can be formed. These channels provide a transport means for gases. The requirement on the current RF Foil is a leak rate of $1{\cdot}10^{-8}$ mbar·l/s at an overpressure of 25 mbar helium. A method should be established in which it is possible to perform an accurate prediction of the leak rate in case of a superplastically formed foil.

1.5.2 Requirement on wake field suppression

The determination of the amount of wake field suppression is very complex and the only way to obtain an accurate solution is by numerical methods. It is, however, possible to give some guidelines with respect to the geometry of structural parts, the basic thought behind these guidelines is that the charged particles in the wall may not deviate too much from the accelerated particles. The path followed by the particles in the wall may not be much larger than the straight path followed by the beam particles. A general rule of thumb here is that the smaller the corrugation depth (i.e. twice the amplitude of the foil waves) the better the wake field suppression. Simulations showed that losses due to resonant modes become acceptable for a corrugation depth smaller than 20 mm [7].

1.5.3 Mechanical requirements

For the RF Shielding box in the LHCb Vertex Locator, a pressure difference can occur between the inside (detector side) and the outside (beam side). Taking into account a safety factor in this pressure difference, the requirement is that at least

a pressure difference of 6 mbar should not damage the shield, which means in this case that this pressure may not result in plastic behavior of the RF Shield. If the pressure difference were to exceed this value, a gravity valve system would release the extra pressure until this 6 mbar difference was reached. An extra safety factor could be taken into account, but a gravity valve is already a redundant system on an electric valve, which releases the pressure when the difference exceeds 1 mbar. It is recommended that this extra safety factor of 6 is applied, because if the shield is damaged it has a disastrous effect (in which case the LHC beam should be switched off).

With respect to the elastic deformation of the shield under a pressure difference, the requirement is that in static conditions the RF Foils may not come in touch with another part (the opposing shield or the sensors) at an overpressure of 1 mbar. It is necessary that a safety factor (of 2) has to be taken into account, since dynamic effects also can play a role. The first natural frequency of the shield may not be less than 50 Hz, because of several input sources with a frequency below this value, such as rotating pumps and earth vibrations. Keeping the first natural frequency above 50 Hz will eliminate most of the amplitude of the external vibrations. To summarize the mechanical constraints:

- no plastic deformation may occur at a pressure difference of 6 mbar;
- the maximum elastic deformation at an overpressure of 2 mbar is 1 mm;
- the first natural frequency of the RF Box is at least 50 Hz.

1.5.4 Radiation length

As mentioned in [29], the average thickness of the aluminum RF Foil is 250 μm, but it is preferable to have a significant thinner foil in an ideal setup, having a thickness of 100 μm. For detector parts, there is no absolute requirement stating that the radiation length of a part should be limited by a predefined value. A demand is that the percentual radiation length is as low as possible. Dividing a traversed length by the material radiation length gives a percentual radiation length. This quantity must be spread out over a spherical area with the interaction point in the center of the sphere. The radiation length can be calculated using a Monte Carlo technique, as is for instance used in the GEANT physics software, which is a toolkit for the simulation of the passage of particles through matter. This software is freely available from the CERN website (http://geant4.cern.ch). It should also be possible to analyze this value numerically with a finite element code. This is, however, not incorporated in any commercial FE program, so this should be coded manually.

1.6 Project outline

This section outlines the methods followed in this project in order to act as a guideline for designing RF Foils to be used in future detectors. This involves the description of superplasticity, and experiments on a superplastic material. The outcome of the experiments have to lead to the development of a constitutive model of the material, to be used in structural analyses concerning sheet metal forming. This model is then used to establish an optimization procedure of the current RF Foil.

1.6.1 Describing superplastic behavior

Superplastic materials behave in a different way compared to conventional plastic materials as it comes to deformation beyond the plastic limit. The physical deformation mechanism of conventional plasticity is based on the plasticity of the grains, whereas the mechanism of superplastic deformation is merely based on the sliding of the grains past each other. In phenomenological terms, this manifests itself as a very high strain rate sensitivity, and also a very low flow stress compared to conventional aluminum flow, in the order of a few MPa. The phenomenon of superplasticity is described in Chapter 2.

1.6.2 Obtaining material behavior

To obtain material constants, the following material experiments are necessary; these experiment are the subject of Chapter 3:

- uniaxial experiments in order to find the optimal temperature for superplastic behavior to occur;
- uniaxial tensile experiments in order to find the uniaxial stress-strain behavior at different strain rates. These experiments should show the amount of strain rate sensitivity of the material and the void volume fraction evolution behavior;
- biaxial experiments (free bulge) in order to study the plane stress behavior and to obtain leak information and study the influence of a hydrostatic pressure during the deformation process. These biaxial experiments have to be carried out at different deformation velocities;
- biaxial experiments with a die, in order to study the frictional behavior of the material.

For both biaxial experiments, a test setup has to be designed, for which a description is necessary to show how to load the specimen and how to observe the behavior during the test run.

In the uniaxial test, the specimens need to be designed such that the testing machine has a sufficient stroke to account for the very large plastic strains occurring within superplastic materials. All experiments must be performed at an elevated temperature, at least half the absolute melting temperature of the observed material. This forming temperature is about 500 °C for aluminum alloys and 900 °C for titanium alloys. These two materials are the most common to be used as a basis for superplastic materials.

The same holds for the biaxial tests with respect to the temperature, here a specimen geometry and a test setup have to be designed which are as simple as possible, but which provide all the desired data to describe the material behavior. The experiment can consist of a circular test specimen, clamped on the outer edge, and pressed into a die with a circular cutout by means of an overpressure. Because the behavior at very high plastic strains can be dependent on the hydrostatic stress (since a hydrostatic pressure inhibits cavity nucleation and growth), this phenomenon also has to be investigated.

One of the most important requirements of the RF Shield is that it should be gas tight in order to prevent gas molecules from entering the beam pipe as much as possible. The leak-tightness is dependent on the state of the deformed material, which can be a stress and/or strain state in combination with the local sheet thickness. A test setup has to be designed to measure the leak of helium, which is known as a gas with a high mobility inside materials. This experiment has to measure the leak-tightness locally, in order to obtain information about the dependency on the quantities stated above. Leak measurements are also part of Chapter 3.

1.6.3 Creating the material model

The experimental results have to be fitted into a material model. The uniaxial experiments can be used to construct the one-dimensional material behavior. Within this one-dimensional model, the strain rate dependency of the flow stress is an important factor. As in many materials, strain hardening can occur and should be accounted for. At high plastic strains, the formation, growth and coalescence of internal voids are the main cause of strain softening. It is known that superplastic materials behave in an isotropic manner, which is caused by the micromechanical deformation mechanism of these materials. Tensile experiments carried out in different directions with respect to the rolling direction should show this isotropic behavior.

The free bulge experiments are used to investigate several aspects of the material. Firstly, the plane stress flow behavior is investigated, in order to obtain information concerning the yield locus. Secondly, the influence of a hydrostatic pressure during the sheet forming process can be studied. The application of a backpressure is likely to postpone the formation of voids, which leads to higher plastic strains before failure. The most important constraint, concerning the leak-

tightness of the sheet, must be incorporated into the material parameters, in order to predict this property of the formed sheets.

Friction is not part of a material model, but it should be accounted for in a forming simulation. Friction is important for the forming behavior of a sheet into a die with respect to formability, resulting sheet thickness and gas leak-tightness. The design of the experimental die is such that the friction coefficient influences can be deduced from thickness measurements.

The material model as constructed from the uniaxial and biaxial experiments is presented in Chapter 4.

1.6.4 Verification of the material model

The established material model, either a predefined material model inside the FE code or a user-defined material model, should contain enough material parameters to describe the mechanical behavior of the sheet material to a sufficient level. On the other hand, the amount of parameters should be reduced as much as possible, in order to avoid unnecessary complexity. Chapter 5 describes the simulation results of the experiments, where attention is paid to all three types of experiments. Within these verification simulations, formability and gas leak prediction are important.

1.6.5 Geometry optimization

Optimization problems generally involve three main ingredients. Firstly, an optimization goal must be determined, which has to be minimized. In the case of the RF Foil, the radiation length is the property to be minimized. This can be translated into an average path that a particle travels through the material. Since the resulting thickness largely determines the average traversed path, it is necessary that this path can be calculated from the FE model of the deformed sheet.

Secondly, the RF Foil is subject to a set of constraints, of which the already mentioned leak-tightness is the most important one. Other constraints are a minimum amount of wake field suppression, and the mechanical constraints as described in Section 1.3 (geometric stiffness, plastic deformation and first resonance frequency). The value of the objective function to be optimized changes if design variables are changed. These variables are mostly related to the dimensioning of the RF Foil. This means that the 3D model of the foil should be parameterized. Another design variable besides the dimensioning can be the initial sheet thickness. Starting with the thinnest sheet will be beneficial with respect to the radiation length, but a thicker sheet may be more able to conform to the constraints of leak-tightness and the mechanical restrictions. The optimization procedure is described in Chapter 6.

2. Superplasticity

Superplasticity can be defined as the ability of polycrystalline materials to exhibit very high elongations prior to failure. This high elongation (ranging from a few hundred to several thousand percent) can only be obtained in a narrow range of operating temperature and strain rate. Within this range, superplastically deformed materials show a very high resistance against necking; the material gets thinner in a very uniform manner. Stresses to establish superplastic flow are low compared to conventional plastic flow. The main requirement for a material to behave superplastically is a fine grain size, which can vary from material to material between 1 and 10 μm. The grains should be randomly oriented in the material, causing it to behave isotropically, and may not grow during plastic deformation, in order to maintain the superplastic properties throughout the entire forming process.

Summarizing, it can be stated that for a material to behave mechanically in a superplastic way, this means in general that very high plastic strains can be reached in the material before failure, but only if the following rules apply:

- the microstructure of the material should show small grains, typically in the order of a few microns. However, there is also a growing tendency to do research on superplasticity in more coarse-grained alloys [76];

- deformation should be carried out at an elevated temperature, which is generally higher than temperatures needed for conventional warm forming. Superplastic aluminum alloys, for instance, show their superplastic behavior at a temperature of about 500 to 550 °C [4], superplastic titanium alloys need a temperature of about 800 to 950 °C [46, 70];

- the strain rate in the material should be low, depending on the alloy. Typical optimal strain rates for superplastic behavior range in the order of 10^{-4} to 10^{-2} s^{-1}. There are also a few known alloys which show superplasticity at higher strain rates [19].

There are two reasons for choosing the superplastic forming process in the context of this project when compared to other processes. One is that superplastic materials can achieve high strains without necking, the other is that the forces required

for superplastic deformation are relatively low, thereby making it a cost-effective process, especially if a small number of products need to be produced.

Superplasticity does not show the same deformation mechanism as conventional plasticity. Briefly, in the latter case, the grains will deform and this will introduce a texture in the material. Superplasticity is caused by the sliding of grains past each other, whereby the grains themselves do not deform substantially. Because of this different deformation mechanism, the mechanical properties of superplastic materials differ from conventional plasticity in terms of very low flow stresses and a very high strain rate dependency of these flow stresses. The physical mechanism of superplasticity is elaborately described in Section 2.1 of this chapter.

Superplasticity is not applicable to every material. The alloys which are suited best to superplastic forming applications are based on aluminum or titanium. Section 2.2 focuses on some materials which are mostly used in industry nowadays, this section also describes the chosen material in this research, ALNOVI-1.

Hardening in superplastic materials is caused by grain growth, which is also different from the conventional plasticity rules, where the Hall-Petch effect states that grain growth induces softening [55]. Softening in superplastic materials is caused by the formation and growth of internal voids. Section 2.3 focuses on the mechanical behavior of superplastic materials. Two methods to describe this behavior are discussed, a macromechanical (phenomenological) and a micromechanical (physical) approach. The first one can be derived from mechanical experiments such as uniaxial and bulge tests, the second describes the material behavior in terms of the atomic and crystalline substructure (e.g. vacancy diffusion and activation energies).

The description of multiaxial behavior is a very important issue in sheet forming simulations, so Section 2.4 is dedicated to multiaxial mechanical behavior of materials in plasticity. A choice of flow criteria is presented, focused on plane stress plasticity.

From experiments, as described for instance in [78], it is known that the mechanical behavior of superplastic materials can be influenced by the application of a backpressure during the forming process. High backpressures can lead to an increase in the maximum elongation prior to failure, which is due to the fact that void formation and growth is postponed. The hydrostatic pressure-dependency of superplastic materials is described in Section 2.5.

This chapter ends with a brief overview of calculations involving computational (super-)plasticity. The stress update procedure described here is dependent on the applied flow criterion.

2.1 Physical mechanism of superplasticity

The exact micromechanical mechanism of superplasticity is still not understood completely. It is very different from the conventional behavior of materials which

show elastoplasticity, viscoplasticity or creep. These material behavior mechanisms intend to stretch the grains in the direction of the highest principal stress, whereas a superplastically deformed material has about the same microstructure as the undeformed material.

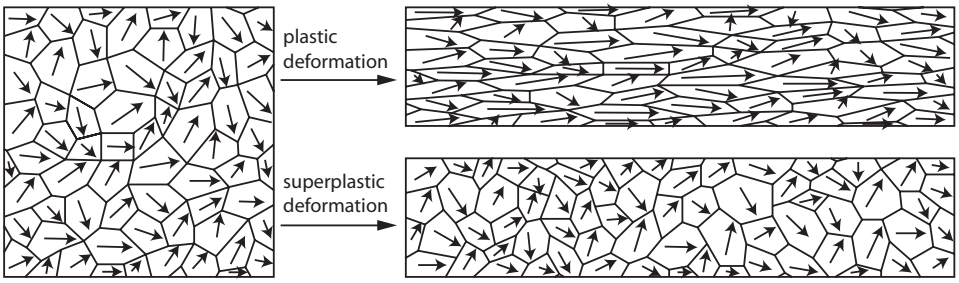

Figure 2.1: The difference between plastic and superplastic deformation on a micrograin scale; arrows indicate the crystal orientation.

This is shown in Figure 2.1, where it can be seen that in the case of superplastic deformation, the grains do not change in aspect ratio [15]. This behavior has two consequences: the material is less subject to become anisotropic during plastic deformation, the other consequence is that superplastic materials in general show less hardening than materials showing conventional plasticity.

At the moment it is believed (and also proved up to some extent) that superplastic flow is dominated by a process which is called *Grain Boundary Sliding (GBS)* [56] . Grains tend to slide past each other, instead of deforming, and this sliding is made more convenient by the material by means of some accommodation mechanisms. These mechanisms are not completely understood yet, but the grain boundaries are known to play some important roles in superplasticity.

2.1.1 Grain boundary sliding

Grain boundary sliding is a process in which the grains slide past each other along their common boundary. At the optimal temperature for superplasticity, the boundary is weaker than the grains themselves, so sliding along this boundary seems a more efficient way for the material to deform plastically under the conditions of a high temperature and a low strain rate. Micromechanically, this is a very heterogeneous process. It has been observed that superplastic flow occurs because of the simultaneous sliding of groups of grains along each other, which is denoted as *cooperative grain boundary sliding* (CGBS) [37, 81]. If during deformation grain growth is observed, then the formation of slide surfaces, along which CGBS can

act, is restrained, and the superplastic flow will stop. This means that grain growth has to be prevented as much as possible in order to achieve superplastic behavior.

2.1.2 Accommodation mechanisms

If GBS were the only mechanism to occur in superplastic flow, then either the grains would have an ideal shape, such as a square, or huge cavities would occur in the material just before sliding takes place. Neither is the case. This means that in between the two grain boundary sliding steps another mechanism is responsible for this happening; it is called an *accommodation mechanism*. Two mechanisms will be discussed here, Diffusion Creep and Intragranular Slip. The mechanisms described are still under discussion, and it is also believed that grain boundary diffusion can be accommodated by partial melting in the boundary zone because of the elevated temperature. The effect of all accommodation mechanisms stays the same: taking care of a coherent shape between the sliding grain boundaries, without introducing large cavities. The accommodation mechanism builds up until a certain threshold stress. If this stress is reached, then (cooperative) grain boundary sliding will take place in a fraction of the time of the build-up period.

Diffusion Creep Diffusion Creep [44] is a creep process, acting at very low stresses. Along the grain boundaries where a tensile stress acts, there is an excess of vacancies. These vacancies can flow to areas where there is a shortage of vacancies, especially in areas where a tensile stress acts. These vacancies can travel through the grain (Nabarro-Hering diffusion creep) or along the grain boundary (Coble diffusion creep) [23, 57]. In superplastic flow, this can lead to a mechanism called *grain switching*, proposed by Ashby and Verrall [2], see Figure 2.2.

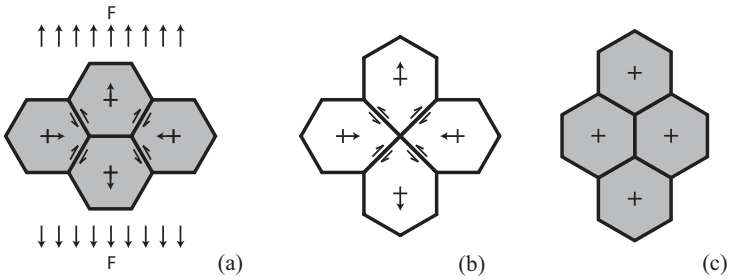

Figure 2.2: The grain switching mechanism of Ashby and Verrall. (a) initial state, (b) intermediate step, (c) strain of 0.55 without grain deformation.

Intragranular Slip If a slip plane arises inside a grain, then this is called *intragranular slip*. An extra boundary can grow inside this grain due to a collective movement of dislocations, which can assist in the mechanism of cooperative grain boundary sliding. Such a dislocation line inside a grain will then be collinear with the favorable sliding path. Intragranular slip is not seen in every superplastic material, this is especially seen in materials based on Al-Mg.

2.1.3 Grain growth

Since at a high enough temperature the grain boundaries in a superplastic material are weaker than the material in the grains itself, the superplastic properties of a material are very dependent on the grain size. There is a strong relationship between the grain size and the *strain rate sensitivity parameter m* [3]. This parameter determines the superplastic flow behavior, as shall be shown in Section 2.3. Because every grain boundary is an imperfection, the free energy of the material is higher at these places. Therefore there is a tendency to grain growth to reduce this free energy. This process is temperature dependent and can be expressed as:

$$d^g - d_0^g = Bt \, \exp(-Q/RT) \tag{2.1}$$

in which d and d_0 are the current and initial grain size, B is a constant, Q is the activation energy, R is the universal gas constant, T is the temperature and t is the time. For normal grain growth, (also called *static grain growth*) where the strain rate is zero, g is equal to 2. This is a diffusion controlled process, hence dependent on the temperature. Grain growth must be prevented as much as possible, because the fracture strain decreases as the grain size increases. This reduction of free energy can also be achieved by adding mechanical energy instead of thermal energy, which means that deforming the material also leads to grain growth, which is called *dynamic grain growth*.

Superplastic alloys have generally very good resistance to both types of grain growth, which is a result of the constituents (alloying elements). Both types of grain growth work independently from each other, which is, for instance, clearly visible from the grain size evolution law, as described in [50]:

$$\dot{d} = M\sigma_{\text{surf}} d^{-r_0} + \alpha \dot{\varepsilon}^{\text{p}} d^{-r_1} \tag{2.2}$$

in which r_0, r_1 and α are constants, M is the grain boundary mobility which is temperature dependent and σ_{surf} is the grain boundary energy density.

Static and dynamic grain growth can conflict with each other and it is desirable that grain growth in general must be avoided as much as possible. Dynamic grain growth is low if the strain rate is low, but this means that the exposure time to an elevated temperature will be higher, and hence will lead to higher static grain growth. Higher strain rates will lead to a higher dynamic grain growth, but to lower static grain growth. Generally, a superplastic material has an optimum strain rate at which the superplastic properties are optimal.

2.1.4 Cavity formation

If the grains were able to just slide past each other as infinitely rigid particles, then very quickly internal voids would occur, also called *cavities*. In the first stage of superplastic behavior, cavities do not arise, and they are normally seen during the last stage of superplastic flow. The cavitation process consists of three stages, which can occur simultaneously.

- cavity nucleation: this takes place at irregularities, where for instance the accommodation mechanism cannot completely compensate for the non-coherence of the shape of adjacent grains. Most irregularities are at places where the grain boundary switches orientation (at triple junctions), or at places where second-phase particles are present.

- cavity growth: with increasing strain, cavities can become larger. They act as large vacancies to where minor vacancies in the structure can diffuse, called *stress directed vacancy diffusion*. Cavity growth is the cause of unstable plastic flow. An equation to describe the cavity volume fraction as a result from cavity growth is found in [5]

$$\xi = \frac{3}{2}\Big(\frac{m+1}{m}\Big)\sinh\Big[2\Big(\frac{2-m}{2+m}\Big)\Big(\frac{k_\mathrm{s}}{3}-\frac{p}{\sigma_\mathrm{e}}\Big)\Big] \tag{2.3}$$

  where m is the strain rate sensitivity, k_s is a stress concentration factor depending on the amount of grain boundary sliding, p is the pressure and σ_e is the equivalent stress.

- cavity coalescence: the internal voids start to interlink with each other to create a crack in the material. According to [45], the coalescence condition can be written as

$$\frac{\sigma_\mathrm{m}}{\sigma_\mathrm{f}}\frac{1}{(1-\chi^2)} = \frac{2}{3}\left[\alpha\left(\frac{1-\chi}{\chi W}\right)^2 + 1.24\sqrt{\frac{1}{\chi}}\right] \tag{2.4}$$

  where σ_m is the matrix stress (the stress in the material around the cavities), σ_f is the macroscopic flow stress, χ is the relative void spacing (void mean diameter over mean void distance), W is the void aspect ratio, and α is a parameter which is 0.1 if there is no hardening present (which can be assumed at the point of void coalescence).

As said earlier, cavity forming only arises during the last stage of superplastic forming, and is an indication of fracture initiation, and therefore can lead to unrecoverable damage to the material. In an earlier stage the material starts leaking, which is more relevant in this research project. It is interesting to see that, in contrast to plasticity, cavities in superplastically formed materials are much more

rounded [64]. It must also be noted that from earlier research [85] it follows that a hydrostatic pressure inhibits the formation and growth of cavities and thereby increases the maximum attainable plastic strain before mechanical failure of the material occurs.

2.1.5 Production of superplastic materials

Adding energy, by deforming a material plastically, can result in a reduction of the grain size. A method to achieve superplastic bulk material is by torsion under pressure. A better known process is the so-called *Equal Channel Angular extrusion (ECA)* [62], see Figure 2.3. In the case of ECA, a billet of material is pushed through a channel with a sharp bend in it, which results in simple shear. The two channels of the tool have the same cross section, so the cross-sectional area during this deformation process does not change. This process is repeated several times to obtain an ultra-fine grain size. This process is also used for materials to be used at room temperature, since according to the Hall-Petch relationship, the strength increases at decreasing grain size.

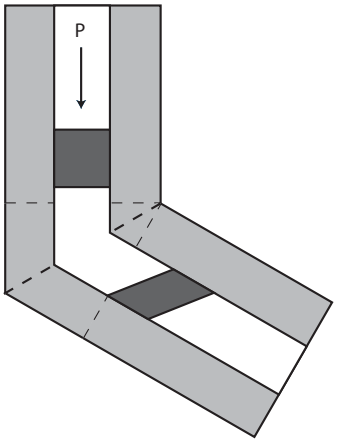

Figure 2.3: Schematic view of Equal Channel Angular Extrusion.

A process to produce sheets of superplastic material is by *Accumulative Roll Bonding* (ARB) [41]. A sheet of material is rolled until half the thickness and twice the length, and then cut in two to obtain two sheets with the original dimensions but with half the thickness. Then these two new sheets are stacked and the roll-bonding process of thinning and lengthening starts again. The number of bonded layers grows exponentially with the amount of rolling cycles.

2.2 Superplastic materials in industry

This section elaborates on the most common materials which can be used in superplastic deformation processes. These materials are mostly aluminum or titanium-based alloys, but some stainless steel or more exotic materials can show superplastic behavior too. Superplastic materials contain generally dedicated alloying elements (second-phase particles), commonly functioning as a grain growth inhibitor. This chapter focuses exclusively on the superplastic behavior of metals, this means that polymers and ceramic materials are excluded from the summarized materials list. Other metal alloys include, for instance, the 2205 series stainless steel, the copper-based alloy Coronze CDA-638 and the nickel-based alloy Inconel 718. Compared to aluminum and titanium, these materials have a much higher density. This is why these materials are not used very often in structural applications, unless some typical properties are desired.

2.2.1 Aluminum-based materials

Most materials which are used in superplastic forming processes, are aluminum-based materials. These materials belong to the category of *pseudo-single phase* materials, with relatively small amounts of second-phase elements. They have a high resistance to static grain growth. Their superplastic behavior is the reason why these materials are categorized under names as *Supral* and *Formall*. Typical superplastic forming temperatures are about 500 to 550 °C. The density of aluminum is about 2700 kg/m^3.

Supral 100 and 150 These are the commercial names for Aluminum Alloy 2004SPF which is a medium-strength alloy with mechanical properties similar to AA6061 and AA2219 and is used in lightly loaded or nonstructural applications, e.g. in the aerospace industry. It is manufactured by Superform USA, Inc. AA2004-SPF is alloyed with 6% Cu and small amounts of Mg and Zr. It can reach a nominal plastic strain before fracture of more than 200% [66].

Formall 545 and 700 Formall is the commercial name for superplastic aluminum alloys manufactured by Alusuisse Swiss aluminum and comes in two alloy types, AA5083-SPF and AA7475-SPF, respectively. In AA5083, the main alloying element besides aluminum present in this alloy is magnesium; in AA7475 zinc and copper are the main alloying elements [17]. For these materials, some superplastic material data was found in the literature. AA5083-SPF has a strain rate sensitivity parameter of 0.60 at a flow stress of 3 MPa, whereas AA7475-SPF has a strain rate sensitivity parameter of 0.70 at a flow stress of 3 MPa at the superplastic temperature. Applications are, for instance, car body panels in the automotive industry. The maximum nominal plastic strain before fracture is about 400 % [83].

2.2.2 Titanium-based materials

Titanium has a much higher melting point in comparison with aluminum, the superplastic processing temperature of titanium-based alloys is about 900 °C. Below this temperature, pure titanium consists of a hexagonal close-packed structure, called the α-phase. Above this temperature, the structure is body-centered cubic, which is called the β-phase. The α-phase is particularly useful in cryogenic applications, where the material has its best strength properties, whereas at room temperature the strength is low. The β-phase has a much higher strength at room temperature, but this phase can only be contained at room temperature if the material is solution-treated with e.g. vanadium. Superplastic behavior of titanium alloys can only be observed in a mix of the two phases, so stabilizers should be added to ensure that these two phases keep existing in the alloy. Aluminum, which can be added up to 8%, is an α-stabilizer, whereas molybdenum and vanadium are the best known β-stabilizers. The density of titanium is about 4300 kg/m^3.

Ti-6Al-4V alloy This is the most used superplastic titanium alloy, especially for the manufacturing of structural aircraft parts. It has a superior strength-to-weight ratio and corrosion resistance at high temperatures. Its optimum forming temperature with respect to superplasticity is 800 °C, but the range of temperatures in which superplastic behavior is active is quite broad (between 700 and 950 °C) [70]. At room temperature, the maximum elongation is about 20%, but this value increases quickly starting at a temperature of about 500 °C to a value of about 300% at the optimal superplastic temperature [36]. Above 800 °C, the material suffers from dynamic grain growth, which then will be more dominant with respect to dynamic recrystallization.

Ti 14-25% Al 10-20% Nb 3% V 2% Mo This special alloy is also called Super Alpha 2 and is actually an alloy of titanium aluminide. The aluminide shows very brittle behavior, the addition of niobium makes the material ductile. This alloy has an excellent oxidation resistance at high temperatures, which makes it a suitable material for use in jet engines and supersonic aircraft. At room temperature, this material shows very brittle behavior. This material is, in contrast to the pseudo-single phase materials, a mixture of grains of the matrix phase and grains of the alloying phase, a so-called *microduplex* superplastic alloy. The optimal superplastic temperature is about 960 °C [65], showing an elongation of more than 1000 %.

2.2.3 ALNOVI-1

ALNOVI-1 is a relatively new material also based on AA5083, manufactured by Furukawa Sky aluminum, Japan [25, 78]. It is designated a superplastic material, although it does not reach the extremely high plastic strains which can be reached by other superplastic materials. A grain growth inhibitor is added (0.8% Mn). At

room temperature, this material has a high strength (yield strength of 160 MPa and tensile strength of 297 MPa). The optimal superplastic temperature is about 520 °C. At this temperature, a stretch of 300 to 500% can be reached according to the manufacturer. This material will be chosen for use in this research project. There are a few reasons to use this material, instead of the other materials presented earlier.

The main reason is that the minimum sheet thickness that can be obtained from manufacturers of superplastic materials is typically 1.0 mm, not only for aluminum alloys, but also for titanium superplastic materials. ALNOVI-1 can be obtained in sheets with a minimum thickness of 0.3 mm. This is beneficial in the context of this research project, since its goal is to minimize the resulting wall thickness. This material has been ordered from the manufacturer as a sample batch with thicknesses of 0.3, 0.5, 0.8 and 1.0 mm.

The second reason to use ALNOVI-1 is the ability to weld this material. The RF Box has been built up of five separate panels welded into a box. Not only the top foil of the box itself, but also the welding seams showed some gas leak. A test showed that ALNOVI-1 can be perfectly welded, even better than the AA5083 alloy that was used for the current RF Box.

Thirdly, this material can be ordered in small batches. In case of RF Boxes, only two pieces are necessary which makes the usage of other aluminum superplastic materials an expensive option. Besides, titanium superplastic materials are also very expensive, even in small batches.

In this research, titanium superplastic alloys will not be considered at all since aluminum is a much lighter material which is beneficial in terms of radiation length. Because the optimal superplastic temperature of superplastic titanium alloys is much higher than that of superplastic aluminum alloys, the manufacturing of dies would be a much more complicated and expensive option. Dies for superplastic aluminum alloys can be made from stainless steel AISI321, for which its strength is conserved at the optimal superplastic temperature for aluminum.

2.3 Mechanical behavior of superplastic materials

Superplastic materials show a very high sensitivity in mechanical properties with respect to the strain rate, especially the flow stress. Another important factor is the temperature. At the optimal superplastic temperature, the stress-strain behavior looks like the graphs plotted in Figure 2.4 [69], from which the conclusion can be drawn that the flow stress is very low at this optimal temperature. This section presents two general methods to describe mechanical behavior of superplastic materials: firstly a phenomenological way, secondly a physical method.

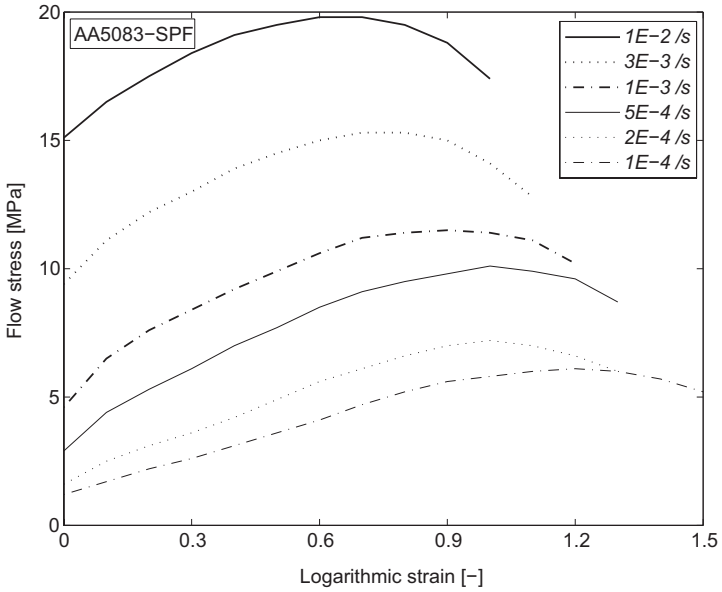

Figure 2.4: Example of the stress-strain behavior of AA5083-SPF at 530 ^{o}C [69].

2.3.1 Phenomenological material behavior

Since the strain rate is the dominating factor, a very simple expression for the flow stress is used in some calculations involving superplastic material behavior. This equation involves the influence of the strain rate by an exponent m only, see for instance [4, 62, 69, 71], which is the strain rate sensitivity. This results in the flow formulation:

$$\sigma = k(T)\,\dot{\varepsilon}^{m} \tag{2.5}$$

where $k(T)$ is a constant dependent on the temperature T. In this section, the formulation for the initial flow stress is further elaborated, and extended with a strain hardening and softening behavior. Far more complex flow formulations are known from literature, for instance in [10], where a formulation has been derived for the superplastic titanium alloy Ti6Al4V.

When the stress is plotted against the strain rate in a log-log diagram, this results in a straight line with slope m. However, in reality, it appears from experiments that this line is not straight, but shows a sigmoidal curve, as can be seen in Figure 2.5(a). The curve can be divided into three areas as shown in the figure. The point where the highest slope can be found, is equal to $m_{\max}$, this point is called the *inflection point* of the curve, and is situated in the relatively narrow area II. This means that m is dependent on the strain rate (see Figure 2.5(b)). In fact

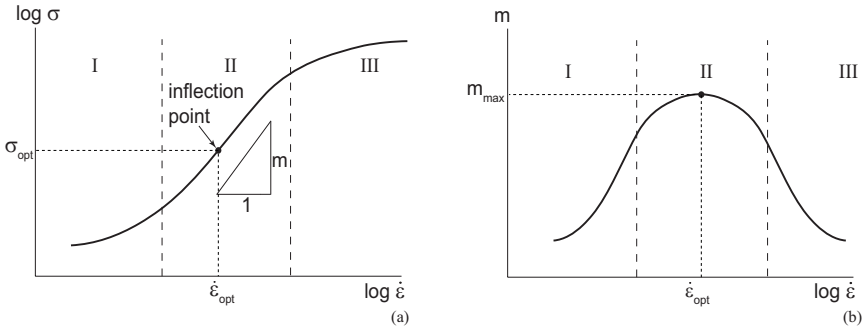

Figure 2.5: Typical superplastic material behavior. (a) Sigmoidal curve showing stress-strain behavior, (b) Strain rate sensitivity parameter m as function of the strain rate.

m can only be considered constant over a narrow range of strain rates, so Equation (2.5) is only valid within this very small range. Besides that, m is also strongly temperature dependent.

It can be shown that the higher m is, the higher the resistance against local necking of the material. The biggest advantage of the power law (2.5) is that it is a simple formulation, however, the disadvantage is that the applicability range is very small. It can be useful in experiments, where everywhere in the test specimen the strain rate and the temperature are constant, but in practical applications a range of strain rates is present. Besides, this power law also represents the superplastic behavior of materials: if somewhere in the material onset of necking is present, then in that area the strain rate is higher and therefore results in a large increase in flow stress compared to more conventional plastic behavior. The neck undergoes strain rate hardening which prevents further necking. A high strain rate sensitivity thus means a high resistance to necking.

A more elaborated approach is one in which the shape of the curve in Figure 2.5(a) is accounted for. A way to describe this curve is by means of the so-called *Universal Superplastic Curve*, in which an expression for the slope m is written as:

$$\frac{m}{m_{\max}} = \exp\left(-a^2(\log\frac{\dot{\varepsilon}}{\dot{\varepsilon}_{\text{opt}}})^2\right) \tag{2.6}$$

in which, for many superplastic materials, $a \approx 0.25$ [82]. However, this formulation is far from complete to describe the mechanical behavior of superplastic materials, because it does not account for strain hardening. It also does not account for a flow stress at a strain rate approaching zero, the initial flow. Since this equation describes the slope of the curve, the initial flow stress should then be described by an integration constant. Another way to describe the initial flow stress is to adjust the general equation for a sigmoidal curve $f(t) = 1/(1+\exp(-t))$ with four

parameters. In general terms, these four parameters scale and shift the normalized curve in two directions. This can result in an expression like

$$\log(\sigma_{y0}) = \frac{1}{a + b\exp(c\log\dot{\varepsilon})} + d \tag{2.7}$$

in which a, b, c and d are the customizing parameters. These parameters can be determined by tensile tests at different cross-head velocities.

Strain hardening Most materials show an increasing flow stress with an increasing plastic strain. This is also the case with superplastic materials, but the hardening mechanism is thought to be different from the strain hardening mechanism of conventional materials. Conventional materials follow the Hall-Petch effect, which proposes a relationship between grain size and flow stress, thereby showing lower flow stresses at higher grain sizes. Since in superplasticity it is believed that strain hardening is caused by grain growth, it seems straightforward that a relationship is constructed between these two quantities. At elevated temperatures, high enough for superplastic material behavior, the grain boundaries are much weaker than the grains themselves, so the Hall-Petch effect is not applicable in that case.

When the curves from Figure 2.4 are observed, it may also be possible to describe the hardening rule with a Voce model, which makes use of a saturation stress (a maximum hardening stress which is reached asymptotically), see e.g. [12]. The Voce model is generally applicable to aluminum alloys which are deformed at elevated temperatures. Despite the fact that superplastic deformation is physically different from conventional plastic deformation, the Voce approximation seems an acceptable option to use in calculations involving superplasticity.

Strain softening Several studies describe the behavior of cavities in (superplastic) materials. The best known is Gurson's porous metal plasticity model. His analysis is based on a spherical void in a unit cell, in which the void growth can be determined as a function of the rate-of-deformation tensor $\mathbf{D}$. This model takes into account that the voids already exist in the initial configuration and no void nucleation is accounted for. Needleman [60] developed a model for the nucleation of voids, which can be considered stress- or strain-driven. The advantage of Gurson's description is that a hydrostatic stress can be accounted for in the model [63]:

$$\dot{\xi} = (1-\xi)\,\mathrm{tr}(\mathbf{D}) + \mathcal{A}\,\dot{\sigma}_{\mathrm{m}} + \mathcal{B}\,\dot{\Sigma}_{\mathrm{h}} \tag{2.8}$$

in which ξ is the void volume fraction, σ_{m} is the yield stress of the matrix material and Σ_{h} is the average hydrostatic stress in the material. Furthermore,

$$\mathcal{A} = \mathcal{B} = \frac{f_{\mathrm{N}}}{s\sqrt{2\pi}}\,\exp\Big[-\frac{1}{2}\Big(\frac{\sigma_{\mathrm{y}} + \Sigma_{\mathrm{h}} - \sigma_{\mathrm{N}}}{s}\Big)^2\Big] \tag{2.9}$$

This equation represents a normal distribution, with σ_N being the mean stress for void nucleation with a standard deviation of s. f_N is the volume fraction of the particles responsible for void nucleation. An expression for the macroscopic flow stress is given by [39]

$$\sigma_f = \sigma_y(1 - n_1\xi^{n_2})^{n_3} \tag{2.10}$$

where n_1, n_2 and n_3 are adjusting parameters.

Much more complex descriptions of void growth and the effect on the flow stress are available in the literature, most of them are based on micromechanical analyses. The downside of the use of phenomenological models is that the constants, which describe the material behavior, do not have a direct physical meaning.

2.3.2 Physical material behavior

The foregoing approach is a purely phenomenological one, but it is also possible to create a more physical model in order to describe the mechanical behavior of superplastic materials. Physical models of superplastic flow directly incorporate the micromechanical parameters into the constitutive equations. A classical model is a description given by Valiev and Kaibyshev [62]:

$$\dot{\varepsilon} = \frac{\dot{\sigma}}{E^*} + \frac{\Omega D}{16kTG} \cdot \left(\frac{\sigma - \sigma_0}{d}\right)^2, \qquad \sigma > \sigma_0 \tag{2.11}$$

where σ_0 is the threshold stress, Ω the volume of a vacancy (the atomic volume), k the Boltzmann constant, G the shear modulus, D the coefficient of grain boundary diffusion, E^* an effective modulus which has to represent the system 'specimen-testing machine' and d the average grain size. The effective modulus E^* is a weighted average modulus of the cross-head and the specimen in uniaxial experiments. Since the flow stress in a superplastic material (specimen) is very low compared with conventional materials (cross-head), the elastic deformation is very small. The second term in Equation (2.11) therefore becomes the dominant factor in an already early stage of the uniaxial test.

Besides this model, a lot of modern theories have been established to describe superplastic flow in terms of physical constitutive equations, but the main drawback of these models is the fact that no standard test has been described to determine the necessary parameters [42, 43, 53, 61]. Also the range of applicability cannot be predicted and the models do not allow for transient regimes of loading.

2.4 Multiaxiality

Experiments on tensile test specimens result in a uniaxial stress-strain behavior, generally presented as a set of stress-strain curves at different strain rates. In the case of sheet metal deformations (i.e. plane stress situation), two in-plane normal

stresses and one in-plane shear stress are present; or, in principal directions, only two normal stresses are present.

Material flow is dependent on both these stresses. Different formulations have been developed to determine whether a material will flow in a certain stress situation. Here, three of these formulations are discussed: the von Mises, the Tresca and the Hosford flow criterion. The first two criteria can be seen as a special case of the Hosford flow criterion, which in its turn is a special, isotropic, case of the more general Yld2000 criterion.

2.4.1 Flow conditions

If in a material point a stress situation falls inside the yield locus (point A in Figure 2.6), then the material behaves elastically and there is no plastic flow present.

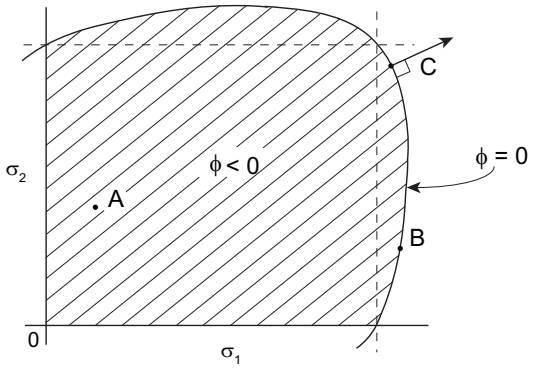

Figure 2.6: Yield locus, showing three points: point A is in a purely elastic situation, point B is in a mixed elastic-plastic situation, further plastic strain starting from point C flows in a direction perpendicular to the yield locus.

Besides, a stress situation can never lie outside the yield surface. This means that if the material flows, the stress situation is always positioned on the yield locus, see point B in Figure 2.6. The position of the yield locus, however, can be dependent on the amount of deformation (strain hardening) or on the deformation rate (strain rate hardening). Superplastic materials generally show a low strain hardening with respect to conventional plasticity, but a very high strain *rate* hardening.

According to Drucker's postulate, the direction of the plastic strain rate is always perpendicular to the yield surface and is called *associative* plastic flow; see

point C in Figure 2.6

$$\mathbf{D}^{\mathrm{p}} = \dot{\lambda}\frac{\partial \phi}{\partial \boldsymbol{\sigma}} \tag{2.12}$$

in which $\dot{\lambda}$ is the plastic multiplier. Two assumptions are generally made in plastic flow theory which may not be directly applicable to superplastic flow:

- the position of the yield surface is independent of the hydrostatic pressure. It is known that failure of superplastic materials is caused by cavity formation in the material and it is believed that the application of a backpressure can inhibit this effect.
- the volume of the material during plastic flow is constant. In superplasticity, the macroscopic volume increases due to cavity formation.

This means that strictly speaking the flow behavior is non-associative. Generally, the hydrostatic pressure, which is caused by application of a backpressure during the deformation process, does not change. This makes the use of a non-associative flow model unnecessary if the hydrostatic pressure only influences the void volume fraction and does not change the relationship between the void volume fraction and the softening stress.

2.4.2 Yield criteria

A yield criterion is always formulated in such a way that a value, represented as ϕ, is smaller than zero if the stress situation falls inside the yield surface and zero in case it falls on the yield surface. The Kuhn-Tucker relations have to be satisfied:

$$\begin{aligned} \dot{\lambda} &\geq 0 \\ \phi &\leq 0 \\ \dot{\lambda}\phi &= 0 \end{aligned} \tag{2.13}$$

In metal plasticity calculations, the von Mises yield criterion is mostly used for isotropic material behavior. Because superplastic materials are known to behave in an isotropic way, three yield criteria will be discussed here which can be used for this purpose: von Mises as the most common criterion, the Tresca criterion as a limit situation, and the Hosford criterion as a generalization of both these criteria. These three criteria can all be considered as derived from the more general Yld2000 flow criterion [9, 86], an orthotropic yield function applicable to sheet material (plane stress).

Von Mises yield criterion If projected onto the π *plane*, which is the cross section of the yield surface perpendicular to the line $\sigma_1 = \sigma_2 = \sigma_3$, the yield locus is a circle. The von Mises yield criterion is based on the assumption that a material

flows if a certain deformation energy is exceeded. The flow equation in principal stress space for the von Mises yield criterion reads:

$$\phi = \sqrt{(\sigma_1 - \sigma_2)^2 + (\sigma_1 - \sigma_3)^2 + (\sigma_2 - \sigma_3)^2} - 2\sigma_\mathrm{f} \leq 0 \tag{2.14}$$

or

$$\phi = \sqrt{\frac{3}{2} s_{ij} s_{ij}} - \sigma_\mathrm{f} \leq 0 \tag{2.15}$$

in which s_{ij} are the deviatoric stress components from the tensor $\mathbf{s}$ according to

$$\mathbf{s} = \boldsymbol{\sigma} - \frac{1}{3}\mathrm{Tr}(\boldsymbol{\sigma}) : \mathbf{I} \tag{2.16}$$

and σ_f is the uniaxial yield stress. With reference to an arbitrary orthonormal coordinate system with axis directions x, y and z, the von Mises yield criterion can be written in a general form:

$$\phi = (\sigma_x - \sigma_y)^2 + (\sigma_y - \sigma_z)^2 + (\sigma_z - \sigma_x)^2 + 6\tau_{xy}^2 + 6\tau_{yz}^2 + 6\tau_{zx}^2 - 2\sigma_\mathrm{f}^2 \leq 0 \tag{2.17}$$

Tresca yield criterion This criterion is based on the assumption that a material flows if a certain shear stress is exceeded. The Tresca yield criterion is defined as

$$\phi = \max(|\sigma_1 - \sigma_2|, |\sigma_1 - \sigma_3|, |\sigma_3 - \sigma_2|) - \sigma_\mathrm{f} \leq 0 \tag{2.18}$$

σ_f is the yield stress in a uniaxial stress state. The Tresca yield stress criterion can be interpreted as a maximum shear stress criterion, where the maximum shear stress is defined as:

$$\tau_\mathrm{max} = \frac{1}{2}\max(|\sigma_1 - \sigma_2|, |\sigma_1 - \sigma_3|, |\sigma_3 - \sigma_2|) = \frac{1}{2}\sigma_\mathrm{f} \tag{2.19}$$

In plane stress situations, $\sigma_3 = 0$.

Hosford yield criterion From experiments it follows that the von Mises yield criterion is not sufficient in case of f.c.c. materials, such as aluminum [54, 59]. These materials show a flow behavior which is situated between the von Mises and Tresca yield criteria. Both these yield criteria can be expressed in the same way in the format of a general equation

$$\phi = (|\sigma_1 - \sigma_2|^n + |\sigma_1 - \sigma_3|^n + |\sigma_2 - \sigma_3|^n)^{1/n} - 2\sigma_\mathrm{f} \leq 0 \tag{2.20}$$

named after its developer, Hosford [32, 33]. In the case that n equals 2, the von Mises criterion is the result; the Tresca yield criterion is obtained if n goes to infinity. In the case of aluminum plasticity (or f.c.c. metal plasticity in general), the best fit is commonly reached at $n = 8$. The higher n, the sharper the corners of

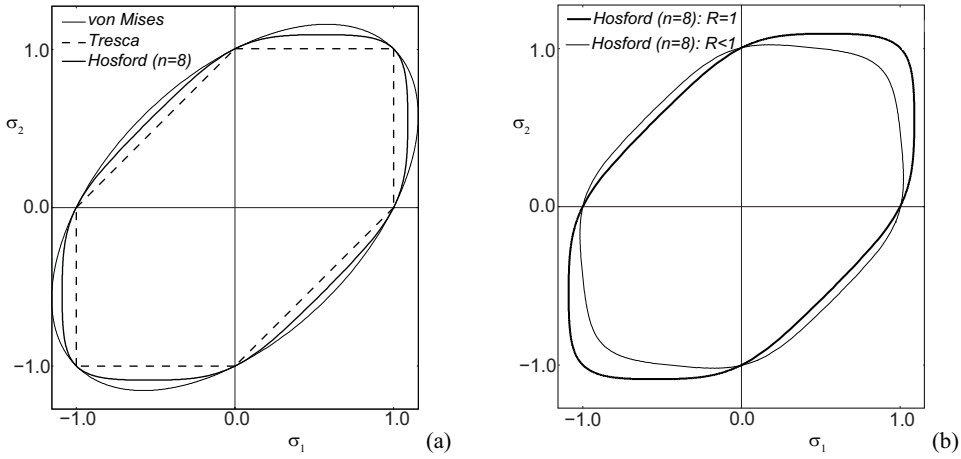

Figure 2.7: The Tresca, von Mises and Hosford yield criteria in two-dimensional principal stress space.

the yield locus. The three yield criteria mentioned here are shown in Figure 2.7(a). The Hosford criterion as mentioned in Equation (2.20), is used in the case of three-dimensional isotropy. In cases of sheet metal applications, materials can show an out-of-plane anisotropy, expressed in the Lankford strain ratio R. In [59], the Lankford strain ratio was measured as a function of the temperature for a 5083 aluminum alloy. Here it was shown that this ratio increases with temperature. The Lankford strain ratio is the ratio between the uniaxial in-plane strain (in y direction) and the out-of-plane strain (z direction) in case of an applied stress in x direction

$$R = \frac{\varepsilon_z}{\varepsilon_y} \tag{2.21}$$

The expanded version of the Hosford yield criterion is given, where this Lankford strain ratio is incorporated, which is

$$\phi = \frac{1}{1+R}(\sigma_1^n + \sigma_2^n) + \frac{R}{1+R}(\sigma_1 - \sigma_2)^n - \sigma_{\mathrm{f}}^n \leq 0 \tag{2.22}$$

The effect of a Lankford strain ratio R smaller than 1, is shown in Figure 2.7(b). The stress in the third direction in the plane stress situation is equal to zero.

2.4.3 Equivalent plastic strain and equivalent stress

In finite element simulations involving plasticity, the total strain tensor must be split into an elastic and a plastic part, in order to obtain an accurate output for the

stress tensor. The stresses and plastic strains can be calculated using an iterative scheme (e.g. a Newton iteration scheme). In this iterative scheme, it is much more convenient to use single scalar values for the plastic strain and stress, therefore an equivalent value for the strain and stress tensor must be defined. From uniaxial tensile experiments, a plastic strain state can be determined relatively easily from the elongation. A stretch λ can be translated into a strain ε by using one of several different formulations. The most used is the logarithmic or true strain, which is defined as

$$\varepsilon_{\mathrm{l}} = \ln \lambda \tag{2.23}$$

In a uniaxial stress situation, the strains in the perpendicular directions are non-zero, but can be easily determined because the stresses in these directions are zero. In case of plasticity, these strains are such that the material volume does not change (which is not necessarily the case in superplasticity, if the macro-volume is considered, see Section 2.4.1).

In a 2- or 3-dimensional stress situation, it is convenient to compare the strains and stresses in the material with the strains and stresses as found in a uniaxial situation. Therefore, an *equivalent plastic strain* can be defined, which is

$$\varepsilon^{\mathrm{p}} = \int_{t_0}^{t} \dot{\varepsilon}^{\mathrm{p}} \mathrm{d}t \tag{2.24}$$

in which $\dot{\varepsilon}^{\mathrm{p}}$ is the *equivalent plastic strain rate* and is defined in terms of the plastic part of the rate-of-deformation tensor $\mathbf{D}^{\mathrm{p}}$, which is in the case of von Mises plasticity

$$\dot{\varepsilon}^{\mathrm{p}} = \sqrt{\frac{2}{3}\mathbf{D}^{\mathrm{p}} : \mathbf{D}^{\mathrm{p}}} \tag{2.25}$$

The von Mises equivalent stress shows a comparable equation

$$\sigma_{\mathrm{y}}^{\mathrm{eq}} = \sqrt{\frac{3}{2}\mathbf{s} : \mathbf{s}} \tag{2.26}$$

where $\mathbf{s}$ represents the deviatoric stress tensor. The relationship between equivalent stress and equivalent plastic strain in a material is the same as its uniaxial stress-strain relationship.

These formulations of equivalent strain and stress become different if the Hosford yield criterion is used, but the idea is the same: constructing a useful scalar value which can be compared with a uniaxial situation. Equations (2.20) and (2.22) give the equivalent stress in the case of Hosford flow. The equivalent plastic strain can be determined by generalizing an alternative formulation

$$\sigma_{\mathrm{y}}^{\mathrm{eq}} \dot{\varepsilon}^{\mathrm{p}} = \boldsymbol{\sigma} : \mathbf{D}^{\mathrm{p}} \tag{2.27}$$

Represented as a one-dimensional stress vector and a two-dimensional rate-of-deformation tensor. Unfortunately, where the equivalent stress in case of von Mises

flow can be easily expressed in terms of the deviatoric stress tensor, in the case of the Hosford yield criterion this is not possible. The double dot product between two 2-dimensional (stress) tensors gives a scalar value, just as the equivalent stress. In the case of the Hosford yield criterion, higher (n) double dot multiplications are not possible, so a scalar value cannot be the output. The equivalent stress must therefore be expressed in the stress tensor elements only, rather than by the stress tensor as a whole.

2.5 Hydrostatic pressure dependence

Since the flow stresses of superplastic materials are very low (at the optimal superplastic temperature and strain rate this is in the order of a few MPa), it is possible to influence the flow behavior with a hydrostatic pressure. This pressure then can act as a cavity growth inhibitor [20]. This means that the material can reach a higher plastic strain before failure. In [78] it is shown that in free bulging tests, the maximum bulge height reaches higher values if a backpressure of 14 bar is applied during the forming stage.

In essence, this would mean that a non-associative flow model has to be used when considering pressure-dependent material behavior. In pressure-dependent material models, such as the Mohr-Coulomb criterion, the hydrostatic pressure is an extra variable in the description of flow. However, when considering superplastic sheet metal forming, the applied backpressure is not a variable, but it is constant during the whole deformation process. Therefore, it is not necessary to implement the effect of an applied backpressure into the biaxial flow formulation, it is sufficient to describe the application of such a pressure in the uniaxial stress-strain description only.

Since the formulation of cavities is postponed to higher plastic strains at higher backpressure, the material has a higher strength at the same plastic strain. If the void volume fraction is low, this is a minor effect, but this effect will increase if the void volume fraction becomes higher, so at higher plastic strains. The effect of an applied backpressure to a superplastic material on the uniaxial flow stress is qualitatively depicted in Figure 2.8.

2.6 Computational (super-)plasticity

Consider a material point in a structure where a prescribed strain increment is applied. If it is known that the material will behave in a purely elastic manner, it is easy to find the accompanying stress increment. The stress situation at this material point can be derived in this case from the elastic properties, i.e. Young's Modulus E and Poisson's ratio ν. The relationship between stress and strain is described by a fourth-order elasticity tensor ${}^4\mathbf{C}$ if the stress and strain are represented

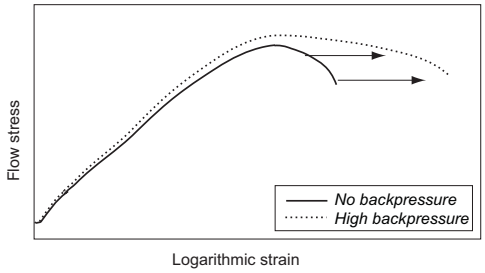

Figure 2.8: Possible material stress-strain behavior in case of a hydrostatic pressure, relative to the original material behavior.

as second-order tensors $\boldsymbol{\sigma}$ and $\boldsymbol{\varepsilon}$ respectively. This gives:

$$\boldsymbol{\sigma} = {}^{4}\mathbf{C} : \boldsymbol{\varepsilon} \tag{2.28}$$

In many cases, the elasticity tensor is represented as a second-order matrix, the stress and strain are then written as vectors $\{\sigma\}$ and $\{\varepsilon\}$. If this notation is used (as is the case in FE codes like ABAQUS), it must be noted that off-diagonal terms in $\boldsymbol{\varepsilon}$ representing the shear terms, must be doubled in the strain vector.

If the material behaves partially plastic, then the stress situation calculated with the elasticity assumption would fall outside the flow surface. Since this is a forbidden area, a correction on the stress is necessary in order to find the current stress. The general procedure to find the stress is presented in Section 2.6.1, followed by a section dedicated to the plane stress variant of the return mapping procedure in case of von Mises and Hosford flow.

2.6.1 General return mapping

This section describes the general principle of return mapping in brief terms, many papers and text books can be found which cover this topic in great detail, an extensive description can be found in [72]. In computational plasticity, a stress vector is calculated from the given strain increment by using the elastic stiffness tensor, thereby giving an elastic trial stress vector, called the *elastic predictor*. Then it is checked whether this trial stress vector lies outside the yield surface. If this is the case, this means that this point is deforming plastically. In computational terms, the stress vector has to be projected back onto the yield surface, called the *plastic corrector*.

This plastic corrector is determined by the return direction and distance. According to Drucker's postulate, the return direction is always perpendicular to the yield surface. However, the yield surface at the end of the time step in which the strain increment is applied is not known a priori, e.g. in cases where strain and

strain rate hardening are present. The return distance is expressed in the plastic multiplier $\dot{\lambda}$.
A method to find the updated stress is to draw a virtual yield surface through the point where the elastic prediction is situated. The direction perpendicular to the yield surface, in the point of the stress situation at the beginning of the time step, is chosen to be the return direction. The return distance is determined by the plastic multiplier. The advantage of this explicit, Euler forward, return mapping algorithm is that it is a relatively fast method. The main drawback is that this method is not very robust, the chosen return direction has the risk tendency to 'miss' the yield locus where it should return to. The deviation from the solution is dependent on the strain increment. The higher this strain increment, the higher the deviation, the calculated solution will drift away from the correct solution.

The implicit, backward Euler method looks for a solution where the return direction is perpendicular to the yield surface at the end of the time step in which the strain increment is applied. This is a more complicated method to implement, but generally leads to a more accurate solution. The main advantage of the Euler Backward method is that it is unconditionally stable, whereas the Euler Forward method is only conditionally stable (condition of a maximum critical time step). The return direction and distance have to be determined in an iterative process. Because of the higher stability and assumed accuracy, the Euler Backward method will be adapted throughout the rest of this section as the method to be implemented in the superplastic flow analyses.

2.6.2 Plane stress return mapping

In sheet metal forming computations, the in-plane dimensions are considerably larger than the dimensions in the thickness direction. A consequence is that the stress in the thickness direction may be considered to be equal to zero, leading to a situation of plane stress. The elasticity equation (2.28) in the case of plane stress and isotropic elastic material behavior becomes

$$\boldsymbol{\sigma}_{\mathrm{tr}} = \begin{Bmatrix} \sigma_{xx} \\ \sigma_{yy} \\ \sigma_{xy} \end{Bmatrix} = \frac{E}{1-\nu^2} \begin{bmatrix} 1 & \nu & 0 \\ \nu & 1 & 0 \\ 0 & 0 & (1-\nu)/2 \end{bmatrix} \begin{Bmatrix} \varepsilon_{xx} \\ \varepsilon_{yy} \\ \gamma_{xy} \end{Bmatrix} \tag{2.29}$$

where γ_{xy} is twice the engineering strain ε_{xy}, and $\boldsymbol{\sigma}_{\mathrm{tr}}$ is the trial stress vector. The strain in thickness direction cannot be derived from the stress in that direction, since this stress is zero. Therefore an extra constraint is necessary with respect to the plastic thickness strain. This constraint states that the material volume is conserved during plastic deformation. Therefore

$$\varepsilon^{\mathrm{p}}_{zz} = -(\varepsilon^{\mathrm{p}}_{xx} + \varepsilon^{\mathrm{p}}_{yy}) \tag{2.30}$$

The plane stress problem in case of J_2 (von Mises) plasticity is, for example, written out in [72]. Here, it is convenient to write the stresses in terms of the deviatoric

stress tensor **s**. The general implicit return mapping procedure in case of J_2 plasticity is a radial return algorithm, since the von Mises yield surface is a circle in deviatoric stress space. This means that the return direction is always pointed in the direction of the stress origin.

If another yield criterion, like the Hosford criterion, is used, as is for instance applicable to aluminum alloys at elevated temperature [54, 59] then the return direction is much more complicated to determine, since the yield surface cannot be represented as a circle. The first and second derivative of the yield surface are necessary to determine the return direction and distance in an iterative manner. In a plane stress situation, this can however lead to erroneous results if the strain increment is too high. In [47], a method is developed which makes use of a subincremental return mapping scheme. The elastic trial stress is projected onto the current yield surface in steps.

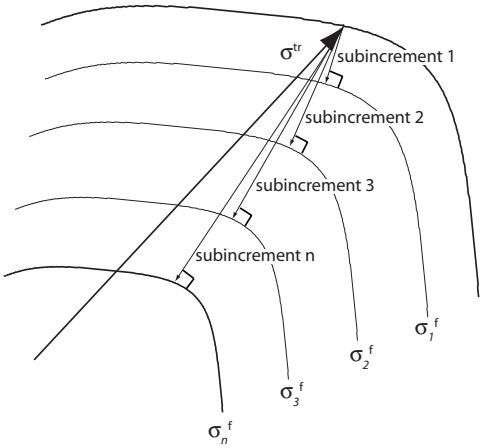

Figure 2.9: Subincremental plane stress return mapping procedure.

Figure 2.9 shows the procedure where the subincrements (1) to (n) are used. Details of the stress update procedure as used in this research project are discussed in Section 4.5. Simulating the superplastic forming process involves both geometric and material nonlinearities. If a standard material description is used in ABAQUS which covers (rate-dependent) elasto-plasticity, then automatically the solution algorithm accounts for finite deformations and strains. If, for instance, the Hosford yield criterion has to be implemented, a user-defined material description is necessary, this is called a UMAT in ABAQUS. When using such a UMAT, ABAQUS will not automatically account for these nonlinearities, only for the stress and the strain vector. All other vectors (for instance, the elastic and plastic strain vector

which should be programmed as state variables) should account for these nonlinearities within the user subroutine itself. ABAQUS provides a utility routine for this purpose, called *rotsig* [75], for rotating strain-like or stress-like vectors. The difference between these two lie in the fact that the third term in these vectors (the shear term) must be doubled or not.

2.7 Summary and conclusions

This chapter describes the properties of superplastic materials and the phenomenon of superplasticity. Superplastic forming of the RF Foil seems an attractive alternative for the manufacturing process which is currently used. The main reason for this process to apply is the extremely high plastic strains which can be reached with these materials in the forming process without failure. In the case of the RF Foil, the failure is defined by a maximum leak rate. Applying a backpressure during the forming process will increase the maximum plastic strain because void nucleation and growth is then postponed. Therefore, by increasing the backpressure during forming, leaking is far less likely to occur in a formed sheet. Superplastic forming is a slow process, but this is not an issue if only a few products have to be manufactured.

Superplastic materials come mainly as aluminum or titanium alloys. With respect to the material property radiation length, the use of aluminum is preferred above titanium. The position of the element Aluminum compared with the element Titanium in the periodic table of elements explains this preference. Some aluminum superplastic materials have been described, of which ALNOVI-1 is the best choice.

The mechanical behavior is discussed, where phenomenological and physical behavior has been distinguished. The choice has been made to use a phenomenological material description. The flow stress behavior has been split into three parts:

- the initial flow stress as a function of the equivalent plastic strain rate;
- the hardening stress, which is caused by grain growth, and is best described by a Voce hardening law;
- the softening stress, caused by void nucleation, growth and (eventually) coalescence.

When considering plane stress, a more general description of the von Mises flow behavior will be used, namely the Hosford flow criterion.

The plane stress calculations will be carried out by using an Euler Backward return mapping algorithm. This scheme is unconditionally stable and yields in general better results than the, easier to implement, Euler Forward return mapping scheme.

3. Material experiments

The accuracy of finite element analysis results involving (visco-)plasticity strongly depends on the material modeling. In order to extract the desired material properties, experiments are necessary to obtain uniaxial behavior expressed in stress-strain relationships. Biaxial experiments determine the basis for biaxial flow behavior. In this research, the superplastic aluminum alloy ALNOVI-1 is used. This chapter is dedicated to the setup and results of the uniaxial and biaxial experiments carried out on ALNOVI-1. Section 3.1 describes the experimental setup of the tensile tests and the specimen geometry. The raw data as obtained from these experiments are presented as force-displacement curves. These curves are translated into uniaxial stress-strain behavior by using inverse FE modeling of the tensile tests. The stress-strain relationships are used to design the bulge experiments. Also, void growth behavior as a function of plastic strain and strain rate is observed.

One of the most important properties to know about the material is the permeability of the deformed material with respect to gases. Before the material fails by fracture, enough voids may have been formed, grown, or may even be interlinked, to provide a leak channel through the thickness of the formed material. An experiment has been designed where circular sheets are freely blown into a, practically endless, cylindrical tool. Another extra input that can be accounted for, which which was not the case in the tensile experiments, is the application of a backpressure during the test. In Chapter 2, it was mentioned that a backpressure slows down the process of cavity growth, which has a beneficial effect on the gas permeability. Section 3.2 describes the free bulging experiments, whereas Section 3.3 presents the leak measurements from these experiments.

Section 3.4 concerns the forming of the sheets into a die, in order to obtain friction information between the sheet and the die. A die shape has been designed where the resulting thickness of the sheet can be measured in two points. The thickness ratio between these two points is a measure for the friction coefficient.

3.1 Uniaxial material experiments

The purpose of the tensile experiments is to gather information about the uniaxial mechanical behavior of ALNOVI-1. Tensile tests until fracture are performed which

are used to construct stress-strain curves. Tensile tests which have been stopped before fracture (from now on called *strain/vvf tests*) give information about the void volume fractions of the plastically strained material. First, the experimental setup is described, see Section 3.1.1. Then the results of the uniaxial tests will be presented. In the case of the tensile experiments until fracture, the force-displacement data are presented, see Section 3.1.2. In the case of the strain/vvf experiments, which are presented in Section 3.1.3, the void growth behavior is studied. Also, the strain in width and thickness direction can be measured from the strain/vvf tests, giving Lankford's strain ratio. A separate paragraph is used to discuss the strain rate sensitivity of the material.

3.1.1 Setup of the uniaxial experiments

The tensile experiments are carried out on a Hounsfield tensile testing machine, equipped with a tunnel furnace, see Figure 3.1(a). This tunnel furnace heats the specimen up to the desired temperature and a thermostat was used to retain this temperature during the test. The cross-head velocity can vary between 1 and 999 mm/min, but cannot be changed during a test. Figure 3.1(b) shows the way a specimen is attached to the cross-heads.

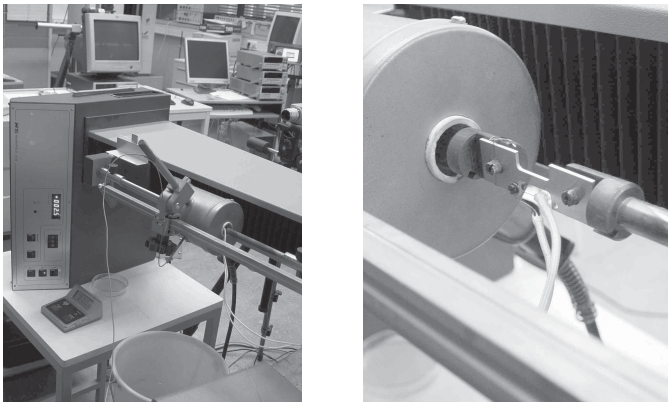

(a) (b)

Figure 3.1: Experimental setup for the tensile tests (a): tensile testing device; (b): specimen attachment.

Specimen geometry The dimensions of the tunnel furnace largely determine the geometry of the tensile specimens. The length of the effective (straining) zone must be found as a compromise between these furnace dimensions and the expected

elongation, thereby bounding a maximum specimen length. On the other hand, minimizing the strain rate prescribes certain minimum dimensions: the larger the effective length, the smaller the strain rate with equal cross-head velocity. The effective length of the specimen, excluding the 2 mm radius fillets, is 12 mm, see Figure 3.2. The specimen thickness is 0.8 mm.

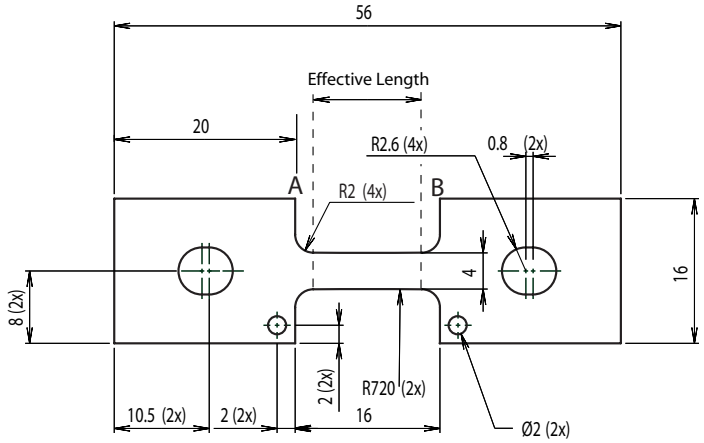

Figure 3.2: Tensile specimen geometry.

At a cross-head velocity of 1 mm/min, this would result in a strain rate of about 0.001 s^{-1}, if all of the cross-head displacement could be dedicated to the deformation of this effective zone. There are more factors which can influence the strain rate, such as deformation and distortion of the connection holes to the cross-head. The tensile specimens are manufactured by Electro-Mechanic Discharge (EMD). This process is able to create smooth cutting surfaces without too many burrs. It is also a process which does not create a heat affected zone, as is the case with e.g. laser cutting. Such a heat affected zone can negatively influence the superplastic properties of the material.

Performed tensile tests Two types of tensile experiments have been done in order to extract all the necessary output. Firstly, tensile tests until fracture at different velocities provide information concerning the stress-strain behavior at different strain rates. Secondly, strain/vvf tests have been carried out where each test is stopped at a prescribed load. The purpose of these tests is to study the dependence of the void volume fraction with respect to the plastic strain and strain rate, and also to obtain insight in the (an-)isotropy of the material.

The temperature range for optimal superplasticity is very small, values are reported varying between 500 and 530 °C. Figure 3.3 shows the typical load-displacement curves resulting from a first set of experiments, the optimal superplastic temperature for the material ALNOVI-1 is found to be 520 °C.

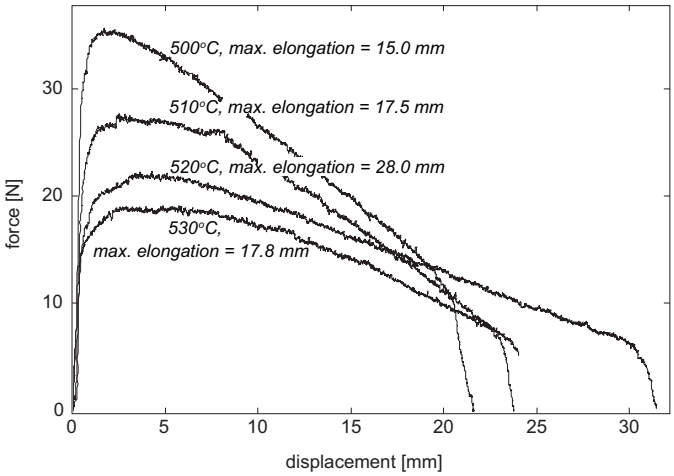

Figure 3.3: Force-displacement curves at 2 mm/min at different temperatures. Each test has been repeated two times. Elongation has been measured as the distance increase between the points A and B in Figure 3.2.

The tensile tests until fracture have been performed at five different speeds ranging from 1 to 10 mm/min, at three different orientations with respect to the material drawing direction: parallel, perpendicular and at a 45° angle. Taking into account the micromechanical superplastic deforming mechanism, which is mainly the effect of Cooperative Grain Boundary Sliding (CGBS), it is to be expected that the material behaves (planar) isotropic.

The second type of experiments concerns strain/vvf tests. It is known that internal voids will nucleate and grow inside the material with increasing plastic strain. To investigate this relationship, it is best to carry out tensile experiments until a prescribed value of the strain (elongation). Since, from Figure 3.3, it is clear that the force decreases approximately linearly over a large elongation range, it is chosen to carry out experiments until some predefined fractions of the maximum force is measured during the test. At three different cross-head velocities, experiments have been done until the force dropped to a percentage of the maximum force measured in the corresponding tensile tests until fracture. This is a better method to determine whether a large percentage of the total displacement has been

reached as opposed to stopping at a prescribed value of the displacement, since the total displacement until fracture is not known.

3.1.2 Results of the tensile tests until fracture

The tensile tests until fracture, in which the specimens were all loaded until fracture, resulted in force-displacement curves for a set of five different cross-head velocities. The first observation is that the forces are very low compared to results usually obtained in tensile tests on aluminum specimens. Figure 3.4 (a) shows the force-displacement curves of the test specimens in rolling direction for five different tensile velocities.

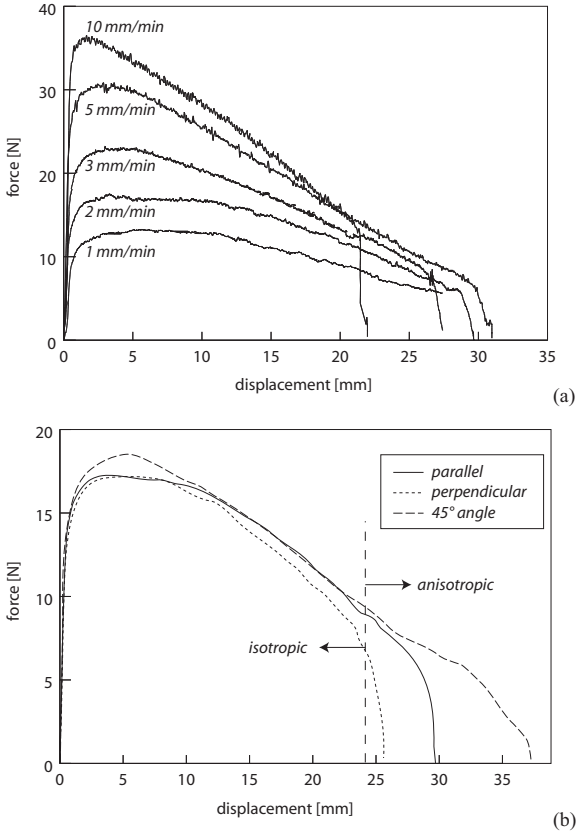

Figure 3.4: Force-displacement curves at different tensile velocities(a), and the same curves at 2 mm/min for three loading directions(b).

From this figure, the high strain rate sensitivity becomes apparent as there is much difference between the curves at different drawing velocities. Figure 3.4 (b) shows the load-displacement curves for the tensile velocity of 2 mm/min, for all three loading directions, showing the (an-)isotropy of the material. Until a displacement of 24 mm, the material can be considered planar isotropic. If the displacement exceeds this value, the three loading directions result in planar anisotropic behavior or in anisotropic damage, as can be seen in the way the three curves deviate from each other. It is supposed that at higher strains, the Grain Boundary Sliding becomes relatively more difficult, which is caused by grain growth and void formation. Therefore, conventional plastic behavior can take part in the overall deformation process, making the material anisotropic.

Uniaxial mechanical behavior Since the strain rate range in which optimal superplasticity occurs is very small, it is of importance that a predefined target strain rate will not be exceeded in superplastic forming. To carry out bulge tests with a prescribed target strain rate (which should be the maximum strain rate in the product), the pressure on the sheet should be a function of time. In order to define this pressure-time function, the stress-strain behavior of the material needs to be known. Therefore, stress-strain curves at different strain rates are constructed using the force-displacement results of the tensile tests. The stress-strain curves are constructed by inverse modeling by using the FE code ABAQUS, with which the tensile experiments have been simulated. The plasticity description which is used is the classical metal plasticity approach with strain rate dependency. The default yield criterion is then used (von Mises).

This section describes the method showing how the force-displacement curves of the tensile experiments are transformed into stress-strain curves. Figure 3.5 shows a flow diagram, starting with the raw tensile experiment output, which is in terms of force-displacement curves. Force data of the tensile experiment should be translated into stress data, thereby assuming the evolution of the current cross-sectional area of the tensile specimen during straining. This will result in the stress evolution as a function of time.

Displacement data of the tensile experiment are used to estimate the current plastic strain in time. Not all of the displacement of the cross-head can be attributed to the effective length of the specimen. A fraction of the cross-head displacement should therefore be estimated in order to determine the change in effective length.

The estimated elongation of the effective length is then used to determine the plastic strain in this area. This results in the strain evolution as function of time.

The stress-time and strain-time relationships are then coupled to construct stress-strain curves at different strain rates. These strain rates are estimated from the constructed strain-time data. These stress-strain curves are used to perform an inverse modeling of the tensile tests. The tensile tests are simulated with the

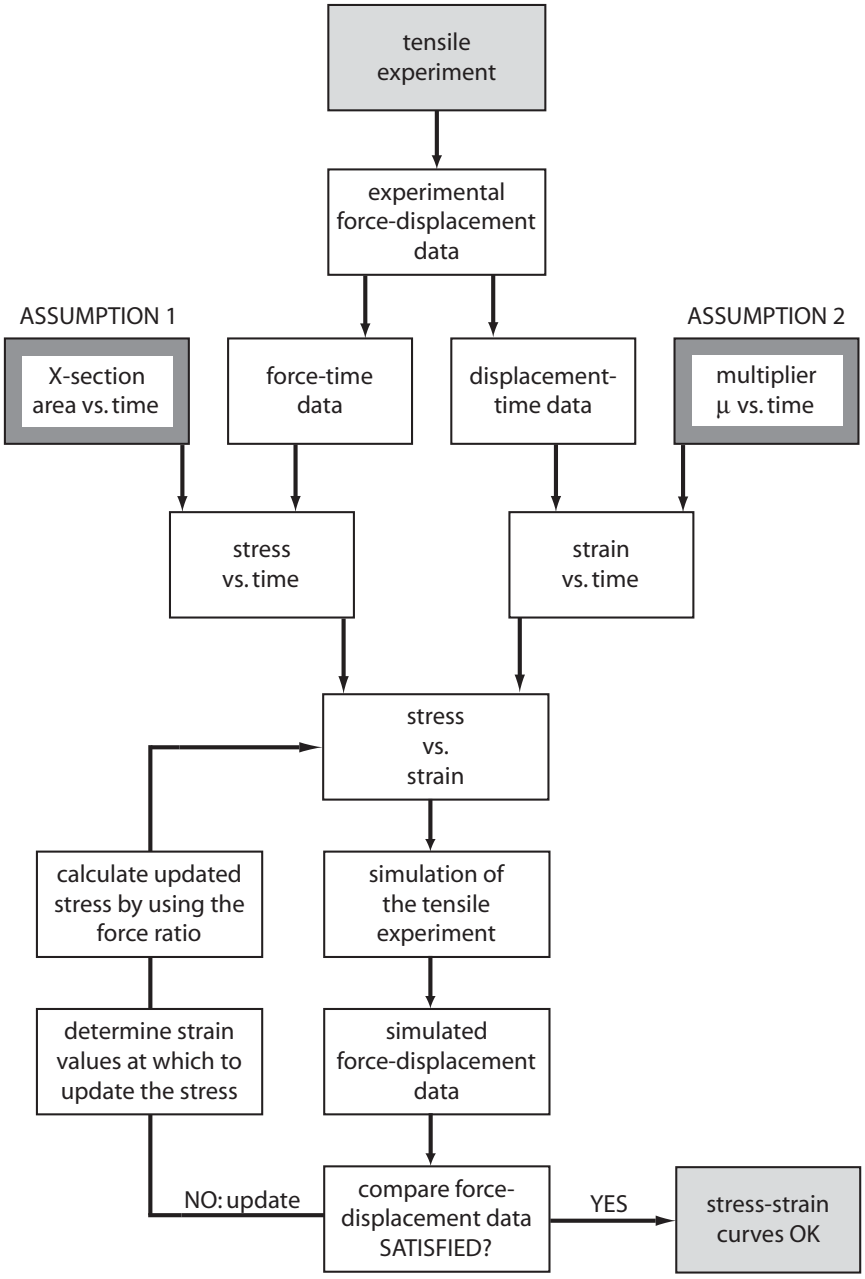

Figure 3.5: Flow scheme explaining the method of transferring force-displacement curves from the tensile experiments into stress-strain data.

constructed stress-strain data, where the output of these simulations is in terms of force versus displacement.

The simulated force-displacement output is compared with the one measured in the experiments. The deviation between both is used to improve the stress-strain behavior. This is done as follows. The tensile force at ten points on the simulated force-displacement curve is compared with the experimentally determined force at the same displacement. The strain at this displacement is then derived. The updated stress at this strain is then determined by multiplying the old stress value by the ratio between the experimentally and simulation-based force. This procedure is repeated until sufficient correspondence between the experiment and the simulation will be reached, by minimizing the RMS value between both curves at these ten points.

To estimate the stress in the tensile specimen as a function of the time, the current cross-sectional area evolution must either be known, or be estimated. Since it was not possible to monitor the width and thickness of the specimen during a tensile test (because of the surrounding tunnel furnace), the cross-sectional area must be estimated. The width and the thickness were measured at the start and the end of an experiment. The initial assumption of the cross-sectional evolution is such that both width and thickness decrease linearly with displacement (or time, since the cross-head velocity is constant). Then both the force and the estimated cross-sectional area with time are known, so the estimated stress as a function of time is known. Volume preservation is not checked here, since the goal of this procedure is only to obtain a first estimate of the stress-strain behavior.

The estimate of the plastic strain is somewhat more complicated, a few assumptions are made here. Since the flow stress is very low, it is assumed that all of the calculated strain can be considered plastic. The length of the effective zone is assumed to be 35% of the total distance between the hole centers of the specimen, which is based on a purely elastic simulation. This fraction is taken as a starting value μ_0 at zero displacement, which increases with increasing strain. Also a first simulation, where only elasticity is considered, shows that initially about this fraction of the total displacement can be attributed to the effective zone.

This multiplier μ_x, which is initially 0.35, will increase with the overall displacement. Generally, in tensile experiments, the strain rate decreases with increasing elongation, provided that the cross-head velocity is constant. However, in this case, the strain rate is assumed constant, because μ_x increases with increasing elongation. If the drawing velocity is v [mm/s], then the strain rate is

$$\dot{\varepsilon} = \frac{\mu_0 v}{l_0} \tag{3.1}$$

where l_0 is the initial effective length, and μ_0 is the initial value of the multiplier. At the lowest tensile velocity, which is 1 mm/min, this results in an initial strain rate of $4.9{\cdot}10^{-4}$ s^{-1}.

Since the calculations involved elasto-plasticity, a value for Young's modulus and Poisson's ratio are necessary. Young's modulus can be estimated from the first part of the force-displacement curves. The average value of Young's modulus is then 840 MPa, which means a considerable reduction with respect to Young's modulus at room temperature. Poisson's ratio has been assumed to have a value of 0.33.

With this information and set of assumptions, five different stress-strain curves (Cauchy stress versus true strain as in Equation (2.23)) were constructed, each of them representing the experiments depicted in Figure 3.4(a). The resulting stress-strain curves are shown in Figure 3.6(a) as the five solid curves. With this unidirectional material behavior, the tensile experiments were simulated, leading to a set of five force-displacement curves. These $F - d$ curves were compared with the experimental ones, in order to improve the unidirectional material modeling.

The simulations have been done in the ABAQUS software. The uniaxial stress-strain data were entered as a set of stress-strain points in a table. Each set of these stress-strain points was defined for each different strain rate. The von Mises flow criterion was used for the biaxial flow properties, as is the default in ABAQUS.

From the simulations, the following data were extracted to update the input stress-strain curves. Firstly, the equivalent plastic strain as a function of time is known from the simulation. This means that the equivalent plastic strain rate is also known from the simulation, which can be compared with the assumption for the strain rate for each stress-strain curve. From the simulations, it follows that the equivalent plastic strain rate in the effective zone is about 0 to 35% higher than estimated initially. That means that at a tensile velocity of 1 mm/min, the equivalent plastic strain rate, according to the simulation, decreases from $6.8{\cdot}10^{-4}$ s^{-1} at the onset of plastic strain to $5.0{\cdot}10^{-4}$ s^{-1} at the maximum plastic strain. This difference is low enough to state that it is not necessary to redefine the stress-strain curves at other strain rates. Defining a material as a set of stress-strain curves at different strain rates is valid for the whole range of strain rates, and not only for the values at which these stress-strain curves are defined.

Secondly, at each point in time, the simulated force is divided by the experimental force, giving the force ratio as mentioned in Figure 3.5. For each point of strain output (time), the stress is updated by dividing the original simulation stress input by this force ratio, in order to result in updated stress-strain curves, which are used in the next set of simulations. Each set of simulations, covering five different tensile velocities, is called an iteration.

After five iterations, the stress-strain behavior converges to a satisfying solution, represented by the dashed curves in Figure 3.6(a). The solid curves in this figure represent the initial estimates. It can be seen that the converged solution does not deviate very much from the initial estimates, except for the strain rate of $5{\cdot}10^{-3}$ s^{-1}. Figure 3.6(b) shows the comparison of the force-displacement curves for both the experimental output and the simulation output of the final solution,

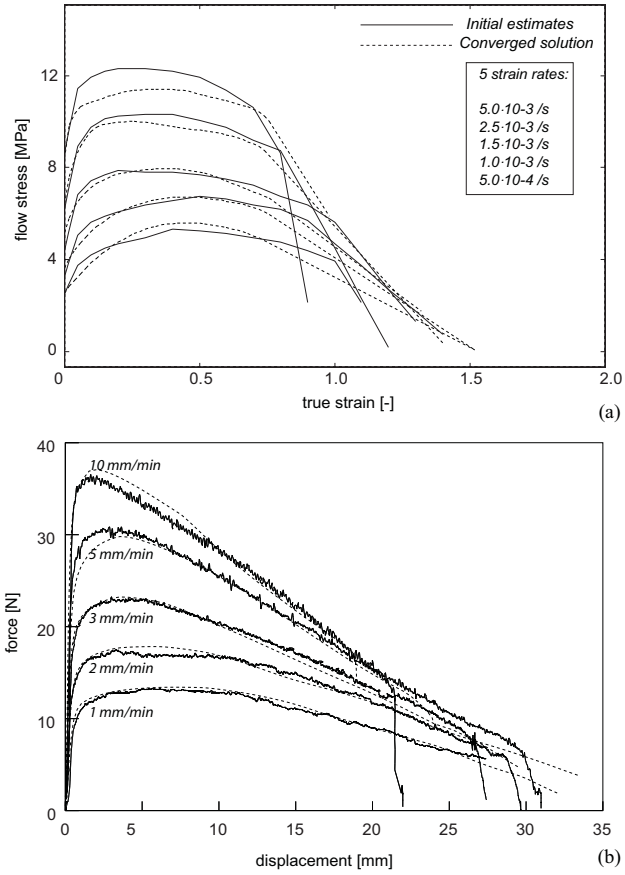

Figure 3.6: Converged solution of the stress-strain behavior after 5 iterations , compared with the initial estimates (a), force-displacement curves of the simulations compared with the experimental ones, for the converged solution (b).

represented as the dashed curves. The curves of both experiment and simulation lie close enough to each other to use the stress-strain data for the design of the bulge experiment.

3.1.3 strain/vvf tensile test results

To study the void volume fractions in the drawn specimens, cut specimens are polished and investigated under a light microscope. Electron microscope observations are also possible, but this gives so much detail and focus depth, that there

is not much contrast between void and material. This would make it very hard to estimate the void volume fraction.

The width and thickness of the specimens, leading to values for width and thickness strain, are also a measure for the amount of anisotropy of the material, expressed in the Lankford strain ratio R. In the case of pure superplasticity, the material should behave perfectly isotropic. Measurements have been done to calculate R.

From the tensile tests, also the strain rate sensitivity m has been measured, as a function of the strain rate. The strain rate sensitivity should show a maximum at the optimal superplastic strain rate. The strain/vvf tests are stopped at a prescribed value of the tensile force. This tensile force in time turned out to be highly reproducible. The tests have been performed at tensile velocities of 1, 3 and 10 mm/min. At each velocity, a test has been stopped at 60, 40, 30, 20 and 10% of the maximum drawing force.

Void volume fractions Figure 3.7 shows the typical void growth behavior in ALNOVI-1 with increasing plastic strain. To obtain an accurate view of the internal cavities and to calculate the void volume fraction, the specimens have to be polished and cleaned thoroughly. This ensures a sharp edge between the surface and the cavity, which can be used in photo editing software to count the amount of cavity pixels with respect to the total amount of pixels. The ratio between these two numbers defines the void area fraction ξ_{a}.

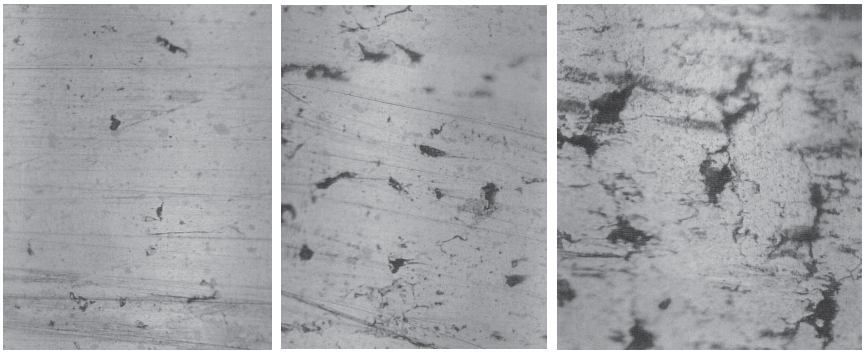

Figure 3.7: Void growth in ALNOVI-1 with increasing plastic strain, from left to right: 0.1, 0.9 and 1.3.

The void volume fraction ξ_{v} has a relationship to the void area fraction ξ_{a}. It is assumed that the void area fraction is independent on the orientation of the

observed plane. This means that

$$(1 - \xi_{\mathrm{a}})^{3/2} = (1 - \xi_{\mathrm{v}}) \tag{3.2}$$

or

$$\xi_{\mathrm{v}} = 1 - (1 - \xi_{\mathrm{a}})^{3/2} \tag{3.3}$$

In Figure 3.8, the measured void volume fractions are presented as a function of the equivalent plastic strain for different strain rates, compared e.g. with [21].

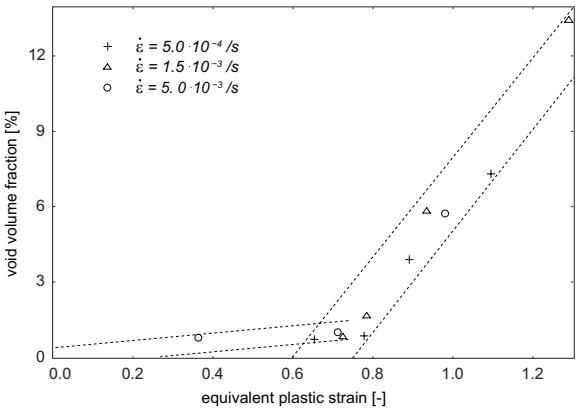

Figure 3.8: Void volume fractions as measured from the strain/vvf tensile experiments. The dashed lines mark the bounds of the measurements.

Firstly, as was also shown qualitatively in Figure 3.7, it was observed that the void volume fraction increases with increasing plastic strain. Secondly, the void volume fraction shows hardly any dependence on the strain rate, see also [13]. Thirdly, it seems that there exists a value for the plastic strain $\varepsilon_{\mathrm{tr}}$ (a transition strain), where the void volume fraction rate increases instantly, from $\dot{\xi}_1$ to $\dot{\xi}_2$ (or from slope c_1 to c_2). This can be explained by the fact that at higher plastic strains, the grains inside the material cannot accommodate enough to provide a smooth Grain Boundary Sliding process.

Lankford strain ratio From all the deformed specimens in the strain/vvf test series, the resulting width and thickness were measured. By using the initial width and thickness, the plastic strains in these directions were calculated. The Lankford strain ratio is determined as the strain in width direction divided by the thickness strain in a uniaxial experiment. A value less than 1, which is common for aluminum alloys, means that the absolute value plastic thickness strain is higher than

the absolute plastic strain in the in-plane direction perpendicular to the loading direction. Table 3.1 shows the R values in three directions, together with the average strain ratio $\bar{R}$ and the sensitivity ΔR to the loading direction. This number is very low (absolute value smaller than 0.005), meaning that the material can be considered planar isotropic.

Table 3.1: Lankford strain ratios of ALNOVI-1, including average strain ratio $\bar{R}$ and the amount of anisotropy, expressed in ΔR.

R_0	R_{45}	R_{90}	$\bar{R}$	ΔR
0.816	0.827	0.829	0.825	-0.0043

Strain rate sensitivity Equation (2.5), which describes superplasticity in its most basic form, is only valid within a small range of equivalent plastic strain rate. The value of m is however not constant and depends on this strain rate. Several methods of calculating the strain rate sensitivity exist, see for instance [28], where four different methods are discussed. A general expression for the calculation of the strain rate sensitivity is used in these methods, which is

$$m = \frac{\ln(\sigma_2/\sigma_1)}{\ln(\dot{\varepsilon}_2/\dot{\varepsilon}_1)} \tag{3.4}$$

where the subscripts 1 and 2 refer to two different loading rates. Since the stress is also dependent on the plastic strain, and not on the strain rate only, the value of m is not constant for a given strain rate. It is chosen here to calculate the strain rate sensitivity based on the maximum tensile load in the specimens, i.e. the maxima of the curves given in Figure 3.4(a). This maximum was found to be highly reproducible in the tensile tests, rather than the force at the start of the test. This results in the values for m as given in Table 3.2. The highest strain rate sensitivity is seen at a tensile velocity of 2 mm/min.

Table 3.2: Strain rate sensitivity values as calculated from the load-deflection curves. The label given in the top of the table refers to the lower value of the two strain rate values (in $10^{-4}\mathrm{s}^{-1}$) which are compared with each other.

target strain rate	6	12	18	30
m	0.43	0.70	0.55	0.25

3.2 Free bulge experiments

Biaxial experiments are done by carrying out free bulge tests, for which a dedicated experimental setup was designed and manufactured at Nikhef. Circular sheets of ALNOVI-1 were pressed with gas pressure into a cylindrical, endless die, with a diameter of 70 mm. The blanks had a diameter of 95.5 mm. The pressure-time curves are dependent on two variables: the target strain rate (6, 12 and $18{\cdot}10^{-4}\mathrm{s}^{-1}$ and the initial sheet thickness (0.3, 0.5, 0.8 and 1.0 mm). With each of these combinations, two other variables had to be controlled: the maximum duration of each test and the applied backpressure during the test. A program was developed within the software LabVIEW to control the pressures on both sides of the sheet in order to follow the pressure-time curves as closely as possible. The setup of the bulge test in terms of hardware and software will be described in more detail in Section 3.2.1. Subsequently, the results of these experiments are described, in terms of reached dome heights and apex wall thickness.

3.2.1 Setup of the free bulge experiments

ALNOVI-1 shows its optimal superplasticity at a temperature of about 520 °C. The part of the bulge forming setup which is in the vicinity of this sheet and is exposed to the same temperature, should be manufactured with a material which keeps its structural properties at this temperature. Stainless steel AISI 321L has been chosen for this purpose, which has a high strength at this temperature and which also has a good weldability.

Hardware The desired pressures in the setup are controlled by a set of digital valves, responsible for the inlet and outlet of gas. Figure 3.9 shows a schematic view together with a photo of the setup. In Figure 3.10, a cross-sectional view of the setup is shown. Three pressure vessels are present, a Top and a Bottom Container, and a Pressure Bag. Because the volumes of Top and Bottom are small, they are artificially increased by applying two buffer cylinders (CYL).

The aluminum sheet and the stainless steel have a different Coefficient of Thermal Expansion (CTE). So to ensure that the sheet stays flat without any internal stresses before forming, the sheet will be clamped in the setup after the desired temperature has been reached. This is achieved by inflating the Pressure Bag, which will then expand elastically a few tenths of a millimeter. The sheet is then pressed by the Bottom Container on a ridge in the Top Container. The resulting metallic contact is a sufficient seal between the two separate pressure chambers to prevent gas leak from one chamber to the other. The forming pressure is applied within the Bottom Container. The pressure is applied according to the pressure-time curves as calculated using a user subroutine within ABAQUS (to ensure that the target strain rate will not be exceeded). This uses the same plasticity model as mentioned in Section 3.1.2. A temperature sensor monitors the temperature

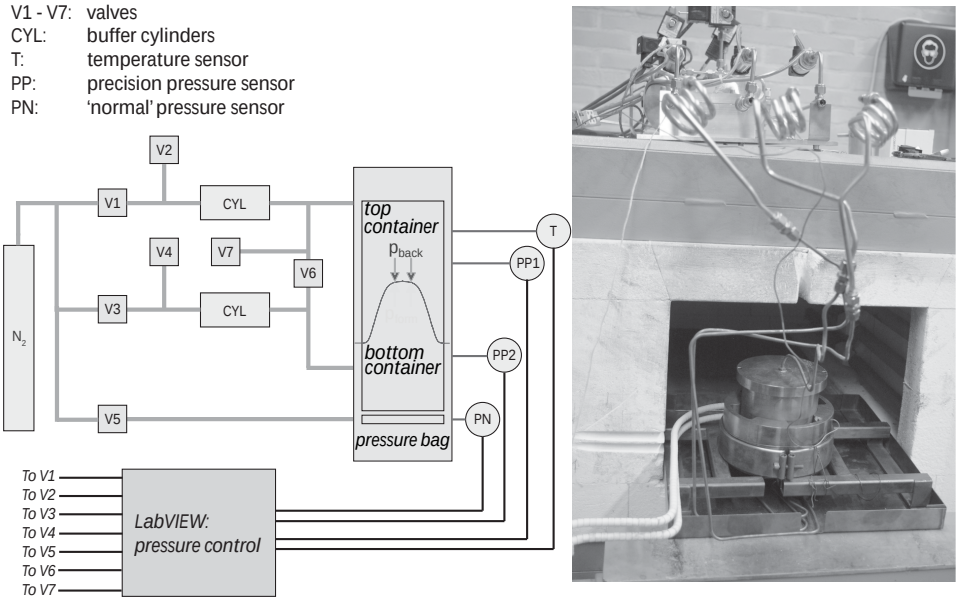

Figure 3.9: Schematic and photographic view of the bulge test setup.

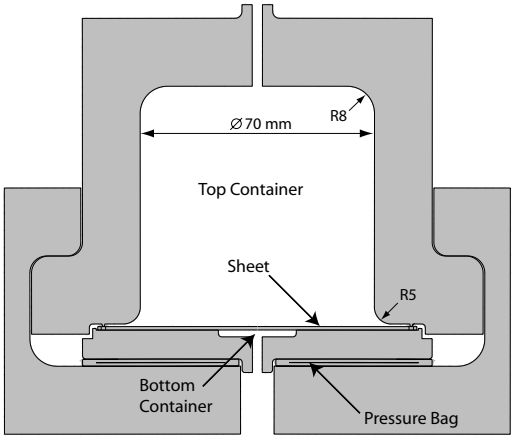

Figure 3.10: Cross-section view of the three pressure vessels.

of the containers together with the sheet. This temperature is controlled with an extra band heater surrounding the containers. Without this band heater, the fluctuations in temperature caused by the thermostat of the furnace are too high. With this band, the temperature fluctuations are within 1 °C deviation from the target temperature.

Software The bulge test is controlled by a program written in LabVIEW, which uses a temperature and three pressure readouts as input, and seven digital valve positions as output. A NI-DAQPad-6015 from National Instruments is used for the data transport from the setup to LabVIEW and vice versa.

The necessary input in this program are the target strain rate, the backpressure to be applied during the test and a time limit (i.e. duration of the test). A fixed sequence of steps is followed to obtain a properly formed cup. The detailed sequence of steps is written out in Appendix A.

3.2.2 Pressure control

If a superplastic aluminum sheet is deformed at its optimal superplastic temperature, control over the maximum strain rate is necessary. Exposing the material for a long time to a high temperature will result, however, in losing superplastic properties, so the deforming time should be as small as possible. Hence, the optimal way to deform a sheet is by taking care that at each time point, this maximum strain rate will be reached. This can be achieved by prescribing the forming pressure as a function of time [31, 48].

During the whole forming process, the maximum strain rate may not exceed a predefined target strain rate. In a nonlinear simulation, this can be achieved by prescribing the pressure load in the current time increment depending on the maximum strain rate in the process in the previous time increment. A self-developed user subroutine which was provided with the simulation reads the equivalent plastic strain rate at each increment at each element. This strain rate in the model is then compared with the target strain rate. The pressure increase or decrease on the sheet in the next increment is then a function of the ratio between the maximum equivalent plastic strain rate in the model and the target strain rate. If the maximum equivalent plastic strain rate is higher, respectively lower than the target strain rate, then the pressure will be multiplied by a value less, respectively more than 1. To prevent sudden increases and decreases at each successive time increment, this multiplication factor equals 1 in a small zone between 0.9 and 1.1 times the ratio between maximum and target strain rate. The multiplication factor is always 'damped', also to prevent sudden pressure changes due to element strain rate changes that are too severe.

The FE model consists of a quarter of a sheet, with symmetry boundary conditions applied on both symmetry edges. The sheet has been meshed with 3410

quadrilateral, reduced integration, shell elements (S4R). The outer edge of the sheet has been clamped. A friction coefficient of 0.15 has been assumed between the sheet and the radii.

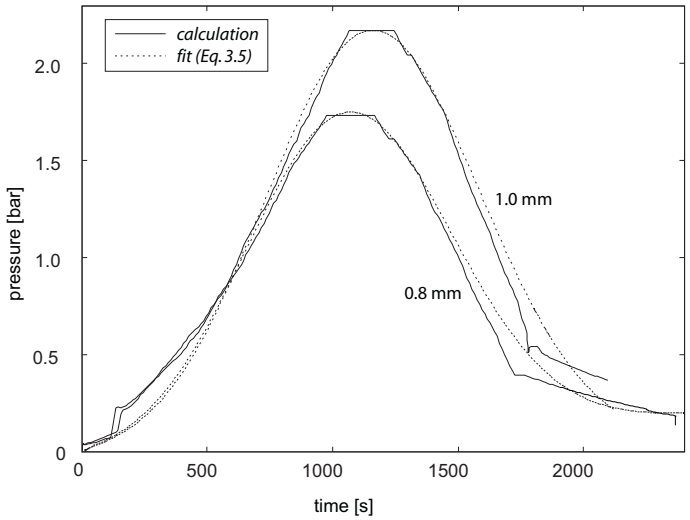

Figure 3.11: Calculated pressure-time curves to be used in the free bulge experiments for two values of the initial sheet thickness (0.8 and 1.0 mm), target strain rate is $6{\cdot}10^{-4}\mathrm{s}^{-1}$. Also the fitted curves are present (dashed curves).

Typical pressure-time curves, as a result from these simulations, are shown in Figure 3.11, in the case of sheets with an initial thickness of 1.0 mm and 0.8 mm, a bulge diameter of 70 mm and a clamping diameter of 89 mm. The target strain rate is $6{\cdot}10^{-4}\ \mathrm{s}^{-1}$. It must be noted here that side effects due to the different initial sheet thicknesses (0.3, 0.5, 0.8 and 1.0 mm) have been neglected. The reason why is because the manufacturer of the material reports similar values for bulge heights reached in their experimental setup with each of these four sheet thicknesses.

In order to control the pressure versus time in LabVIEW, an expression is necessary to fit these curves to. It is chosen to take the normal distribution function as a starting point, corrected for some extra features in these curves. The expression needs four parameters a, b, c and d to be defined according to

$$p = \left[\frac{a}{b\sqrt{2\pi}} \cdot \exp\left(-\frac{(t_\mathrm{s} - c)^2}{2b^2} \right) + dt_\mathrm{s} \right] \cdot \frac{\sqrt{t_\mathrm{s}}}{10} \tag{3.5}$$

The parameters c and b represent the mean and the standard deviation, a is a multiplication factor on the surface area under the curve (since in a normal distribution, this surface area is always equal to 1). The parameter d is chosen to make the curve asymmetric, the square root of t_s, which is the time in seconds, makes the pressure equal to zero if the time is zero, it will also make the pressure not equal to zero (asymptotically) at high t_s. All simulations end up with a resulting height of the bulge of about 40 mm before instabilities start to arise in the top of the bulge.

3.2.3 Free bulge test results

The free bulging tests are mainly carried out on the sheets with an initial thickness of 1.0 and 0.8 mm. All the sheets have been covered with a pencil-drawn grid (graphite), which makes it possible to measure the stretch at the top and the side of a formed bulge.

The results of the free bulging experiments are presented in terms of the obtained bulge height and resulting thickness values. A picture of the record holder in terms of reached bulge height is shown in Figure 3.12.

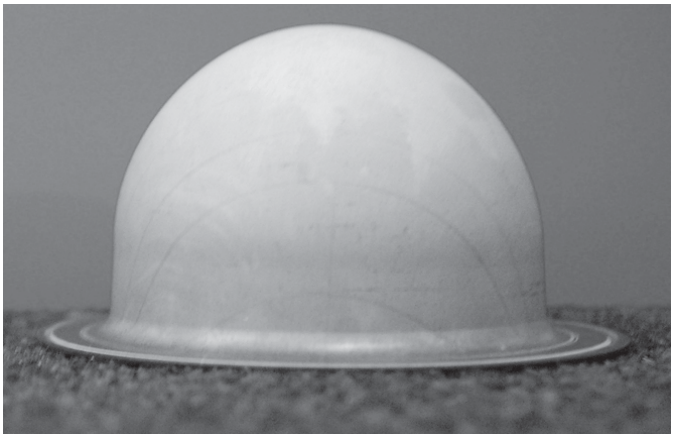

Figure 3.12: Highest bulge reached in the free bulge experiments: 53.17 mm.

A theoretical basis for the bulge tests can be developed, as was done by Syn et al [78]. This theory uses of the assumption that the thickness is the same everywhere in the product, which is clearly not the case. This was demonstrated in the work of Cornfield and Johnson [22], where the thickness distribution was made dependent on the strain rate sensitivity parameter. However, the strain rate

sensitivity in this paper is independent of the strain rate itself (so m is constant), where it is known that the strain rate sensitivity is highly dependent on the strain rate. The manufacturer of ALNOVI-1 reports an average value of the strain rate sensitivity of 0.5, this value is used to predict the bulge height as a function of the bulge apex thickness. Figure 5 of the paper of Cornfield shows a graph depicting the thinning factor (i.e. the pole thickness divided by the edge thickness) as a function of the height-to-base-ratio (i.e. the bulge height divided by the sheet diameter). Table 3.3 shows the results from this analysis in terms of bulge height versus bulge apex thickness for an initial sheet thickness of 1 mm. It is assumed that the edge thickness is an average between the apex thickness and the initial thickness, since the clamping zone is situated outside the 70 mm-diameter. This table shows the results in the case of an initial sheet thickness of 1.0 mm. The resulting apex thickness can be linearly scaled to find the thickness at other initial sheet thicknesses. In the same table, experimental results are shown as the average of the three different target strain rates mentioned before.

Table 3.3: Theoretical and measured bulge apex thickness t versus bulge height, at an initial sheet thickness of 1.0 mm.

height	10	20	30	35	40	45	49
analytical t	0.95	0.78	0.64	0.54	0.44	0.34	0.27
experimental t	0.97	0.73	0.54	0.42	0.34	0.24	0.18

It can be seen from the table that the theoretical values for the apex thickness are somewhat overestimated, indicating that the edge thickness assumption is not accurate enough, and/or the assumption of a strain rate independent m is insufficient. This shows that it is a complex task to predict bulge apex thicknesses as function of the bulge height by analytical models. The difference in apex wall thickness can be explained by the fact that the Lankford strain ratio is less than 1, as was measured from the tensile experiments. The analytical model presumes implicitly a value of 1 for the Lankford strain ratio (isotropic behavior). Figures 3.13 (a) and (b) show plots of the bulge height versus the apex wall thickness. In Figure 3.13(a) the points are categorized into different target strain rates. In Figure 3.13(b), the measured points are categorized in different values for the backpressure (0, 14, 22, and 30 bar), all for sheets with an initial thickness of 1.0 mm.

From Figure 3.13(a), it can be seen that the apex wall thickness is somewhat higher for lower target strain rates at the same bulge height. This shows the high strain rate sensitivity (viscosity) of the material, where the material has more time to obtain material from the sides to flow into the cylindrical die. From Figure 3.13(b), it is clear that at higher backpressure values, higher bulges were

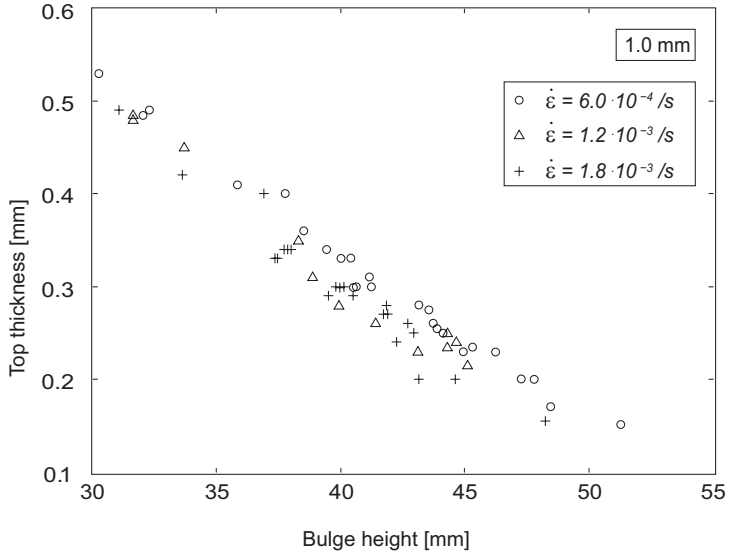

(a)

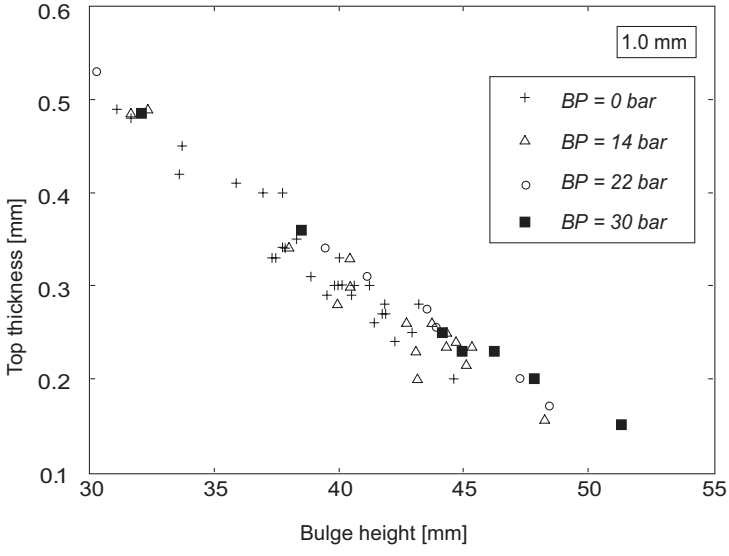

(b)

Figure 3.13: Results of the free bulging experiments, top thickness vs. height (1.0 mm), per strain rate value (a), and per backpressure value (b).

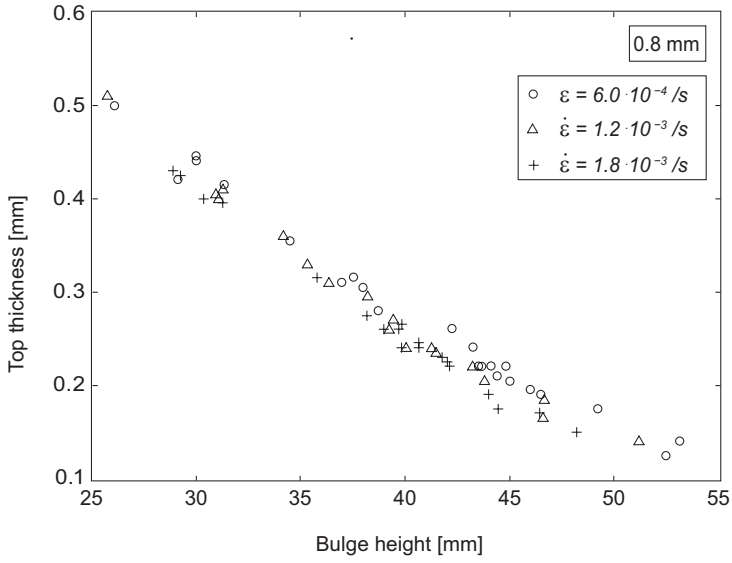

(a)

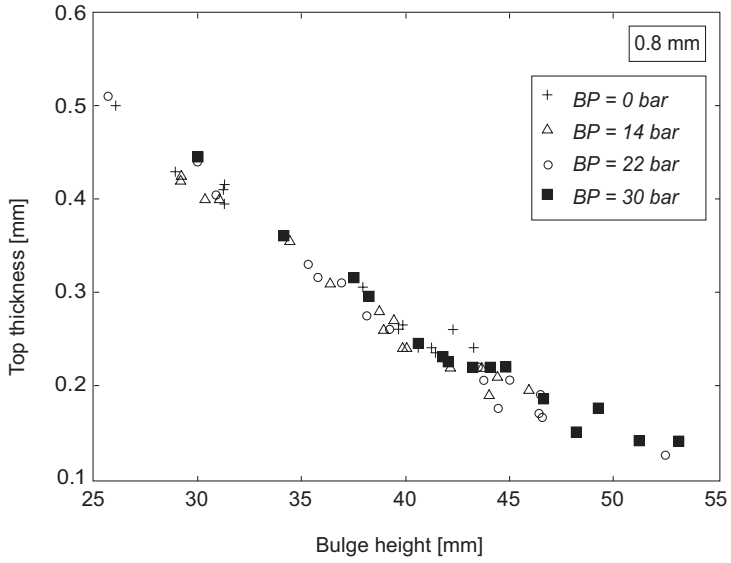

(b)

Figure 3.14: Results of the free bulging experiments, top thickness vs. height (0.8 mm), per strain rate value (a), and per backpressure value (b).

reached. This confirms the idea that a hydrostatic pressure applied on the material inhibits the void nucleation and growth with respect to plastic strain. So, the maximum plastic strain in ALNOVI-1 before fracture is dependent on this backpressure. In other words: the stress-strain behavior is dependent on the backpressure. It seems that the stress-strain curves can be thought stretched as was already schematically shown in Figure 2.8. Figures 3.14 (a) and (b) show the corresponding results for the sheets with an initial thickness of 0.8 mm. The same conclusions can be drawn for this thickness as for an initial thickness of 1.0 mm. Besides, it is observed that the maximum bulge height is the same for both thicknesses. This means that at this level of resulting apex wall thicknesses (0.15 mm), there is no influence of side effects. Also a few bulge tests were carried out on sheets with an initial thickness of 0.3 mm, with a 30 bar backpressure. These bulges also showed a bulge height exceeding 50 mm, indicating the fact that still no side effects (grain size or void size with respect to apex wall thickness) show up here. The apex wall thickness in the case of an initial sheet thickness of 0.3 mm is 0.055 mm.

From Figure 3.13, it was mentioned that at lower target strain rates, the top thickness is higher at the same bulge height. This effect is even more visible if a so-called stretch ratio r_λ is defined. This is the ratio between the measured stretch on the top of the bulge and the stretch on the side of the bulge. The stretch ratio is plotted in Figure 3.15 (a) and (b), in case of 1.0 and 0.8 mm initial thickness, respectively. From the grid which was drawn on the sheets, a stretch can be calculated, and thereby a value for the equivalent plastic strain. For each of the target strain rate values and each of the backpressure values, the bulge with the maximum height was used to determine the equivalent plastic strain. The results are shown in Table 3.4.

Table 3.4: Maximum values for the equivalent plastic strain, as calculated from the grid lines drawn on the specimens. The maximum values are presented as a function of the target strain rate and the applied backpressure during forming.

	backpressure	0	14	22	30
target strain rate	$6 \cdot 10^{-4}$	1.25	1.42	1.66	1.81
	$12 \cdot 10^{-4}$	1.23	1.47	1.57	1.77
	$18 \cdot 10^{-4}$	1.30	1.39	1.56	1.61

3.2.4 Bulge void volume fractions

A selection of formed bulges has been prepared to study the voids in the top region. The void volume fraction in the material is calculated by using Equation (3.3). The

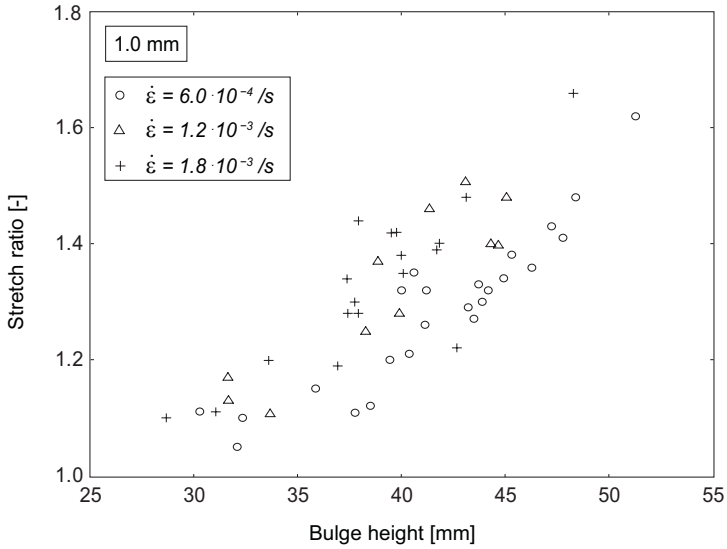

(a)

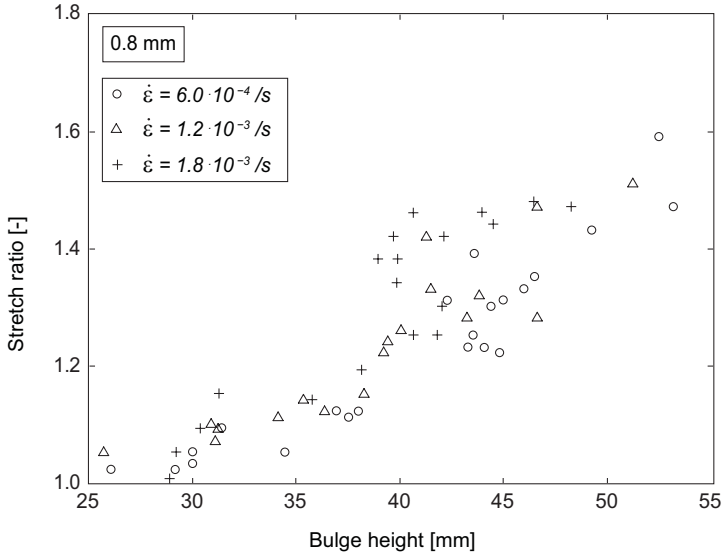

(b)

Figure 3.15: Results of the free bulging experiments, stretch ratio between top and side (1.0 (a) and 0.8 mm (b)).

results of the observations are summarized in Figure 3.16. The expected trend is visible, i.e. at higher backpressure values, the void volume fraction is lower at the same bulge height. Therefore, higher bulges can be reached at higher backpressures before failure of the material.

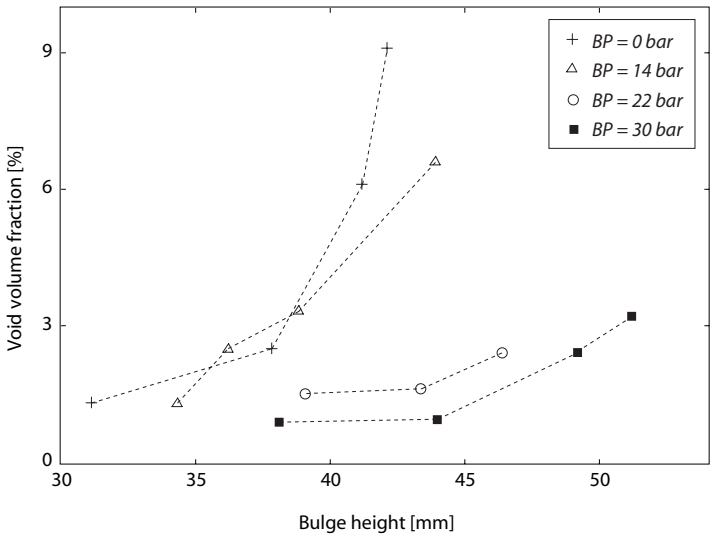

Figure 3.16: Void volume fractions of the top region of the bulges, categorized in backpressure value. The dotted lines are drawn for a clearer view.

With the pencil drawn grid on the bulges, the stretch can be measured. From the stretch, a value for the equivalent plastic strain can be calculated, taking into account that on the top of the bulge an equibiaxial stress state is present. Table 3.5 lists some values of the void volume fraction as function of the equivalent plastic strain, in case no backpressure is applied.

Table 3.5: Void volume fractions as a function of the equivalent plastic strain, without the application of a backpressure.

equivalent plastic strain	0.67	0.96	1.12	1.20
void volume fraction	1.3	2.5	6.1	9.1

If the values are compared with the void volume fraction observations from the

tensile experiments, then the following can be seen. At values for the equivalent plastic strain below the transition strain, the measured void volume fraction in the bulge is higher than in the tensile experiments. This difference is about 30 %. Above the transition strain, this difference decreases, and even becomes lower for the values measured in the bulge test. This means that the void volume fraction is not only dependent on the equivalent plastic strain, but also on the strain situation. In the bulge apex, an equibiaxial stress (and strain) situation is present. In that case, the void nucleation and growth process goes faster than in a uniaxial stress situation. However, when it comes to void coalescence, this process seems to run slower than in a uniaxial situation.

3.3 Leak tests

All formed cups from the free bulging experiments have been leak tested in an experimental setup. Within this setup, the outer side of the cup is drawn vacuum, while the inner side is filled with helium at atmospheric pressure. The leak through the formed sheet is then measured with an Alcatel ASM 181 td Leak Detector.

3.3.1 Setup of the leak experiments

The experimental setup must be designed such that it can be attached to the leak detector by means of a standardized vacuum flange. This should be at the side of the formed cup which should be made vacuum. The other side of the formed cup must be flushed with helium. It must be ensured that because of the overpressure of 1 bar at the inside, the material does not undergo plastic deformation. This has been done by measuring the bulge height before and after the leak test, and this did not result in any height differences.

Leak rate is expressed in the unit mbar·l·s^{-1} He. This unit represents the amount of helium (mbar·l) traversing the formed sheet per time unit. The leak tester neither 'knows' about the geometry to be tested, nor the pressure difference between the two sides of this geometry. If local leak rates are to be tested, a so-called sniffer is used, which can be placed onto the bulge and measures the leak rate in a small area.

3.3.2 Leak test results

The results of the leak experiments can be categorized in target strain rate or in backpressure. Since a high backpressure is thought to postpone void nucleation and growth behavior, the latter categorization is the most interesting, and is presented in Figure 3.17. What was concluded a few times before and is now visible in the leak rate results, is that a higher backpressure is beneficial for the leak rate. Table 3.6 shows the highest bulges at each backpressure value for two different leak rates:

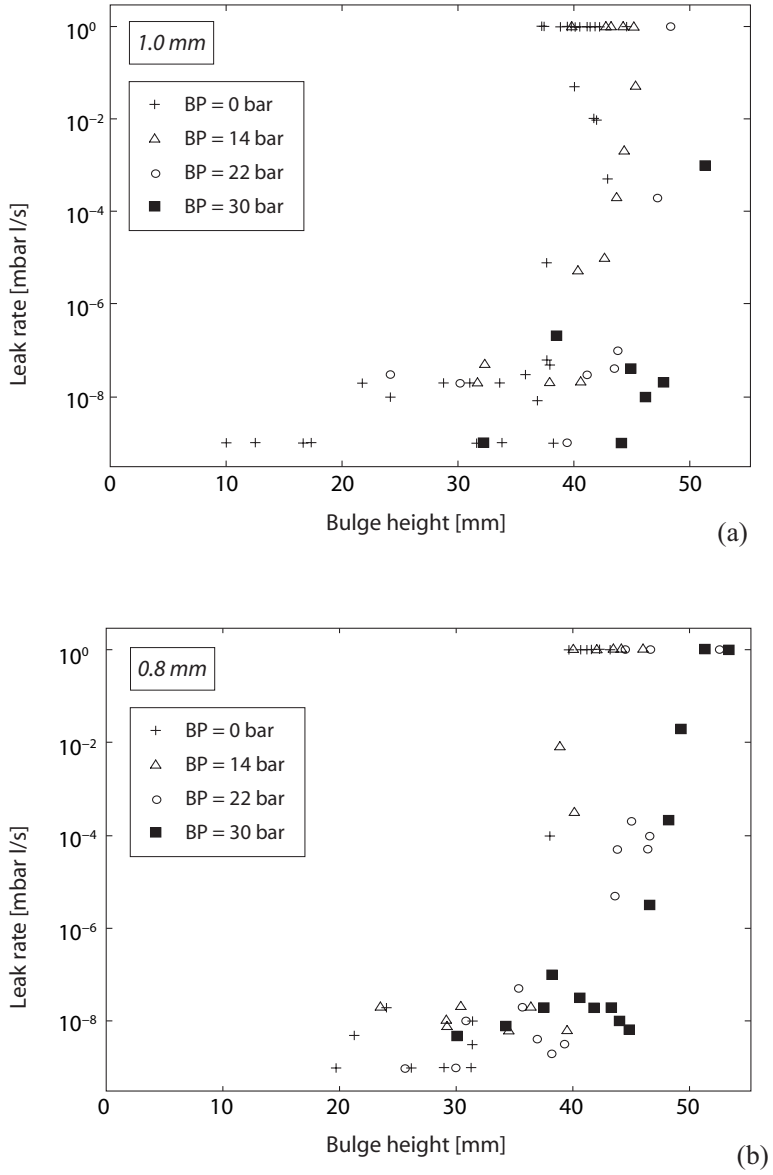

Figure 3.17: Leak test results of the formed cups, leak rate vs. bulge height, by backpressure value, at an initial thickness of (a): 1.0 mm, and (b): 0.8 mm

Table 3.6: Overview of the highest bulges with a leak rate as defined in the table, expressed in mm and mbar l/s, respectively. The bulge heights are presented as dependent on the applied backpressure (BP; in bar) and the initial sheet thickness, 0.8 and 1.0 mm.

BP		0	14	22	30
Leak 10^{-8}	0.8 mm	31.31	34.47	39.23	44.82
	1.0 mm	31.67	37.97	39.43	46.26
Leak 10^{0}	0.8 mm	37.97	40.04	46.50	49.24
	1.0 mm	41.85	42.69	47.27	51.32

firstly, a leak rate just above the minimum rate which could be measured (10^{-8} mbar l/s); secondly, the highest value of the leak rate below 10^{0} mbar l/s, since this is a value at which no holes are visible in the bulge.

If holes were visible, these bulges were not leak-tested, since this would result in a absurdly high leak value. Bulges with visible holes were all categorized under a leak value of 10^{0} mbar l/s. From this table it can be concluded, and was also expected, that a higher backpressure has a beneficial effect on the leak rate.

3.4 Die bulge experiments

When a sheet is pressed into a die to obtain a predetermined shape, the resulting geometry is dependent on the friction between sheet and die. This section describes a die design which is used for die bulge experiments, with the goal to obtain friction information. A set of experiments was designed where three variables were used, of which two were also used in the free bulge experiments: the target strain rate and the backpressure applied during the deformation process. The third variable is the friction coefficient, which is unknown beforehand. The design of the die is such that the ratio of resulting thicknesses at two points in the deformed sheet determines the value of the friction coefficient.

3.4.1 Friction in superplastic materials

Friction in superplastic forming processes has not been studied intensively, it is covered in e.g. [18, 51]. Two superplastic aluminum alloys are studied here, AA5083 and AA7475. The aim is to study the frictional behavior as a function of the target strain rate and the applied backpressure. Also, the difference between lubrication and non-lubrication was studied.

In the case of AA5083, the lowest friction coefficients were measured between the sheet and a steel die by using graphite as lubrication. In this case, the friction

coefficient was measured to be more or less constant when the backpressure or the strain rate were varied, in contrast to the other tested aluminum alloy (AA7475). The value of the friction coefficient of AA5083 against a steel die is then between 0.12 and 0.18, becoming lower at high strain rates, which are beyond the range where the superplastic deformation mechanism is active. Coulomb friction has been assumed, which will also be the case in this research.

3.4.2 Die bulge setup

The friction between ALNOVI-1 and the stainless steel die will be determined by experiments where a sheet is pressed into a shaped die. Simulations where a sheet is pressed into the die are performed at different friction coefficients. In simple terms, in the simulation which resembles the experiment the most, the correct friction coefficient was entered. This will be explained more elaborately in this section under 'die bulge pressure control'.

Die design An insert has been designed which can be mounted inside the cylindrical shaped tool, which was used for the free bulge experiments. The geometry of this axisymmetric die is shown in Figure 3.18. The dimensioning of this die is such that the friction coefficient can be determined by measuring the thicknesses at points A and B.

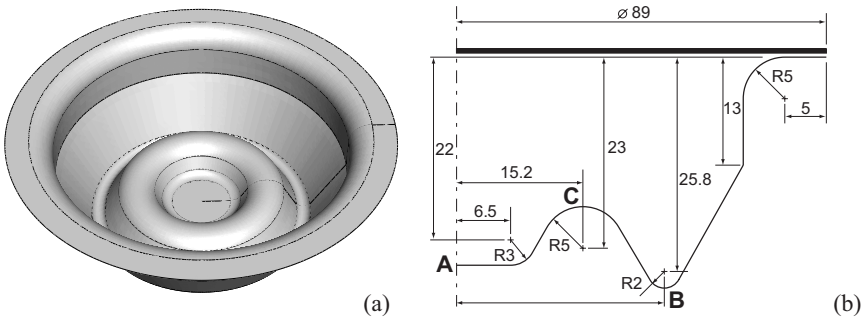

Figure 3.18: Geometry of the die used to measure the friction coefficient, (a): 3D impression, (b): cross-section, dimensions in mm.

In general, the thickness at point A is higher than the thickness in point B at high values for the friction coefficient and vice versa. The sheet to be deformed will first make contact in point C, after which point A is touched by the sheet. Then, the sheet has to be pressed into the side cavity towards point B. At low values for the friction coefficient, the material slides relatively easily along point

C, so the material flows from the mid region to the side cavity. At high values for the friction coefficient, this sliding is prevented, resulting in a higher thickness in the mid region and a lower thickness in the side cavity.

Die bulge pressure control A series of simulations have been done, with the same material properties as used for the free bulge simulations, and with the same strategy to control the target strain rate, from which a set of pressure-time curves results. The curves concerning the free bulge process only have the target strain rate as a variable, for each initial thickness value. The pressure-time curves for the die bulge experiments also use an estimated friction coefficient as variable.

So, for the three target strain rates and for five values of the friction coefficient, the pressure-time curves were determined. These are the curves to be applied in the die bulge experiments. All the curves show the same typical shape, the best way to fit this into the pressure control system in LabView is to use six straight lines, see Figure 3.19.

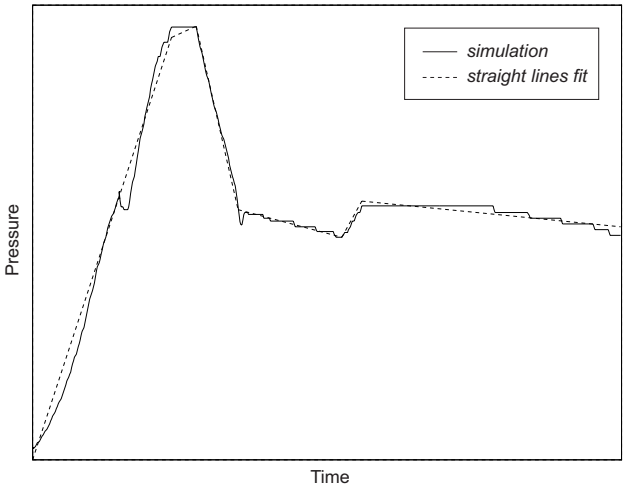

Figure 3.19: Fitting of the pressure-time curve by means of six straight lines, which are to be used as input for the die bulge experiments.

Simulations have been done using these pressure-time curves, and the correct friction coefficient for each simulation. The results of these simulations are summarized in Table 3.7, where two values are given: the resulting sheet thickness in the middle and the thickness on the position pointing towards point B, from now on called the *cavity height*. The ratio between these two thicknesses is given for each value of the friction coefficient entered in the simulation. This shows clearly

Table 3.7: Mid and cavity height as a result from simulations where different values of μ are entered. The ratio between these two thicknesses is also given.

μ	0.04	0.08	0.12	0.16	0.20
Mid thickness (mm)	0.181	0.228	0.244	0.259	0.268
Cavity thickness (mm)	0.253	0.247	0.238	0.233	0.226
Thickness ratio	0.72	0.92	1.03	1.11	1.19

that the thickness ratio increases with increasing friction coefficient. The die bulge experiments are carried out using two lubricants: one series where graphite is used, these sheets have an initial thickness of 0.5 mm. The other series is lubricated with a mixture of graphite and molybdenum sulphide, called Molykote. The sheets lubricated with Molykote all have an initial thickness of 0.3 mm. This is expected to be the thickness to be used for the forming of RF Foils, as is currently the case. Tests are performed either without the application of a backpressure, or with a 30 bar backpressure.

3.4.3 Die bulge results

Figure 3.20 shows a picture of one of the formed sheets in the die bulge experiment. From all the sheets formed in this way, the following geometric properties were measured:

- the thickness in the middle of the sheet, this part of the sheet always touches the die (point A) in every performed test;
- the cavity height. In the experiments, point B was intentionally never reached, because of the low fillet radius;
- the thickness at the cavity height. Compared with the thickness measured in the middle of the formed sheet, this gives information about the friction coefficient;
- the leak value of the formed bulges.

Table 3.8 lists the average mid thickness, and the thickness at the cavity height of the series lubricated with graphite (0.5 mm initial thickness) as a function of the target strain rate. The maximum forming time is dependent on this target strain rate: 5400 seconds at $6{\cdot}10^{-4}$ s^{-1}, 2700 seconds at $12{\cdot}10^{-4}$ s^{-1}, and 1800 seconds at $18{\cdot}10^{-4}$ s^{-1}. From the observations summarized in this table, no backpressure has been applied during the forming process. Also, the average cavity height is listed in the table. Table 3.9 shows the same observations, but now where a backpressure of

Figure 3.20: Photo of a formed sheet as a result of the die bulge experiments.

Table 3.8: Thickness results in the middle and at the cavity position of the formed sheets. The initial sheet thickness is 0.5 mm, no backpressure was applied, graphite lubrication.

$\dot{\varepsilon}_{\text{target}}$	$6{\cdot}10^{-4}$ s^{-1}	$12{\cdot}10^{-4}$ s^{-1}	$18{\cdot}10^{-4}$ s^{-1}
Mid thickness (mm)	0.274	0.265	0.263
Cavity thickness (mm)	0.222	0.223	0.228
Thickness ratio	1.23	1.19	1.15
Cavity height(mm)	24.4	24.5	23.8

Table 3.9: Thickness results in the middle and at the cavity position of the formed sheets. The initial sheet thickness is 0.5 mm, a backpressure of 30 bar was applied, graphite lubrication. * = only one measurement was available.

$\dot{\varepsilon}_{\text{target}}$	$6{\cdot}10^{-4}$ s^{-1}	$12{\cdot}10^{-4}$ s^{-1}	$18{\cdot}10^{-4}$ s^{-1} *
Mid thickness (mm)	0.280	0.270	0.270
Cavity thickness (mm)	0.237	0.220	0.210
Thickness ratio	1.18	1.23	1.29
Cavity height(mm)	23.9	25.0	25.3

30 bar was applied during the forming process. From both tables, the following can be concluded: the ratio between the thicknesses in the middle region and the cavity height does not show much variation, the average value is 1.19 if no backpressure has been applied, and 1.21 (the value of 1.29 being omitted, since this concerns only one measurement) if the 30 bar backpressure has been applied. This means that if the ratio values from the simulations are considered, that the friction coefficient is about 0.20 in the case of graphite lubrication.

Table 3.10 and Table 3.11 present the same kind of observations, but now in the case of an initial sheet thickness of 0.3 mm and a Molykote lubrication. The ratio between the two measured thicknesses in case of Molykote lubrication is lower than with graphite lubrication, meaning that Molykote results in a lower friction coefficient. The average value here is about 1.03, and if this number is compared with the simulations, a friction coefficient of 0.12 is obtained.

Table 3.10: Thickness results in the middle and at the cavity position of the formed sheets. The initial sheet thickness is 0.3 mm, no backpressure was applied.

$\dot{\varepsilon}_{\text{target}}$	$6{\cdot}10^{-4}$ s^{-1}	$12{\cdot}10^{-4}$ s^{-1}	$18{\cdot}10^{-4}$ s^{-1}
Mid thickness (mm)	0.154	0.154	0.149
Cavity thickness (mm)	0.147	0.143	0.149
Thickness ratio	1.05	1.08	1.00
Cavity height(mm)	23.7	24.7	24.5

Table 3.11: Thickness results in the middle and at the cavity position of the formed sheets. The initial sheet thickness is 0.3 mm, a 30 bar backpressure was applied.

$\dot{\varepsilon}_{\text{target}}$	$6{\cdot}10^{-4}$ s^{-1}	$12{\cdot}10^{-4}$ s^{-1}	$18{\cdot}10^{-4}$ s^{-1}
Mid thickness (mm)	0.148	0.140	0.145
Cavity thickness (mm)	0.147	0.138	0.143
Thickness ratio	1.01	1.01	1.01
Cavity height(mm)	24.2	24.5	24.5

What can be concluded in the second place from the four tables showing the experimental results, is that there seems to be no dependency of the average cavity height with respect to the applied backpressure. However, when the leak values

of the formed sheets are measured, the differences between either a 30 bar backpressure or no backpressure application becomes significant. In total, only 20 % of the sheets with an initial sheet thickness of 0.5 mm, where no backpressure was applied, was completely leak-tight. This means that there was no helium measured flowing through the sheet in a leak test, a minimum value of 10^{-9} mbar·l s^{-1} is then assumed. When the sheets were formed with a backpressure of 30 bar, all sheets turned out to be leak-tight. The same accounts for the sheets with an initial thickness of 0.3 mm. Here, 33 % of the sheets showed no leak if no backpressure was applied, 67 % of the sheets was leak-tight in case of 30 bar backpressure.

So, at first sight, the backpressure does not influence the cavity height, but if only the formed sheets are taking into account which show no leak, the backpressure is determining the cavity height. Table 3.12 shows the maximum cavity height measured in the tests at the sheets showing no leak, depending on the backpressure.

Table 3.12: Maximum cavity height at three different strain rates, only the sheets which show no leak are taken into account. Values are in mm.

$\dot{\varepsilon}_{\text{target}}$	$6{\cdot}10^{-4}$ s^{-1}	$12{\cdot}10^{-4}$ s^{-1}	$18{\cdot}10^{-4}$ s^{-1}
Max. height (No BP)	23.5	25.2	24.1
Max. height (30 bar BP)	24.4	26.9	25.3

The differences seem very small, but taken into account that the side cavity depth of the die is 27.8 mm, the difference is significant. An important thing to mention here is that the minimum wall thickness that was reached in the die bulge tests where no leak was found, is 0.140 mm. The corresponding thickness in the middle of the sheet was 0.150 mm. These values show a better result than was reached in the RF Foils produced so far, where the minimum thickness reached was 0.17 mm, but did not show leak tightness. The average thickness in the RF Foils is 0.25 mm, these experiments are an indication that thinner sheets can be produced by means of superplastic forming, leading to leak-tight constructions.

3.5 Summary and conclusions

The material ALNOVI-1 has been mechanically tested with the goal to extract results which are necessary to use in a material model. This material model must be adequate enough to perform forming simulations and predict not only the forming behavior, but also the leak rate of the formed product.

The uniaxial stress-strain behavior is extracted from tensile experiments. Five different curves (at five different strain rates) have been constructed. The maximum

strain rate sensitivity (0.70) was measured to occur at the tensile specimens loaded at a cross-head velocity of 2 mm/min. This corresponds with a strain rate of $12{\cdot}10^{-4}$ s^{-1}. The void volume fractions were measured, leading to a relationship between this property and the plastic strain. This relationship shows a transition in void growth rate. This growth rate has a lower value for plastic strains below a transition strain, and a higher value for plastic strains above this transition strain. The Lankford strain ratio was also measured, leading to a value of 0.825. This value is independent of the in-plane directions, so the material can be considered planar isotropic.

Free bulge experiments were carried out to study the forming behavior of the material. Void volume fractions and leak rates of the formed bulges were measured. These values are dependent on the applied backpressure during the forming process. The highest backpressure applied was 30 bar, which is a significant fraction of the flow stress of the material. Therefore, this backpressure postpones void nucleation/growth/coalescence, which means that a higher equivalent plastic strain can be reached without failure of the material. The highest bulge formed without the application of a backpressure was 43 mm, whereas this height was 53 mm with 30 bar backpressure applied. The highest bulges which can be considered almost leak-tight (leak rate is 10^{-8} mbar·l/s) were 31.67 mm without the backpressure applied and 46.26 mm with 30 bar backpressure applied.

Die bulge experiments were performed to investigate the frictional behavior between ALNOVI-1 and the material of the bulge setup (stainless steel AISI 321L). The friction coefficient was extracted by comparing two thickness values in the formed products. This resulted in a friction coefficient of 0.20 in the case of graphite lubrication and 0.12 in the case of Molykote lubrication. Also in these experiments, the leak rates were measured. The same conclusion as for the free bulge experiments can be drawn: the application of a backpressure has a beneficial effect on the leak rate.

The data as resulted from the mechanical experiments described in this chapter will be used to develop a constitutive model, to be used in superplastic forming simulations. The development of this constitutive model is the subject of the next chapter.

4. Superplastic material modeling

Finite element codes generally do not supply a superplastic material model, and if one does, the formulation is comparable to the one mentioned in Equation (2.5), which is for instance used in the finite element software of MARC [26]. Depending on the desired types of result and behavior to implement, it may be possible to use a predefined material type for the purpose of superplastic forming simulations. ABAQUS/Standard provides some material models in the class of metal plasticity, where isotropic or kinematic hardening can be combined with rate-dependent yield.

These material models are the subject of Section 4.1, together with a conclusion where the reasons are given for not using these models, thereby justifying the use of a user-defined material model (UMAT). This section also shows an evaluation of the use of the classical metal plasticity approach. This approach was used in Section 3.2.2 to predict the pressure-time curves for use in the bulge experiments.

The user-defined material model is described in this chapter, where the uniaxial behavior is the subject of Section 4.2. The uniaxial stress-strain behavior, as presented in Section 3.1 as a set of stress-strain curves at different plastic strain rates, is divided into three parts: the initial flow stress (at zero plastic strain), strain hardening behavior and the strain softening caused by internal void formation and growth. This section also describes the implementation of the pressure dependency in the model.

The plane stress behavior, as a result of the free bulging experiments, is described in Section 4.3, where the Hosford flow criterion is recapitulated. Since this flow criterion is expressed in the principal directions, an extra step is necessary in the material model to translate the global stress vector into these directions.

As mentioned in Chapter 1, the most important constraint of an RF Shield concerns the leak tightness. To predict if a superplastically deformed sheet will satisfy this constraint, this property should be added to the material model. This is the subject of Section 4.4.

The stress and necessary state variables should be updated every increment. Because this concerns in general a set of nonlinear equations to be solved, a Newton iteration scheme is used in the user-defined material description to solve these variables. This procedure is described in Section 4.5.

4.1 ABAQUS material models

ABAQUS provides some sophisticated material models to simulate material plasticity. One class of plasticity models is the metal plasticity group, consisting of a classical metal plasticity formulation, which can be extended by a set of additional plasticity features. These features include for instance rate-dependent yield behavior or porosity effects. This section mentions firstly the built-in material models in ABAQUS which may be suitable for the purpose of superplastic forming simulations or may provide useful information for building a user-defined material model. Secondly, the classical metal plasticity approach with strain-rate dependency will be evaluated in this section.

4.1.1 Plasticity models

Three ABAQUS/Standard plasticity models were considered which could potentially be used in a superplastic constitutive model. However, all three have a few limitations, which prevented them from being used in this research project:

- the Porous Metal Plasticity model: It is based on Gurson's porous metal plasticity theory together with a void nucleation definition. This model is valid for void volume fractions not exceeding 10 %. The void volume fraction is calculated by means of an evolution law where the void growth is dependent on the current void volume fraction. The resulting void volume fraction is used to calculate the updated yield surface with respect to the yield surface in case no voids would be present. This model is only applicable to von Mises plasticity. The main problem is that this material type is not applicable to element types which assume a plane stress condition. This means that to make use of this material type, three extra stress and strain components would be necessary by using e.g. volume elements. These components are not necessary in sheet metal forming simulations and the use of volume elements may even lead to less accurate results and also to an unacceptable increase in computation time;

- the Drucker-Prager model: this model is generally used for granular-like materials, which show different behavior in tension and compression, thereby making the material dependent on the hydrostatic pressure. The micromechanical deformation mechanism of superplastic materials can be considered as particles (granules) sliding across each other, and is also pressure-dependent. However, the problem with this material type when using elements with a plane stress formulation, is that a prescribed hydrostatic pressure cannot be applied. This means that there will be no difference in simulation results between applying the forming pressure only, and the application of a forming pressure in combination with a backpressure from the other side of the sheet;

- the Classical Metal Plasticity approach with strain-rate dependent yield option: this is a straightforward method where a set of stress-strain curves is defined at different strain rates. This method is used to predict the pressure-time curves for the bulge experiments, and is applicable to plane stress elements. Just as with the Drucker-Prager model, it is not possible to apply it to a hydrostatic pressure. This model will be evaluated in this section by simulating the free bulge experiments.

4.1.2 Evaluation of the classical metal plasticity model

This subsection shows some results of simulations of the free bulging experiment, using the classical metal plasticity model combined with the rate-dependent yield. This model was already used to predict the pressure-time curves as calculated in Section 3.2.2, resulting in a prescribed maximum value of the target strain rate. The fitted functions of these pressure-time curves, see Equation (3.5), were used as the pressure input for the simulation models (as they were also used for the experiments). In this material type, it is not possible to apply an external hydrostatic pressure which affects the material behavior. In the case of a hydrostatic pressure, the material data should be modified, but experimental values of tensile tests with the application of a backpressure are not available.

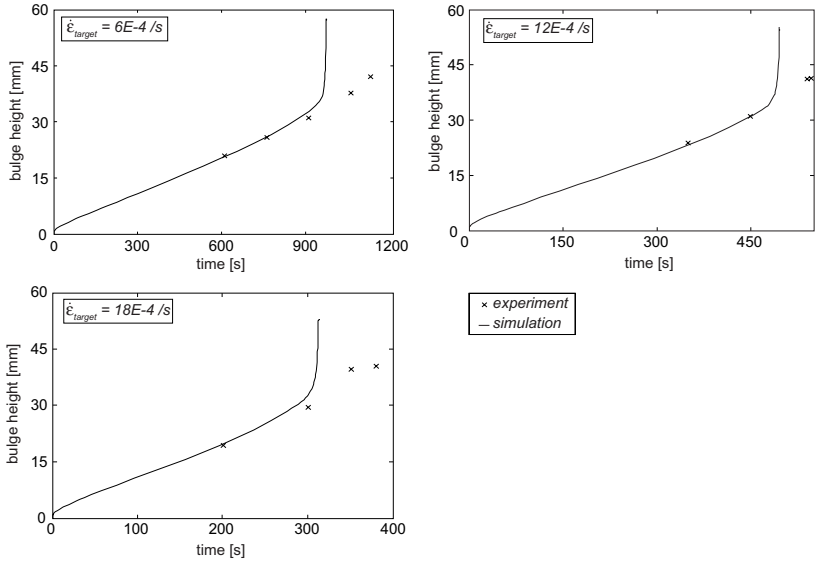

Figure 4.1: Bulge heights from the simulation and experiments compared with three target strain rate values.

Simulated bulge height Figure 4.1 shows the bulge height in the simulation versus the bulge height in the experiments, as dependent on the forming time. As can be seen, simulation and experiment agree very well until a bulge height of about 30 mm, after which the simulation becomes more unstable and shows higher bulge heights than the ones obtained in the experiments.

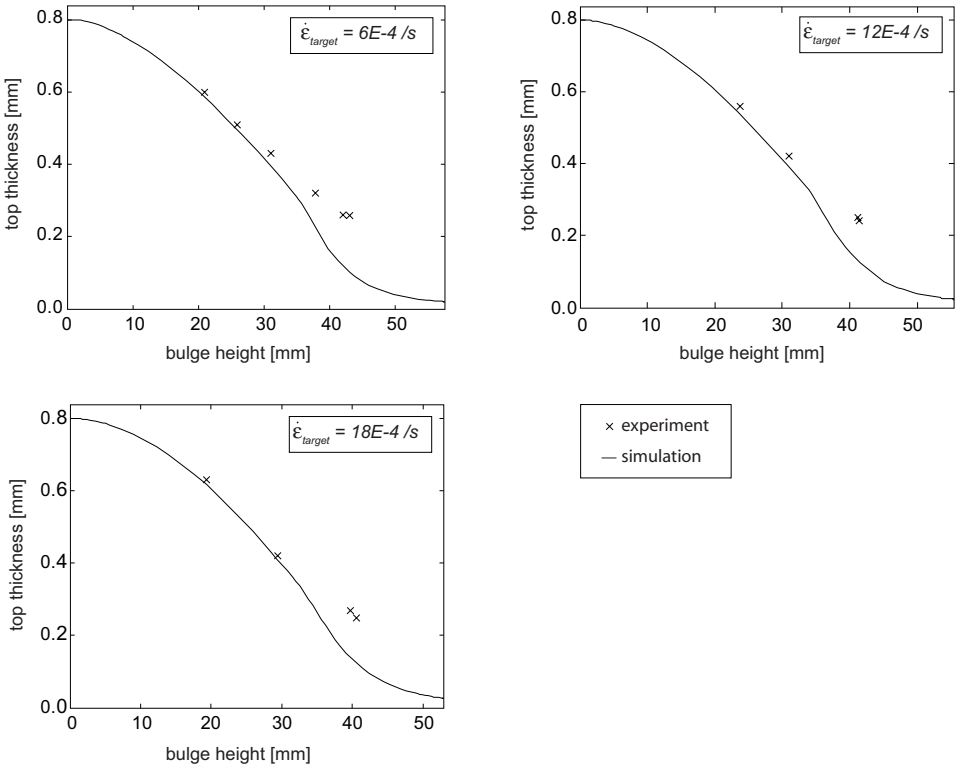

Figure 4.2: Top thickness in the bulge as a function of the bulge height, simulations vs. experiments, for three target strain rate values.

Simulated top thickness In Figure 4.2, the thickness in the top of the bulge is plotted against the bulge height, both for the simulations as for the experiments. For all three target strain rates, it can be concluded that the thickness values from the simulation are more underestimated if the bulge height increases.

A reason for the underestimation of the simulation values may lie in the fact that the material is more resistant to thinning than assumed in the simulation. In other words, the experimental Lankford strain ratio R is larger than one. This is,

however, in contrast with the results as measured in the uniaxial experiments and as found in the literature [59], where for aluminum alloys a value less than one is measured.

Another reason can be found when the resulting shape is considered at high bulge height values, see Figure 4.3. The simulation shows instable behavior, whereas the bulges obtained in the experiments do not show this shape.

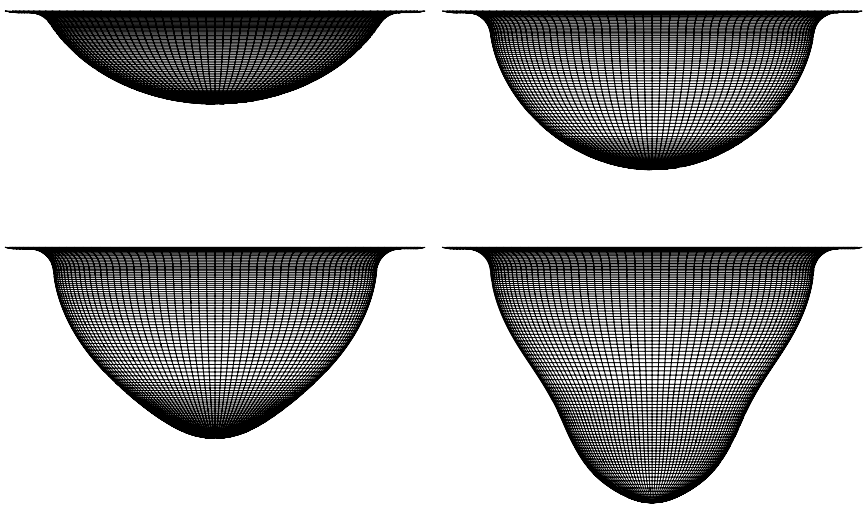

Figure 4.3: Bulge shapes in four different stages of the forming process; membrane elements have been used for the mesh, the mesh has been revolved for better visualization.

This instability effect can be postponed, or even omitted, if the material outside the top part of the bulge were to flow more than predicted by the simulation. In the top of the bulge, an equibiaxial stress state is present, whereas outside the top part close to the side wall of the cylindrical die, a stress situation is present which bears more resemblance to the plane strain state. This means that in these areas of the yield locus, the material should flow more than assumed in a von Mises description. Or, in other words, a Tresca or Hosford type of yield locus would resemble the actual biaxial flow behavior better than the standard (isotropic) von Mises assumption as used in ABAQUS. This is also the reason why the simulations show instabilities exceeding bulge heights of 30 mm. To implement a Hosford yield criterion, it is necessary to program a user-defined material model.

4.1.3 User-defined material model in ABAQUS

A user-defined material within ABAQUS is called a UMAT [75], and must be programmed with a minimum prescribed input and output. The input provided at the start of each increment (i.e. step time fraction of the total forming time) used for programming the material is a strain increment and a time increment. The (incremental) strain tensor is represented in ABAQUS as a vector with six components, or three in case of plane stress, where the shear strains are represented as the engineering shear strains γ. The output of the UMAT is at least a stress vector and the Jacobian. This Jacobian represents the current stiffness between stress and strain increment. The user is free to program the link between strain/time increment input and stress/Jacobian output. Further input and output can consist of a set of state variables which are necessary for the analysis. Examples of output to be stored in state variables can be the decomposition of the strain increment input in an elastic and a plastic part, the equivalent plastic strain and strain rate, or the void volume fraction.

This freedom in programming makes this material model independent of a prescribed yield criterion such as von Mises or Hill. In Section 2.4.2, it was already noticed that aluminum at higher temperatures does not conform to the von Mises or Hill yield criteria, but more to the more generally expressed Hosford criterion. The remainder of this chapter is dedicated to the development of the user-defined material model.

Since superplasticity is both a strain rate and a strain driven phenomenon (strain rate sensitivity m between 0 and 1), a choice could be made between programming the material as an elasto-plastic material, or based on a flow model. The elasto-plastic model (UMAT) is the most flexible option, since the stress and the state variable output can be freely programmed as function of the strain and time increment. ABAQUS provides in a user subroutine for a flow model, but this user subroutine is only intended to model uniaxial viscoplastic behavior. The implementation of a yield criterion as the Hosford criterion is not possible in this case.

4.2 Uniaxial model fitting

If a user-defined material is used to program the material deformation response, the number of parameters necessary to perform efficient analysis has to be as low as possible. For this purpose, the stress-strain data as presented in Figure 3.6 are fitted into a set of equations, each of them describing a separate characteristic in the material response.

The first characteristic is the determination of the initial flow stress σ_{y0} as a function of the equivalent plastic strain rate $\dot{\bar{\varepsilon}}^{p}$ at an equivalent plastic strain $\bar{\varepsilon}^{p}$ of zero. As presented in Section 2.3.1, a method to fit this flow stress is by

means of the Universal Superplastic Curve. The second characteristic describes the isotropic hardening of the material. Two phenomenological hardening types are often used in metal plasticity: Nadai/Swift hardening or Voce hardening. The third characteristic concerns the strain softening due to void nucleation and growth. The flow stress then becomes clearly more dependent on the void volume fraction which is in its turn dependent on the equivalent plastic strain, as was shown in Figure 3.8.

4.2.1 Initial flow stress

The Universal Superplastic Curve is a sigmoidal curve with the logarithm of the initial flow stress as a function of the logarithm of the equivalent plastic strain rate. If the generalized description of a normalized sigmoidal (i.e. S-shaped) curve is

$$y = \frac{1}{1 + \exp(-x)} \tag{4.1}$$

then a set of parameters can be used to fit this curve to the Universal Superplastic Curve for ALNOVI-1. In order to freely shape this curve, which means scaling and shifting in two dimensions each, four parameters a, b, c and d are necessary to describe the relation between $\log \sigma_{y0}$ and $\log \dot{\bar{\varepsilon}}^{p}$ as

$$\log \sigma_{y0} = \frac{1}{a + b \exp(c \log \dot{\bar{\varepsilon}}^{p})} + d \tag{4.2}$$

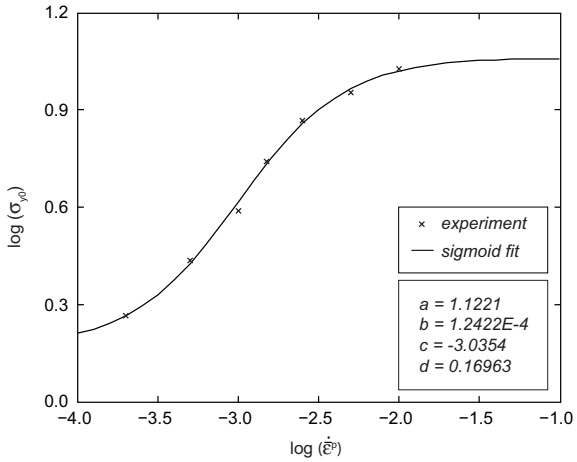

Figure 4.4: Values for the initial flow stress fitted into the Universal Superplastic Curve, as dependent on the equivalent plastic strain rate.

Figure 4.4 shows the initial yield stresses as measured in the tensile experiments, together with the best fit for the parameters a to d; their values are shown in the figure also. The highest strain rate sensitivity is found at the point where the slope has the highest value, for the given values of a, b, c and d, this occurs at a plastic strain rate of

$$\frac{\partial^2 \log \sigma_{y0}}{\partial \log \dot{\varepsilon}^2} = 0 \qquad \longrightarrow \qquad \log \dot{\varepsilon} = \frac{1}{c} \ln \left(\frac{a}{b} \right) \tag{4.3}$$

Substituting the values of a, b and c results in an optimal plastic strain rate of $1.0{\cdot}10^{-3}$ s^{-1}. The strain rate sensitivity m at this plastic strain rate is 0.676. The derivation of the first and second derivative of $\log \sigma_{y0}$ with respect to $\log \dot{\varepsilon}$ is given in Appendix B.

4.2.2 Strain hardening

Strain hardening is caused by grain growth in the material. However, the grain size itself is not measured in this material, so the hardening part will be carried out by fitting the results to an equation following a phenomenological hardening model. Two hardening models are considered here, and are qualitatively depicted in Figure 4.5.

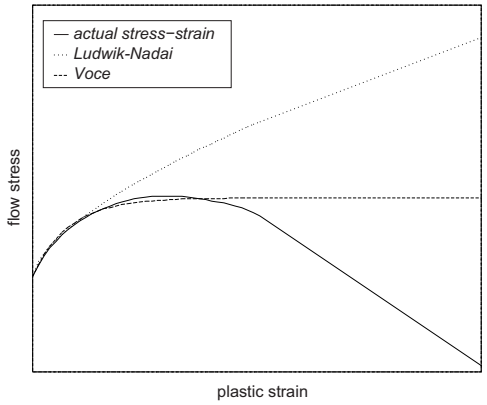

Figure 4.5: Ludwik-Nadai and Voce hardening curves, also plotted is a stress-strain curve at one strain rate for ALNOVI-1.

The first one is Ludwik-Nadai hardening, where the increase in stress is expressed by means of a hardening parameter n

$$\sigma_y = \sigma_0 + C(\varepsilon^p + \varepsilon_0)^n \tag{4.4}$$

If Ludwik-Nadai hardening were to be applied, the material would show diffuse necking in a tensile test at the point where the tensile strain is equal to $n - \varepsilon_0$. The value of the plastic strain at the point of failure is typically in the order of unity, which means that the hardening exponent should be more or less equal to 1. So the relation between uniaxial stress and plastic strain would be not far of a straight, rising line. This does not seem to be a realistic option for ALNOVI-1, since the stress clearly increases less than linearly with the plastic strain. Therefore, the Voce type of hardening seems a more convenient way to approximate the actual hardening behavior, see Figure 4.5. Voce hardening is expressed as

$$\sigma_{\mathrm{y,h}} = \sigma_0 + \Delta\sigma\left[1 - \exp\Big(-\frac{\varepsilon^{\mathrm{p}}}{\varepsilon_0}\Big)\right] \tag{4.5}$$

Here, $\Delta\sigma$ determines the *saturation stress*, the parameter ε_0 determines the approximation velocity of the hardening curve towards the asymptote. As is visible in the stress-strain curves as presented in Figure 3.6, the maximum hardening stress does not show much dependency on the strain rate. The average hardening stress as measured from the stress-strain curves is 3.21 MPa (standard deviation is 0.14 MPa); this value shall be used as a constant for the saturation stress $\Delta\sigma$.

The value of ε_0 can be estimated by considering the flow stress for each plastic strain rate at a fixed plastic strain value. This leaves ε_0 as the only unknown parameter, which can then be calculated for each value of the strain rate. The results are shown in Table 4.1. The value of ε_0 decreases as the plastic strain rate increases, therefore also the multiplication of the strain rate and ε_0 is listed in the table. In the material model, the dependency of ε_0 on the equivalent plastic strain rate should be incorporated, therefore the average value of the multiplication (see bottom row of Table 4.1) will be used as a means of calculating ε_0; this average value is $1.36{\cdot}10^{-4}$.

Table 4.1: Determination of ε_0, as dependent on the strain rate. Also the value of $\varepsilon_0 \cdot \dot{\varepsilon}$ is given.

$\dot{\varepsilon}$	5.0e-4	1.0e-3	1.5e-3	2.5e-3	5.0e-3
ε_0	0.166	0.140	0.0779	0.0583	0.0386
$\varepsilon_0 \cdot \dot{\varepsilon}$	8.30e-5	1.40e-4	1.17e-4	1.46e-4	1.93e-4

4.2.3 Strain softening

Strain softening is caused by void nucleation and growth, and it is straightforward to couple the softening stress to the void volume fraction. Figure 3.8 showed that the void volume fraction is only dependent on the plastic strain and not on the

plastic strain rate, as was observed from the tensile experiments. This void volume fraction could be considered as a bilinear relationship with the plastic strain. If it is assumed that at zero strain there are no voids present in the material, three parameters are necessary to describe this bilinear relationship: two parameters describing the two separate slopes, and one parameter which describes the plastic strain value at which the slope changes. The two slopes are called c_1 and c_2, whereas $\varepsilon_{\mathrm{tr}}$ is the transition strain.

What should also be included in the material model is the fact that voids only nucleate and grow inside the material if a net tensile stress is present. The effect of the void volume fraction on the stress softening was already shown in Equation (2.10), where three parameters n_1, n_2 and n_3 are used. So, c_1, c_2 and $\varepsilon_{\mathrm{tr}}$ describe the relationship between the equivalent plastic strain and the void volume fraction. The parameters n_1, n_2 and n_3 translate the void volume fraction in a factor between 0 and 1, to be multiplied by the sum of the initial flow stress and the hardening stress.

A problem in determining these parameters precisely, is that softening introduces instabilities in the material, and this generally leads to high variations in the experimentally determined stress-strain curves. Another problem, which has to do with numerical simulations, is that at the optimal strain rate, the maximum plastic strain which can be attained, is the highest. At higher strain rates, the maximum attainable plastic strain is lower, which would lead to strain rate softening at these high strains, and thus to numerical instabilities. Since the void volume fraction is only dependent on the plastic strain, the stress-strain curves cannot intersect each other, and thus strain rate softening cannot be present in this model. This is something which should be kept in mind, the optimum strain rate for superplastic forming follows from the value where the maximum value for the strain rate sensitivity is found, and not from the stress-strain curve with the highest plastic strain before failure. The strain rate softening was seen in the experiments, but the variation in results concerning strain rate softening is too large to represent this in the model.

Table 4.2: Parameter values related to void growth/nucleation and strain softening of ALNOVI-1.

c_1	c_2	$\varepsilon_{\mathrm{tr}}$	n_1	n_2	n_3
0.015	0.141	0.74	5.24	0.946	1.272

Table 4.2 lists the value of the parameters mentioned here. The value of the parameters, as follows from the fitting procedures (initial flow stress, hardening, and softening), results in the uniaxial stress-strain behavior as depicted in Figure 4.6.

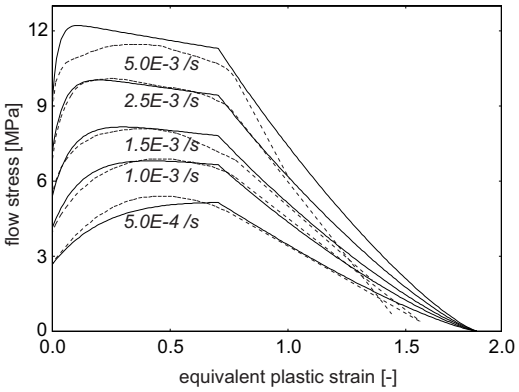

Figure 4.6: Uniaxial stress-strain behavior for different strain rates as a result of the fitted parameter values. The dashed curves are the curves as had been entered for the Classical Metal Plasticity model.

4.2.4 Pressure dependency

The effect of applying a hydrostatic pressure during the deformation process is that void nucleation and growth are inhibited. It is assumed that the initial flow stress and the Voce strain hardening are unaffected by a hydrostatic pressure, as is also the case for the softening stress as a function of the void volume fraction. What is affected, is the void volume fraction as a function of the plastic strain, which means that the values for c_1, c_2 and $\varepsilon_{\mathrm{tr}}$ may change with the application of a backpressure. The backpressure influence cannot be deduced from the tensile experiments, and hence not from the uniaxial behavior of the material established so far. The most flexible way to incorporate the backpressure is to modify these three parameters with a multiplication factor which is dependent on the value of the backpressure. If, in theory, the backpressure were to be infinitely high, there would be no void nucleation and growth at all, leading to zero values of c_1 and c_2. The transition strain $\varepsilon_{\mathrm{tr}}$ is then undetermined, the softening part of the material model as described here would not be present.

To let the values of c_1 and c_2 decrease asymptotically to zero when the backpressure rises to infinity, two extra parameters c_3 and c_4 can be introduced, which are used as modification parameters according to

$$c_1^{\mathrm{BP}} = \frac{c_1}{1 + c_3(p_{\mathrm{h}} - 1)} \tag{4.6}$$

$$c_2^{\mathrm{BP}} = \frac{c_2}{1 + c_4(p_{\mathrm{h}} - 1)} \tag{4.7}$$

where p_h is the applied backpressure in bars. The transition strain is modified by a parameter c_5 according to

$$\varepsilon_\mathrm{tr}^\mathrm{BP} = \varepsilon_\mathrm{tr}[1 + c_5(p_\mathrm{h} - 1)] \tag{4.8}$$

The effect of the introduction of the three parameters c_3, c_4 and c_5 is shown in Figure 4.7.

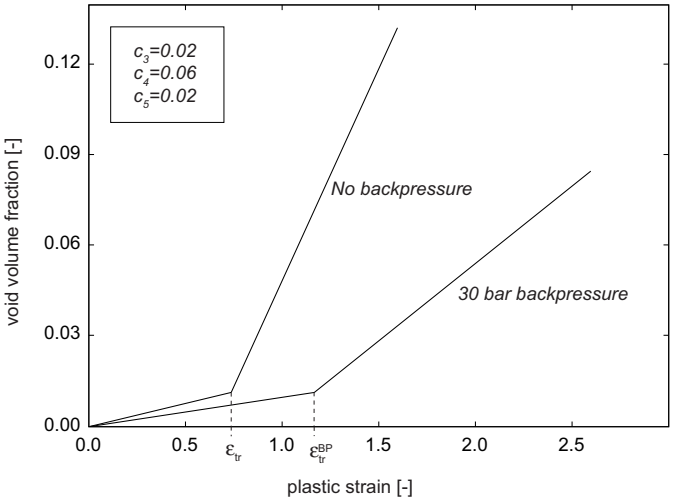

Figure 4.7: Void volume fraction in the material with and without the application of a backpressure. If $c_3 = c_5$ then the void volume fractions at both transition strains are equal.

4.3 Plane stress material model

The von Mises flow criterion is not accurate enough to describe the biaxial behavior of aluminum alloys at elevated temperature. By application of a more general non-quadratic flow criterion, better simulation results can be obtained in these cases. For ALNOVI-1, which shows isotropic mechanical behavior at superplastic temperatures, the Hosford flow criterion is used.

The mechanical behavior of ALNOVI-1 at 520 °C is dependent on the hydrostatic pressure. Since this applied backpressure is constant during the deformation process, a non-associative flow model is not necessary to use. The calculation of the flow direction in the Hosford flow criterion, which is defined only in the principal directions, is the subject of the first part of this section.

The void volume fraction was made dependent on the equivalent plastic strain as measured from the tensile experiments. In these tests the equivalent plastic strain was the same as the plastic strain in the tensile direction. In a biaxial stress/strain state, this relation will generally not be true, e.g. if the stress state is becoming more compressive, the void volume fraction will not increase, but the equivalent plastic strain does increase. The void volume fraction description in a biaxial stress/strain state is the subject of the second part of this section.

4.3.1 Flow directions

Since the Hosford flow criterion is described only in the principal stress directions, see Equation (2.22), it is not possible to derive the updated flow direction from the global xyz coordinates directly. Instead of rotating the global stress situation at the beginning of a time increment and rotating back to an updated angle (which means an extra variable) the stress invariants can be used to determine the flow direction. The first and second invariants I_1 and I_2 of a stress vector in the case of a plane stress situation are

$$I_1 = \sigma_{xx} + \sigma_{yy} = \sigma_1 + \sigma_2 \tag{4.9}$$

$$I_2 = \sigma_{xx}\sigma_{yy} - \sigma_{xy}^2 = \sigma_1\sigma_2 \tag{4.10}$$

So, σ_1 and σ_2 can be written in terms of the stress invariants as

$$\sigma_i = \frac{I_1 \pm \sqrt{I_1^2 - 4I_2}}{2} \qquad i = 1, 2 \tag{4.11}$$

The flow direction $\partial\phi/\partial\boldsymbol{\sigma}$ can be written as

$$\frac{\partial\phi}{\partial\boldsymbol{\sigma}} = \frac{\partial\phi}{\partial\sigma_1}\Big(\frac{\partial\sigma_1}{\partial I_1}\frac{\partial I_1}{\partial\boldsymbol{\sigma}} + \frac{\partial\sigma_1}{\partial I_2}\frac{\partial I_2}{\partial\boldsymbol{\sigma}}\Big) + \frac{\partial\phi}{\partial\sigma_2}\Big(\frac{\partial\sigma_2}{\partial I_1}\frac{\partial I_1}{\partial\boldsymbol{\sigma}} + \frac{\partial\sigma_2}{\partial I_2}\frac{\partial I_2}{\partial\boldsymbol{\sigma}}\Big) \tag{4.12}$$

where $\partial\phi/\partial\sigma_i$ can be derived from the Hosford flow criterion, this is

$$\frac{\partial\phi}{\partial\sigma_i} = \frac{1}{(R+1)\sigma_{\text{eq}}^{(n-1)}}\Big[\sigma_i^{(n-1)} \pm R(\sigma_1 - \sigma_2)^{(n-1)}\Big] \qquad i = 1, 2 \tag{4.13}$$

in which σ_{eq} is the equivalent stress. Further,

$$\frac{\partial\sigma_i}{\partial I_i} = \begin{bmatrix} \frac{1}{2}(1 + \frac{I_1}{2\sqrt{I_1^2-4I_2}}) & \frac{-1}{\sqrt{I_1^2-4I_2}} \\ \frac{1}{2}(1 - \frac{I_1}{2\sqrt{I_1^2-4I_2}}) & \frac{1}{\sqrt{I_1^2-4I_2}} \end{bmatrix} \qquad i = 1, 2 \tag{4.14}$$

To complete the terms in the equation for $\partial\phi/\partial\boldsymbol{\sigma}$:

$$\frac{\partial I_1}{\partial\boldsymbol{\sigma}} = \begin{bmatrix} 1 & 0 \\ 0 & 1 \end{bmatrix} \tag{4.15}$$

$$\frac{\partial I_2}{\partial\boldsymbol{\sigma}} = \begin{bmatrix} \sigma_{yy} & -2\sigma_{xy} \\ -2\sigma_{xy} & \sigma_{xx} \end{bmatrix} \tag{4.16}$$

4.3.2 Biaxial-dependent void volume fractions

The values of the parameters c_1 and c_2, which represent the slopes in the bilinear relationship between the void volume fraction and the equivalent plastic strain, are determined from the tensile (uniaxial) experiments. If the same equivalent plastic strain is present, but now as a result from a compressive test, then it is obvious that no voids would nucleate or grow inside the material. Void nucleation and growth (and eventually coalescence) is a reaction to tensile stresses or strains. In compression, the parameters c_1 and c_2 are zero, or even negative. A negative value means that already existing voids in the material, caused by earlier tension, may be closed again.

Using the strain tensor Instead of using the equivalent plastic strain for the void volume fraction relationship, it may be better to take the plastic strain tensor as a whole into account to determine the change in void volume fraction. The relationship to describe ξ would then look like

$$\xi = c_i^* \cdot (\boldsymbol{\varepsilon}^{\mathrm{pl}} : \mathbf{I}) \qquad i = 1, 2 \tag{4.17}$$

Below the transition strain $\varepsilon_{\mathrm{tr}}$, this constant is called c_1^*, above this strain it is c_2^*. This constant can be calculated from the uniaxial strain state. In the uniaxial case, $\varepsilon_{xx}^{\mathrm{pl}}$ is equal to the equivalent plastic strain and $\varepsilon_{yy}^{\mathrm{pl}} = -(1/(R+1)) \cdot \varepsilon_{xx}^{\mathrm{pl}}$. This means that

$$c_i = c_{1,2}^*(1 - \frac{1}{R+1}) \qquad i = 1, 2 \tag{4.18}$$

So

$$c_i^* = \frac{R+1}{R} c_i \qquad i = 1, 2 \tag{4.19}$$

The transition strain was also defined in terms of the equivalent plastic strain, but in this case it is less obvious than for c_1 and c_2 that this strain is influenced by plastic strain tensor values. This parameter will therefore be held constant in the user-defined material model.

Using the stress tensor The stress tensor can be used as an alternative in the description of the biaxial-dependent void volume fraction. One advantage of using the method of the stress tensor is because the stress is zero in the transverse direction in a uniaxial stress/strain situation. The values of c_1 and c_2 are not modified in this stress situation, and the values of these parameters can be dependent on the angle ζ as depicted in Figure 4.8. The effective values c_1^* and c_2^* are larger than c_1 and c_2 if the second principal stress is positive, and become smaller if the second principal stress is negative. These effective values are determined by two extra parameters x_1 and x_2. In Table 3.5, a void volume fraction of 1.3 % has been reported at an equivalent plastic strain of 0.67. This means that in an equibiaxial

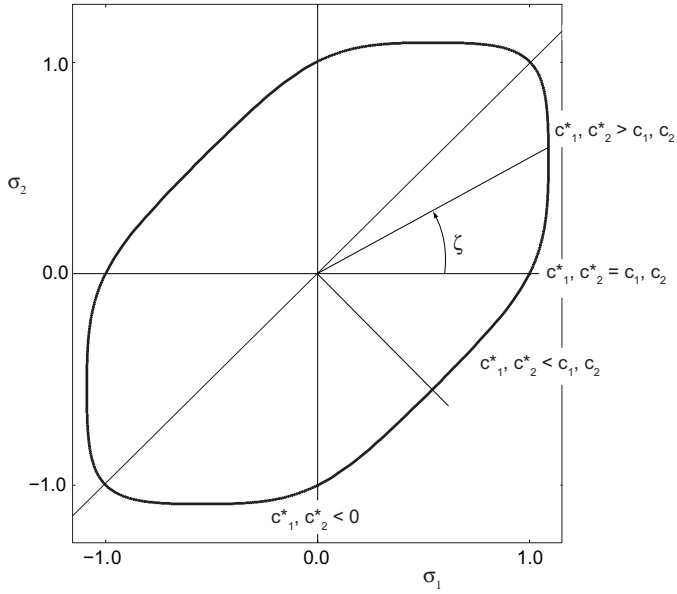

Figure 4.8: Dependence of the parameters c_1 and c_2 as a function of the stress state.

state the value for the parameter c_1 is then $0.013/0.67 = 0.0194$ instead of 0.015. If the increase of c_1 is proportional to the angle ζ, then in an equibiaxial state this angle is $\pi/4$. So, if x_1 is determined by

$$c_1^{(\zeta)} = c_1 + x_1\zeta \tag{4.20}$$

then x_1 is equal to $5.61{\cdot}10^{-3}$.
From the same table it was observed that the void volume fraction increases at an equivalent plastic strain higher than the transition strain, but at a lower rate than in the uniaxial case. So, a negative value for x_2 is expected. Taking the value of the equivalent plastic strain of 1.12 in this table, corresponding with a void volume fraction of 6.1 %, then a value for x_2 of -0.0233 is calculated.

4.4 Leak implementation

The most important characteristic of an RF Foil is the leak tightness. To predict the leak of a superplastically deformed sheet, this property has to be taken into account in the user-defined material model. It is clear that leakage occurs if the gas can find a way along the cavities of the material. This section is aimed at

finding a relationship between the leak and the void volume fraction. The void volume fraction is determined by the plastic strain vector only, which would make it possible to couple the leak directly to the plastic strain in the material.

4.4.1 Leak prediction

Gases can transport through a sheet or membrane by two phenomena: gas diffusion and gas flow. If the diameter of the channels through which the gas travels is smaller than the *mean free path* [79] of the gas molecules, then diffusion is the main transport possibility. In general, the mean free path is about 100 nm at atmospheric pressure. If voids are responsible for the gas leak of the RF Foil, then diffusion is not the main cause in case of gas leak. So, it is assumed here that in case of a gas leak, the gas flows through a channel which is provided by coalescence of the voids. The gas flow through a channel is dependent on the radius and length of the channel, and the pressure difference between both ends [88]:

$$Q = \frac{\pi d_c^4 \Delta p}{8 \eta l} \tag{4.21}$$

where Q is the flow (leak) rate, d_c is the diameter of the channel, Δp is the pressure difference, η is the dynamic viscosity of the gas and l is the length of the channel. The diameter of the channel (or the summation of all channels through the sheet) is related to the void volume fraction. The channel length is related to the resulting sheet thickness. This means that both result types, void volume fraction and sheet thickness, are responsible for the value of the leak rate.

Relating the leak to the void volume fraction has one disadvantage: the void volume fraction measurements on the formed bulges show a high variance. This may make the leak prediction not accurate enough, but two options are possible. One option is to describe the leak on the safe side of the void volume fraction, the other is to use the mean value of the void volume fraction. The risk is that a formed RF Foil may show a leak value which is too high, but since the amount of products needed is very small, the only risk is that the sheet has to be pressed a second time, or even maybe a third time. Or, in general: the permitted percentage of scrap products is higher if the production series is smaller. It is also possible to couple the leak to the plastic strain, but the downside of this method is that a dependence on the applied backpressure is also necessary. Since the void volume fraction is less at the same plastic strain at a higher value for the backpressure, it is assumed that the leak value description as a function of this void volume fraction is independent of the backpressure.

The gas flow equation (4.25) is valid for straight channels. It is, however, not to be assumed that the flow channels through the sheet are straight. A number of curves and corners will occur, which will be dependent on the channel length and thus on the sheet thickness. Each curve or corner means an extra pressure drop inside the channel because flow energy is lost when the gas flow bends.

4.4.2 Leak description in UMAT

A relationship must be found between the leak rate L (or $\log L$), the void volume fraction ξ and the resulting sheet thickness t. Table 4.3 shows a series of leak measurements ($\log L$) together with the corresponding void volume fraction ξ and the sheet thickness (t) values. A linear regression model has been constructed between these quantities, see e.g. Chapter 2 in [58].

Table 4.3: Values for $\log L$ as a function of the void volume fraction ξ and the sheet thickness t (in mm).

ξ	0.0087	0.0094	0.013	0.015	0.016	0.017
t	0.295	0.22	0.41	0.26	0.22	0.31
$\log L$	-9.0	-8.0	-9.0	-8.5	-5.3	-7.7
fit	-9.2	-8.1	-9.5	-7.0	-6.2	-7.0
ξ	0.023	0.024	0.025	0.025	0.032	0.033
t	0.19	0.15	0.24	0.305	0.14	0.26
$\log L$	-4.0	-3.0	-3.5	-4.0	0.0	-2.1
fit	-3.7	-2.9	-3.8	-4.6	-0.4	-1.6

It is no use to fit a linear regression model with the leak value itself involved, because all of the values are in that case very close to zero; there would be no significant difference between all values. Therefore, the logarithm of the leak is used in the regression model. The significance of regression is expressed in the coefficient of multiple determination R^2. A better representation is an adjusted value, R^2_{adj}, because this value does not change if more observations are added. The closer R^2 or R^2_{adj} to 1, the better the linear regression model. The meaning of both these numbers is explained more elaborately in Chapter 6.

The best linear fit obtained is

$$\log L = 297.48\xi - 12.52t - 8.19 \tag{4.22}$$

The fitted values according to this relationship are also presented in Table 4.3. The coefficients of multiple determination are close to 1: $R^2 = 0.967$ and $R^2_{\text{adj}} = 0.961$. This means that this linear regression model describes the leak in terms of void volume fraction and sheet thickness accurately enough.

The leak rate will be determined on an elemental basis, this means that the elemental area is also important. All the separate elemental leak results added together give the overall leak of the deformed structure. The leak rate of an element

is determined by multiplying the leak rate found as given in Equation (4.22) by the elemental area and dividing by a reference area A_{ref}. The value of this reference area will be determined in Chapter 5.

4.5 UMAT procedure

This section describes the sequence of steps to be taken to determine the stress situation and the state variable values in the superplastic alloy ALNOVI-1 for a given strain increment, during superplastic forming. This is an implicit algorithm. The material shows a high strain rate sensitivity, so the time increment has to be taken into account within the sequence of steps. A full constitutive model of ALNOVI-1 should strictly speaking also contain a temperature dependency, but since this is not considered a variable in the forming process, the temperature will not be included. The model is valid for a temperature of 520 °C, i.e. the optimal temperature for superplastic forming of ALNOVI-1. The applied backpressure during forming is an input state variable. The output state variables to be stored are:

- the elastic strain vector $\boldsymbol{\varepsilon}^{\mathrm{e}}$ (3 scalar values), as resulting from Equation (2.28), to be calculated after the stress update procedure has been finished;
- the plastic strain vector $\boldsymbol{\varepsilon}^{\mathrm{p}}$ (3 scalar values), which is the difference between the total strain increment and the elastic strain increment;
- the equivalent plastic strain $\bar{\varepsilon}^{\mathrm{p}}$, this is the equivalent plastic strain from the previous increment plus the value of the plastic multiplier $\Delta\lambda$ as resulting from the stress update procedure in the current increment;
- the equivalent plastic strain rate $\dot{\bar{\varepsilon}}^{\mathrm{p}}$, which is equal to $\Delta\lambda/\Delta t$;
- the void volume fraction ξ, calculated from the transition strain $\varepsilon_{\mathrm{tr}}$, the slopes c_1 and c_2 and using Equation (4.20);
- the flow stress σ_{f}, as a result of Equations (4.2), (4.5) and (2.10).

Below, the steps taken within the user-defined material model description are described, including the part representing the stress return mapping algorithm.

1. Read all results from the previous increment, these are the stress $\boldsymbol{\sigma}_0$ and the output state variables.
2. Read the strain increment $\Delta\boldsymbol{\varepsilon}$, the time increment Δt and the input state variable p_{h}, which is the backpressure.

3. Determine the trial stress state according to

$$\boldsymbol{\sigma}^{\mathrm{tr}} = \boldsymbol{\sigma}_0 + \mathbf{C}\Delta\boldsymbol{\varepsilon} \tag{4.23}$$

where $\boldsymbol{\sigma}_0$ is the stress vector at the start of the new strain increment $\Delta\boldsymbol{\varepsilon}$ and $\boldsymbol{\sigma}^{\mathrm{tr}}$ at the end of this increment under the assumption that the whole strain increment is elastic.

4. Since the Hosford yield criterion is defined in the principal stress directions, determine the principal values of the trial stress vector as

$$\sigma_i = \frac{\sigma_{xx}^{\mathrm{tr}} + \sigma_{yy}^{\mathrm{tr}}}{2} + -\sqrt{\left[\frac{1}{2}(\sigma_{xx}^{\mathrm{tr}} - \sigma_{yy}^{\mathrm{tr}})\right]^2 + (\sigma_{xy}^{\mathrm{tr}})^2} \qquad i = 1, 2 \tag{4.24}$$

5. Calculate the equivalent Hosford stress using these principal values, according to

$$\phi = \frac{1}{1+R}(\sigma_1^n + \sigma_2^n) + \frac{R}{1+R}(\sigma_1 - \sigma_2)^n - \sigma_{\mathrm{f}}^n \tag{4.25}$$

6. Determine the flow stress by calculating the initial flow stress according to Equation (4.2), the hardening stress according to Equation (4.5) and the softening multiplication factor, see Equation (2.10). For these calculations, the equivalent plastic strain and strain rate are necessary, also the void volume fraction. Before the first iteration ($k = 0$), the equivalent plastic strain is the value as entered at the start of the time step, and the equivalent plastic strain rate is zero (since the strain increment is assumed to be completely elastic in the first iteration).

7. If the equivalent trial stress from Step 5 is larger than the flow stress as calculated in Step 6 (i.e. $\phi > 0$), then the material will show plastic deformation. If not, the material behaves purely elastically and the actual stress is equal to the trial stress. In that case, the plastic strain vector, the equivalent plastic strain and the void volume fraction do not change in this increment. In the case of purely elastic behavior, the algorithm ends here. If $\phi > 0$, proceed to Step 8.

8. Start the iteration procedure by initializing the value for the plastic multiplier (generally zero) and the value of the yield function, ϕ_0. Also, initialize the iteration counter, $k = 1$.

9. Calculate the flow direction $(\partial\phi/\partial\sigma)^{(k)}$ in the solution point, which is the trial stress point in the first iteration. Since the Hosford yield criterion is defined in the principal stress space, the flow direction can be calculated by making use of stress invariants $I_1^{(k)}$ and $I_2^{(k)}$

$$I_1^{(k)} = \sigma_1^{(k)} + \sigma_2^{(k)} \tag{4.26}$$

$$I_2^{(k)} = \sigma_1^{(k)} \sigma_2^{(k)} \tag{4.27}$$

Then (omitting the superscript k)

$$\frac{\partial \phi}{\partial \sigma} = \frac{\partial \phi}{\partial \sigma_1}\Big(\frac{\partial \sigma_1}{\partial I_1} \cdot \frac{\partial I_1}{\partial \sigma} + \frac{\partial \sigma_1}{\partial I_2} \cdot \frac{\partial I_2}{\partial \sigma}\Big) + \frac{\partial \phi}{\partial \sigma_2}\Big(\frac{\partial \sigma_2}{\partial I_1} \cdot \frac{\partial I_1}{\partial \sigma} + \frac{\partial \sigma_2}{\partial I_2} \cdot \frac{\partial I_2}{\partial \sigma}\Big) \tag{4.28}$$

10. Calculate the derivative of the flow direction, $\partial^2\phi/\partial\sigma^2$. The best method as a compromise between calculation speed and accuracy is to determine this second order matrix numerically instead of analytically.

11. Determine the flow stress with an equivalent plastic strain input equal to the plastic multiplier $\Delta\lambda^{(k)}$ and an equivalent plastic strain rate equal to $\Delta\lambda^{(k)}/\Delta t$. The use of the plastic multiplier as equivalent plastic strain is only permitted if the Hosford yield criterion is written such that $\partial\phi/\partial\sigma_\mathrm{f} = -1$, as in

$$\phi = \Big[\frac{1}{1+R}(\sigma_1^n + \sigma_2^n) + \frac{R}{1+R}(\sigma_1 - \sigma_2)^n\Big]^{1/n} - \sigma_\mathrm{f} \tag{4.29}$$

12. Two equations have to be solved simultaneously, the first one concerns the fact that the total strain increment in each step is an addition of an elastic strain increment and a plastic strain increment. Written in a residual format, this reads

$$\boldsymbol{r}_{\boldsymbol{\sigma}} = \Delta\boldsymbol{\varepsilon} - \Delta\boldsymbol{\varepsilon}^\mathrm{el} - \Delta\boldsymbol{\varepsilon}^\mathrm{pl} = \mathbf{0} \tag{4.30}$$

The second equation states that the value of the flow function in case of plastic deformation is equal to zero:

$$\boldsymbol{r}_{\boldsymbol{\phi}} = \phi = 0 \tag{4.31}$$

Rewriting the first equation gives

$$\boldsymbol{r}_{\boldsymbol{\sigma}} = \Delta\boldsymbol{\varepsilon} - \mathbf{C}^{-1}\Delta\boldsymbol{\sigma} - \Delta\lambda\frac{\partial\phi}{\partial\boldsymbol{\sigma}} = \mathbf{0} \tag{4.32}$$

To solve these equations in a Newton iteration scheme, they have to be linearized. For both equations, this results in case of the k-th iteration:

$$\boldsymbol{r}_{\boldsymbol{\sigma}}{}^{(k)} = \Big(\mathbf{C}^{-1} + \Delta\lambda\frac{\partial^2\phi}{\partial\boldsymbol{\sigma}^2}\Big)^{(k)}\mathrm{d}\boldsymbol{\sigma}^{(k)} + \mathrm{d}\lambda^{(k)}\Big(\frac{\partial\phi}{\partial\boldsymbol{\sigma}}\Big)^{(k)} \tag{4.33}$$

$$\boldsymbol{r}_{\boldsymbol{\phi}}{}^{(k)} = \Big(\frac{\partial\phi}{\partial\boldsymbol{\sigma}}\Big)^{(k)}\mathrm{d}\boldsymbol{\sigma}^{(k)} - \Big(\frac{\partial\phi}{\partial\bar{\varepsilon}^\mathrm{p}}\Big)^{(k)}\mathrm{d}\lambda^{(k)} \tag{4.34}$$

Rewrite this set of equations as

$$\tilde{\mathbf{C}}^{-1} \cdot \Delta(\mathrm{sol}) = \mathbf{r} \tag{4.35}$$

in which

$$\tilde{\mathbf{C}}^{-1} = \begin{bmatrix} [\mathbf{C}^{-1} + \Delta\lambda \frac{\partial^2 \phi}{\partial \boldsymbol{\sigma}^2}] & \{\frac{\partial \phi}{\partial \boldsymbol{\sigma}}\} \\ \{\frac{\partial \phi}{\partial \boldsymbol{\sigma}}\}^T & -\frac{\partial \phi}{\partial \bar{\varepsilon}^{\mathrm{p}}} \end{bmatrix}^{(k)} \tag{4.36}$$

$$\Delta(\mathrm{sol}) = \left\{ \{\Delta\boldsymbol{\sigma}\}^{(k+1)} \quad \Delta\lambda^{(k+1)} \right\}^T \tag{4.37}$$

$$\mathbf{r} = \left\{ \{\Delta\boldsymbol{\varepsilon} - \mathbf{C}^{-1} \cdot \boldsymbol{\sigma} - \Delta\lambda \frac{\partial \phi}{\partial \boldsymbol{\sigma}}\}^{(k)} \quad \phi^{(k)} \right\}^{\mathrm{T}} \tag{4.38}$$

Iterate until ϕ has reached a value which is smaller than a predefined tolerance value. The final solution for $\Delta(\mathrm{sol})$ has then been found.

13. Update the stress vector, the state variables and the iteration counter. The subincremental procedure is invoked if $\Delta(\mathrm{sol})$ is multiplied by a factor between 0 and 1 before the stress and equivalent plastic strain are updated. This factor can be applied during the whole iteration process, or only during the first iterations. Also, this factor does not have to be the same for all iterations. Go to step 9 if the solution has not been converged, or else go to step 14.

14. Store the stress and the state variables.

4.6 Summary and conclusions

This chapter presented the necessity of developing a user-defined material model in favor of the standard material models which are incorporated in ABAQUS. The Drucker-Prager model and Gurson's model have too many limitations to be useful as a constitutive model base for superplasticity. The standard Classical Metal Plasticity model with strain-rate dependency seemed the best option. However, at higher values for the equivalent plastic strain, the results were not accurate enough in case of simulation of the bulge experiment. Therefore a user-defined material model had to be developed.

This user-defined material model consists of 12 material parameters to describe the uniaxial behavior of ALNOVI-1. These parameters are used to define the initial flow stress, a hardening stress and a softening factor between 0 and 1 to account for the effect of the void volume fraction. Three extra parameters are necessary to account for the effect of the application of a backpressure during the deformation process. It is important that these three parameters are used in the case that the backpressure does not change during the deformation process, which is generally the case in superplastic forming processes.

The Hosford yield criterion has been applied with $n = 8$, this criterion is defined in the principal stress directions only. To account for this situation, the flow direction can be determined by using the stress invariants. This avoids the need to rotate the stress vector about an angle which has to be determined in the iteration

process. The first derivative of the flow function can be derived analytically, the second derivative is determined numerically in the user-defined material model.

The void volume fraction was determined as dependent on the equivalent plastic strain in a uniaxial stress situation. Two extra parameters were necessary to determine the void volume fraction in the case of a stress situation outside the uniaxial case.

The leak rate was found to be dependent on the void volume fraction and the resulting sheet thickness. This is what can be expected if the gas flows through the sheet instead of by a diffusion process. A linear relationship was found which is accurate enough between the logarithm of the leak rate, the void volume fraction and the sheet thickness.

In the next chapter, verification simulations will be carried out to verify the accuracy of the material model. All experiment types will be verified: uniaxial experiments, free bulge experiments and die bulge experiments. The last category, which was not mentioned in this chapter, is used to obtain a more detailed view of the friction coefficient between ALNOVI-1 and the die material.

5. Verification of the material model

The material model as established in the previous chapter will be verified by simulating the experiments. Simulations of the tensile tests have to show the ability of the material model to mimic the experimental force-displacement curves in the case of a uniaxial stress state. Also the void volume fractions, which were measured in the strain/vvf tensile tests, will be compared with simulations. In case of too high deviations, the values for the parameters should be adjusted, i.e. minimizing the difference between the corresponding load-displacement curves. Simulation of the tensile experiments is the subject of Section 5.1.

Simulations of the free and die bulge experiments are necessary to verify the biaxial behavior of the material model. Not only the prediction of the deformation state is important, but also the predicted leak value must be accurate enough. Section 5.2 discusses the simulation results of the free bulge experiments, whereas Section 5.3 is dedicated to the die bulge experiments. The parameters in the material model should be adjusted slightly if the simulation results do not match the experimental results accurately enough. These adjustments should then only cover the parameters which do not (or hardly) influence the uniaxial material behavior. Also the parameters which deal with the application of a backpressure are checked with the biaxial simulations.

5.1 Tensile test simulations

This section describes the results of the finite element simulations concerning the tensile experiments. Firstly, the simulated load-displacement curves are compared with the corresponding curves as found in the destructive tensile tests. The results may show that the material parameters describing the uniaxial behavior have to be adjusted. Secondly, the plastic strain rate is checked in the simulations, verifying the assumption that this value is constant throughout one test. Thirdly, the void volume fractions are calculated and compared with the experimentally found void volume fractions, as resulted from the strain/vvf tensile tests.

5.1.1 Tensile test FE model

With the material parameter values as established in the previous chapter, the tensile experiments have been simulated. In the finite element simulations, the five different cross-head velocities have been applied, i.e. 1, 2, 3, 5 and 10 mm/min.

The finite element mesh of the model is shown in Figure 5.1. The model describes a quarter of the tensile specimen, since the specimen is double symmetric. The mesh consists of mainly four-noded quadrilateral shell elements (S4R) and a few triangular shell elements (S3). The right-hand side of the hole will be moved to the right, see the bold line in Figure 5.1.

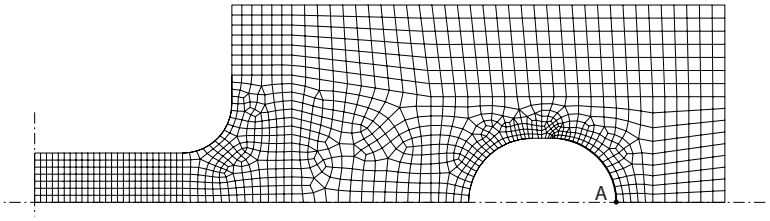

Figure 5.1: Finite element model of the tensile specimen.

The reaction force on the vertical symmetry edge will be monitored as a function of time. It is important that a displacement in the direction of the shell normal will not be restrained, since it was observed in the experiments that an out-of-plane displacement is present. This was especially seen on the far ends of the specimen, caused by the fact that aligning the specimen with the cross-head is only theoretically possible. In node A (see Figure 5.1), a small displacement (2 μm) in normal direction is prescribed to trigger this out-of-plane behavior.

Figure 5.2 shows the deformed mesh after loading with a tensile velocity of 1 mm/min. The maximum displacement is 20 mm. Here it is clearly visible that an out-of-plane displacement occurs, just as in the experiments (see inset in the figure).

5.1.2 Simulated load-displacement curves

The numerically obtained load-displacement curves at all five cross-head velocities are compared with the corresponding curves from the experiments. The result are plotted in Figure 5.3.

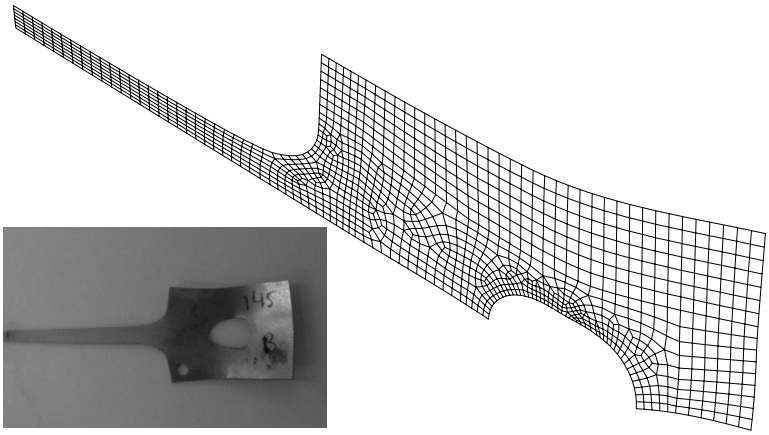

Figure 5.2: Deformed finite element mesh of the tensile specimen, at a loading velocity of 1 mm/min.

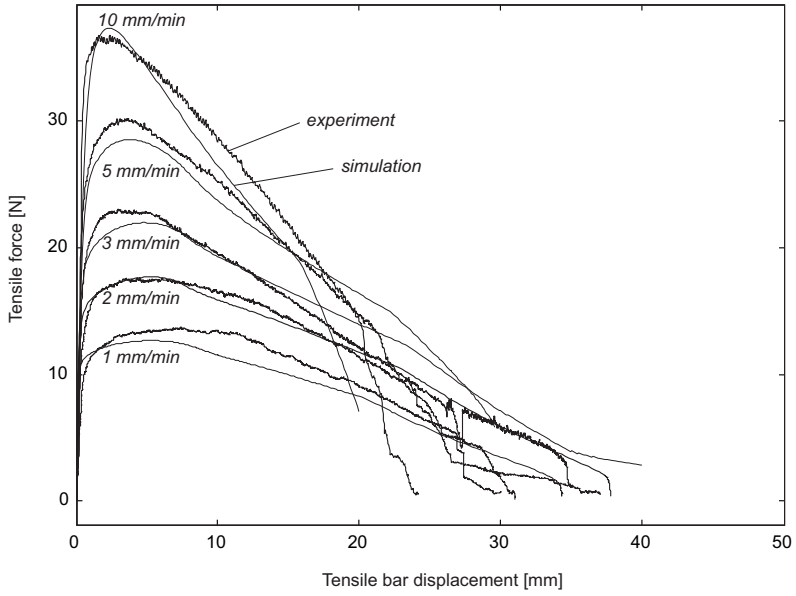

Figure 5.3: Load-displacement curves: simulations compared with experiments.

It can be seen that the load-displacement curve at a cross-head velocity of 2 mm/min shows very good correlation. However, at 1, 3 and 5 mm/min, the simulated force is somewhat too low compared with the experimental values. Hence, an adjustment of the parameters which are responsible for the uniaxial mechanical behavior is necessary to minimize the difference between the experimental and simulated values. In fact, this can be considered an optimization problem where the material parameters are the design variables. The goal function to be minimized is an addition of squared values of force deviations between simulation and experiment, at a predefined set of displacement values. The best results were obtained by increasing the slope at the lower and higher end of the universal superplastic curve, see Figure 5.4.

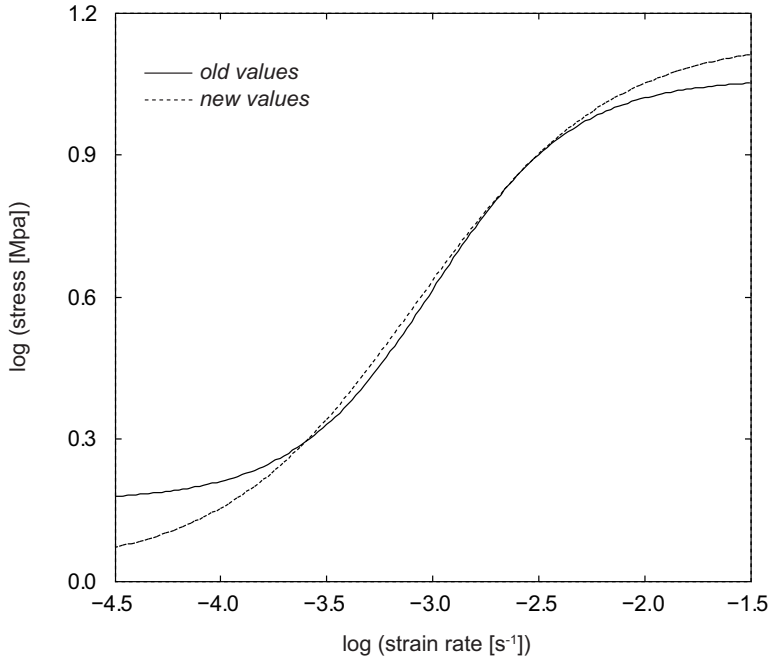

Figure 5.4: Universal superplastic curve: old vs. new parameter values.

Table 5.1 shows the value of the parameters of the universal superplastic curve, as given in the previous chapter, versus the optimized values. It can be seen that these adjustments have their main effect on the low and high strain rate. The midrange, which is around the optimal superplastic strain rate, is much less affected.

With these new values, the optimal superplastic strain rate, according to Appendix A, becomes $8.3{\cdot}10^{-4}$ s^{-1} (was $1.0{\cdot}10^{-3}$ s^{-1}) and the strain rate sensitivity at this strain rate is then 0.619 (was 0.676). All the other parameter values responsible for the uniaxial behavior seemed to be already accurate enough to obtain a good fit for the load-displacement curves.

Table 5.1: Old and new value of the material parameters of the ALNOVI-1 material model.

Parameter	Value (Ch4)	Optimized value
a	1.1221	0.89208
b	1.2442E-4	9.8721E-4
c	-3.0354	-2.2093
d	0.16963	2.4235E-2

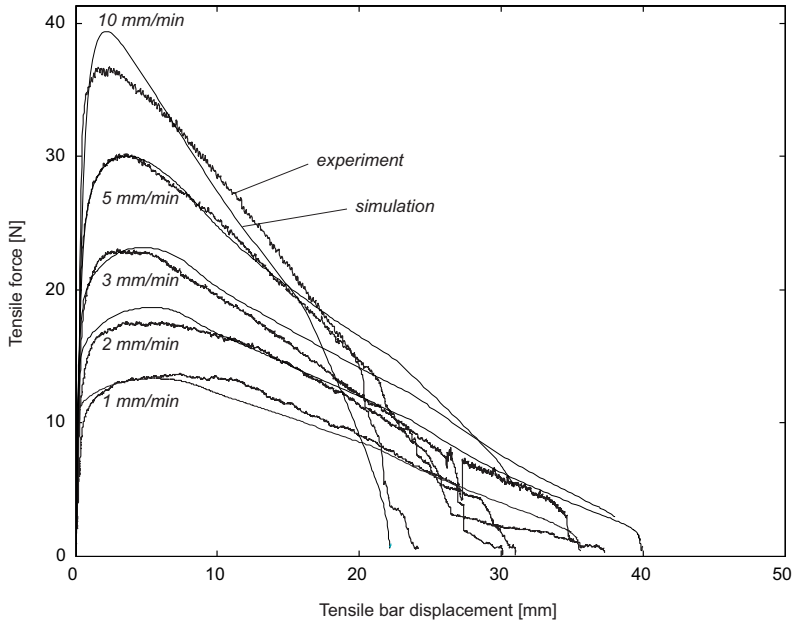

Figure 5.5: Load-displacement curves: simulations compared with experiments, with the optimized parameter values.

With these optimized values, the tensile experiments have been simulated a second time, resulting in load-displacement curves which lie on average closer to the experimental curves. Figure 5.5 shows that at 1, 3 and 5 mm/min, the simulated curves are closer to the experimental curves, at a cost of less accuracy at 2 and 10 mm/min. Since a velocity of 10 mm/min results in a strain rate which is not desired in superplastic forming processes, this curve is considered less important than the curve at the other velocities.

5.1.3 Simulated strain rates

The void volume fraction is one of the output state variables built into the material model, and is used to calculate the strain softening. From Figure 3.8 it was concluded that the void volume fraction can be considered as dependent only on the equivalent plastic strain, and not on the strain rate. The results as presented in Figure 3.6 assumed constant values for the strain rate. From these strain rate values and the total loading time, a value for the equivalent plastic strain was calculated. The simulations of the tensile experiments have to confirm the assumption of constant strain rate during the loading process. Results of these simulations are shown in Figure 5.6.

As can be seen from the plots, the plastic strain rates can be considered constant to a great extent, but the loading rate of 10 mm/min is an exception. The dotted lines in the figure show the strain rates as used in Chapter 3, which are very good in accordance with the simulation results. Only in the case of a loading rate of 10 mm/min, the plastic strain rates cannot be considered constant.

5.1.4 Simulated void volume fractions

As was concluded in the previous subsection, the strain rates can be considered constant in the tensile experiments, apart from the tests at the highest loading rate of 10 mm/min. The plastic strain is increasing monotonically with increasing cross-head displacement. The void volume fractions as a function of the cross-head displacement for both simulation and experiment is given in Figure 5.7. The simulation results approximate the experimental results with reasonable accuracy.

In this figure, a point is present where the slopes of the curves instantaneously change; this is a result of the abrupt change which is coded in the material model. At a strain below the transition strain $\varepsilon_{\mathrm{tr}}$, the slope is determined by the parameter c_1. If the equivalent plastic strain exceeds this transition strain, the slope changes from c_1 to c_2. Figure 5.7 shows that the slopes resulting from the simulations are correct, the transition strain seems somewhat too low. However, since the difference is not too high, the free bulge simulations will be performed with the existing value for the transition strain. If the same kind of error is found in these simulations, the transition strain will be adjusted.

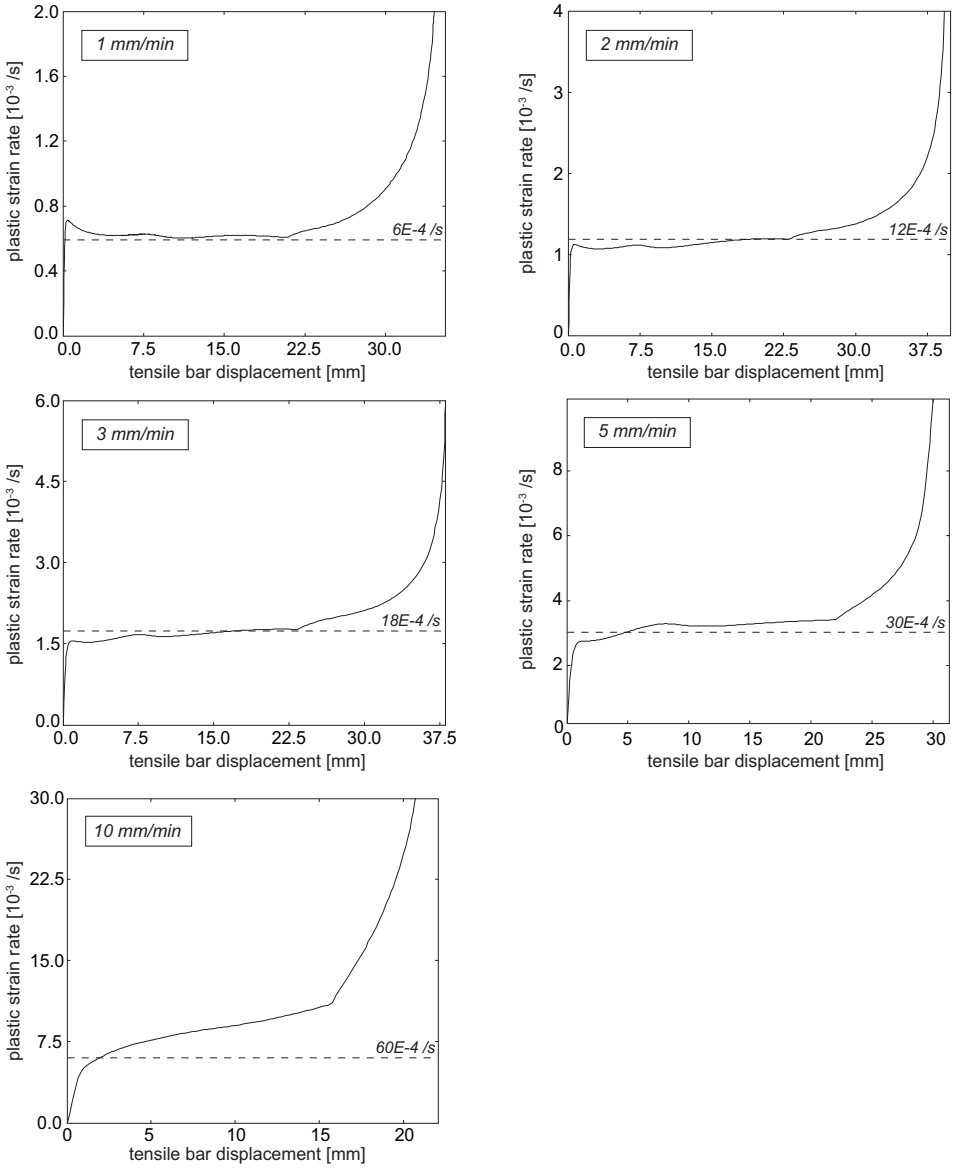

Figure 5.6: Simulated plastic strain rates in the tensile tests.

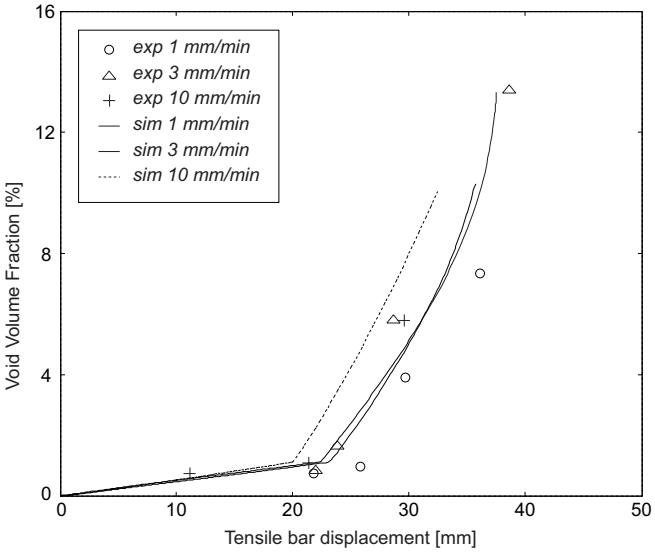

Figure 5.7: Void volume fractions as a function of the cross-head displacement, experiment versus simulation.

5.2 Free bulge simulations

The free bulge experiments will be simulated by using the extra biaxial data as established in Section 4.3.2. In the verification simulations, the parameters which determine the uniaxial behavior will be used as established in the previous section. If a backpressure during the deformation process is not applied, this covers especially the parameters which relate the void volume fraction to the biaxial stress situation, x_1 and x_2. The influence of the applied backpressure is determined by the three parameters c_3, c_4 and c_5. These factors determine the way the slopes c_1 and c_2 change under the application of a hydrostatic pressure during the forming process. Also the transition strain $\varepsilon_{\mathrm{tr}}$ can be influenced by this backpressure.

This section describes the verification simulations in terms of bulge height, top wall thickness, void volume fraction and leak rate. Firstly, in Section 5.2.1, the FE model used for the free bulge verification simulation is discussed. Secondly, in Section 5.2.2, the bulge simulations without the application of a backpressure are presented. A backpressure application does not modify the parameters determined here, so these verification simulations can be dealt with separately. This is done in Section 5.2.3.

5.2.1 Free bulge FE model

Since the experiments were performed on circular sheets, it seems straightforward to use an axisymmetric FE model of the experimental setup to simulate the tests. However, the user-defined material model has been written for use in plane stress situations, since this is necessary for calculations on the RF Foil. So, this model can only be used for models using elements which are described by plane stress behavior.

Since the superplastic forming process mainly involves stretching behavior rather than bending behavior, membrane elements can be used in the simulations [16]. The main advantage of the use of membrane elements instead of shell elements is that the simulation time is considerably less, since bending effects are omitted in membrane elements. To make sure that simplification is justified, several simulations were performed with both element types used. The conclusion was that both element types give nearly the same results, which justifies the use of membrane elements. The finite element model of the free bulge experiments is shown in Figure 5.8.

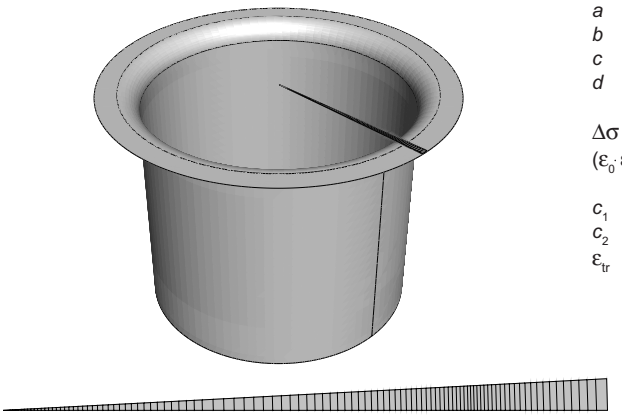

a	0.89208	n_1	5.24
b	9.8721E-4	n_2	0.946
c	-2.2093	n_3	1.272
d	2.4235E-2		
		x_1	5.61E-3
$\Delta\sigma$	3.21 (MPa)	x_2	-2.33E-2
$(\varepsilon_0 \cdot \dot{\varepsilon})$	1.36E-4		
		R	0.825
c_1	0.015	n	8
c_2	0.141		
ε_{tr}	0.74		

Figure 5.8: FE model and parameter values used for the free bulge simulations, below a detailed representation of the mesh of the sheet.

The model of the sheet is a small angled pie, meshed with four-noded membrane elements (M3D4R), one triangular element in the model (M3D3) is applied at the tip of the angled pie. Test simulations had been performed to compare this FE model with a model representing a quarter of the sheet, and both situations gave nearly the same results. Therefore this small angled pie is used, since it saves a considerable amount of simulation time.

5.2.2 Free bulge simulations without backpressure

Four parameters in the material model are related to the plane stress biaxial behavior, on top of the uniaxial behavior. One is the Hosford exponent n, which was assumed to have the value 8. The second parameter, which partly determines the shape of the yield locus, is the Lankford strain ratio R. The third and fourth parameters describe the void volume fraction evolution in the case of a biaxial stress state, x_1 and x_2.

The four parameters mentioned here are adjusted in such a way that the bulge height, top thickness and void volume fraction show the best comparison between simulation and experiment. A fifth parameter, the reference area, is adjusted to give the correct leak rate values. The reference area A_{ref}, which was introduced in Section 4.4.2, is a hypothetical area responsible for the major part of the gas leak through the formed bulges. Table 5.2 gives the values which result in the best comparison between simulation and experiment.

Table 5.2: Parameter values influencing the biaxial flow behavior.

	n	R	x_1	x_2	A_{ref}
old values	8	0.825	0.00561	-0.0233	N/A
new values	8	0.7081	0.01674	-0.03042	$1.35{\cdot}10^{-4}$

Figure 5.9 shows the bulge height as a function of time for three target strain rates. As can be seen in the graphs, the simulated bulge height corresponds very well with the experimental values, only the graph at a target strain rate of $12{\cdot}10^{-4}$ s^{-1} shows a somewhat higher deviation. This is also the case for the simulated top wall thicknesses, as can be seen in Figure 5.10. A simulation stops if the multiplication factor, which is responsible for the softening in the uniaxial material description, becomes zero. This is at a value for the void volume fraction of about 16 %. In that case, the flow stress of the material has dropped to zero.

The void volume fractions can be presented as function of deformation time, but it is a better comparison if the void volume fraction is made dependent on the bulge height. The results of the simulation versus the experimentally found values are presented in Table 5.3. The value for the void volume fraction at a strain rate of $18{\cdot}10^{-4}$ s^{-1} is extrapolated, since a bulge height of 40.52 mm was not reached in the simulations (maximum bulge height was 38.82 mm). It is clear from this table that the simulated void volume fractions resemble the measured values quite well. As was already concluded from Figure 3.17, the results of the leak rate measurements show a high variance. This makes it difficult to predict the correct leak value by simulations. From Table 3.6, two values are extracted which are compared with the simulations. These are the values of the maximum bulge

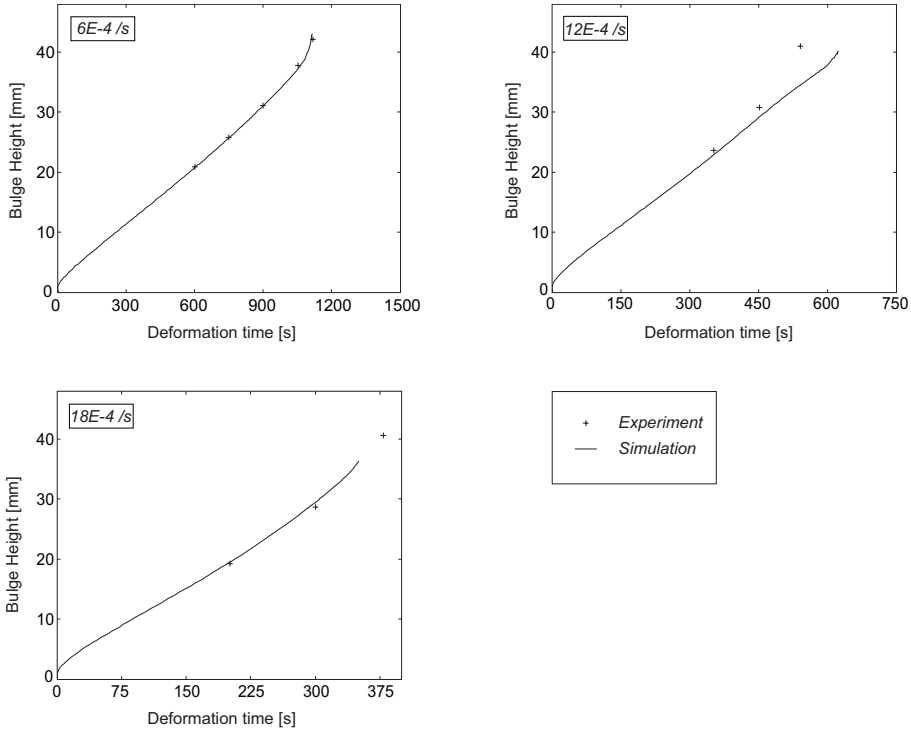

Figure 5.9: Simulated bulge heights, compared with the experimental values for three different values of the target strain rate.

Table 5.3: Simulated vs. measured void volume fractions ξ in the free bulge experiments (no backpressure) at some values for the bulge height u. The value marked with $^{*)}$ is an extrapolated value.

$\dot{\bar{\varepsilon}}_{\text{target}}$	u	ξ_{exp}	ξ_{sim}
6e-4	37.82	2.5	3.12
	42.14	8.9	7.67
12e-4	31.06	1.4	1.60
	41.16	7.2	7.32
18e-4	40.52	12.6	12.89$^{*)}$

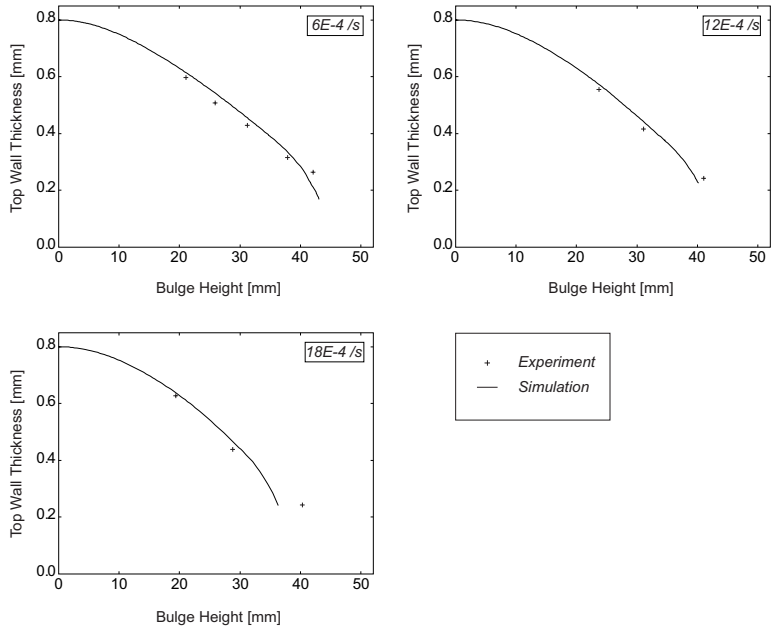

Figure 5.10: Simulated top wall thicknesses, compared with the experimental values for three different values of the target strain rate.

heights reached at a predefined level of the leak rate, without the application of a backpressure. For a leak rate of 10^{-8} mbar l/s and an initial sheet thickness of 0.8 mm, this was 31.31 mm; for a leak rate of 10^{0} mbar l/s, this bulge height was 37.97 mm.

Table 5.4: Simulated bulge heights (in mm) where the leak rate reaches a value of 10^{-8} mbar l/s and 10^{0} mbar l/s.

$\dot{\bar{\varepsilon}}_{\text{target}}$	$\log L = -8$	$\log L = 0$
6e-4	32.68	38.45
12e-4	31.59	37.25
18e-4	31.12	35.13
experiment	31.31	37.97

Table 5.4 shows the corresponding values of the bulge height for the three

different target strain rates, compared with the two bulge height values from the experiments. The tables show that the results are accurate enough to perform reliable simulations with respect to the leak rate, without the application of a backpressure.

5.2.3 Free bulge simulations: 30 bar backpressure

The material model contains three parameters which describe the material behavior in case a hydrostatic pressure during plastic deformation is applied: c_3, c_4 and c_5. These parameters determine the change of the parameters c_1, c_2 and $\varepsilon_{\mathrm{tr}}$ as a function of the backpressure value. Initially, these parameters are set to the values $c_3 = 0.02$, $c_4 = 0.06$ and $c_5 = 0.02$. With these parameter values set, the bulge heights from the simulations are compared with the experimentally found bulge heights. The results are visible in Figure 5.11; the simulated curves follow the experimental values well until about a height of 40 mm.

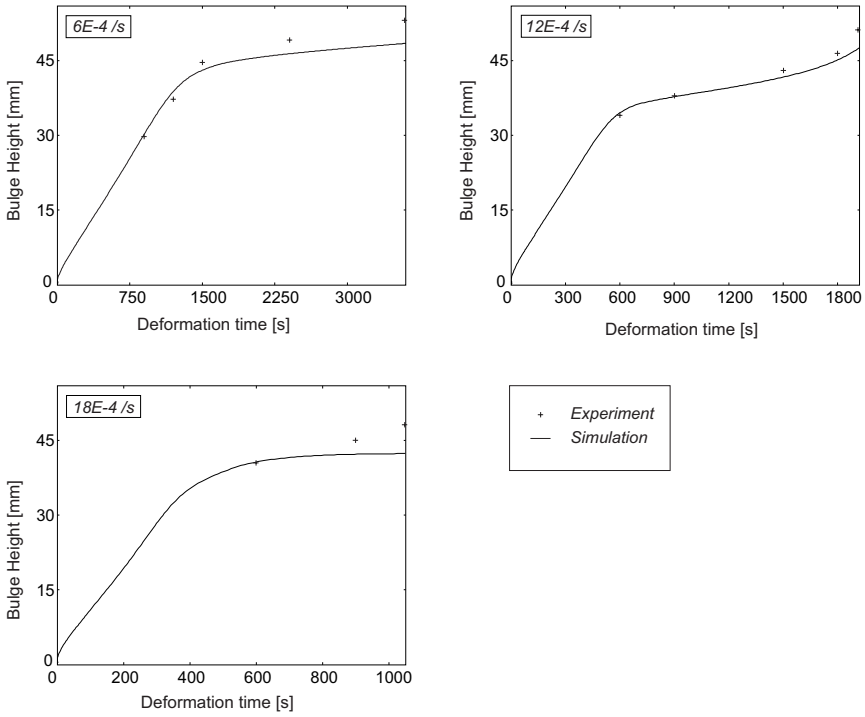

Figure 5.11: Simulated bulge heights with the application of a backpressure of 30 bar, compared with the experimental values for three different values of the target strain rate.

With increasing deformation time, the predicted bulge height underestimates the experimental values, indicating that the values for c_3, c_4 and c_5 must be changed (slightly) to overcome this difference.

Besides the bulge height, the void volume fraction is also important to look at, since this mainly determines the value of the leak rate. Table 5.5 shows the results of the simulated and the experimentally found void volume fractions.

Table 5.5: Simulated vs. measured void volume fractions ξ in the free bulge experiments (30 bar backpressure) as function of the bulge height u. The value marked with $^{*)}$ is an extrapolated value.

$\dot{\bar{\varepsilon}}_{\text{target}}$	u	ξ_{exp}	ξ_{sim}
6e-4	43.98	0.94	1.92
	49.15	2.4	2.83
12e-4	38.08	0.87	1.49
	51.15	3.2	$3.63^{*)}$
18e-4	48.16	1.7	-

From this table it is clear that the simulated values do not correspond well with the measured void volume fractions. Also the ratios between the void volume fractions within the results of one target strain rate value are not the same between experiment and simulation. For instance, at a strain rate of $6{\cdot}10^{-4}$ s^{-1}, a ratio of $2.4/0.94 = 2.55$ is calculated, whereas this ratio from simulations is $2.83/1.92 = 1.47$. The simulated void volume fraction at a target strain rate of $18 \cdot 10^{-4}$ s^{-1} is missing in the table, since a bulge height of 48.16 mm is not reached and is too high to approximate the void volume fraction by extrapolation. The maximum bulge height reached in the simulations at this target strain rate is 42.3 mm. Adjusting the values for c_3, c_4 and c_5 shows that it is possible to obtain a better fit for the bulge height in time. An optimization procedure has to correct the values for c_3, c_4 and c_5 to obtain the best fit. This procedure is based on the Response Surface Methodology, which is explained more elaborately in Chapter 6. Following a Screening Design of Experiments, a space-filling Design of Experiments has been developed, based on a Latin hypercube method [58]. This procedure did not result in satisfactory values for these parameters. Void volume fractions deviated from the experimental results by more than 20%.

If the aforementioned ratio of the void volume fractions is used as a basis for the optimization goal, then adequate results were obtained. Following the same optimization method (RSM), the best fitting values resulted in $c_3 = 0.0148$, $c_4 = 0.0098$ and $c_5 = 0.0184$. In this case, the ratio is correct, but the absolute values

for the void volume fractions are not. An extra parameter, which is dependent on the backpressure, must be incorporated. This parameter, x_3, is used in a multiplier α on the initially calculated void volume fraction as

$$\alpha = 1 + x_3(p_{\mathrm{h}} - p_{\mathrm{atm}}) \tag{5.1}$$

where p_{h} is the value of the applied backpressure (in bars) and p_{atm} is the atmospheric pressure (1 bar). If no backpressure is applied during the deformation process, α is equal to 1. The best fit for x_3 is found to be 0.0476.

Table 5.6 shows the results of the void volume fractions from the simulations, compared with the measured void volume fractions. The simulated bulge height also conforms better to the experimentally found bulge heights, as is depicted in Figure 5.12.

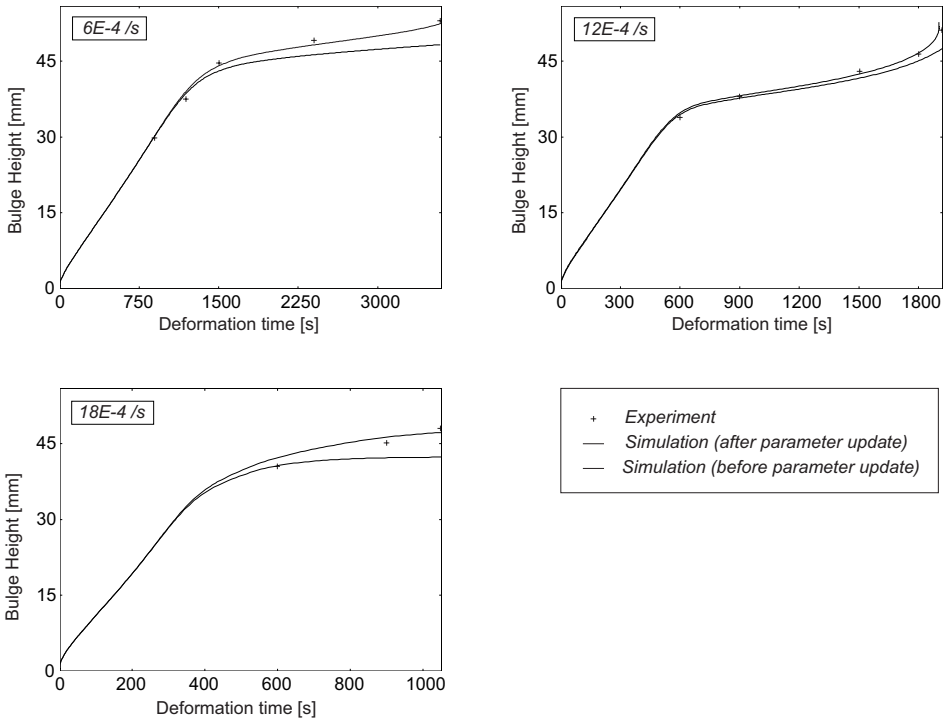

Figure 5.12: Simulated bulge heights with the application of a backpressure of 30 bar, after correction of the necessary parameters. Also the results before the parameter update are shown.

Table 5.6: Simulated vs. measured void volume fractions in the free bulge experiments (30 bar backpressure), after correction of the necessary parameters.

$\dot{\bar{\varepsilon}}_{\text{target}}$	u	ξ_{exp}	ξ_{sim}
6e-4	43.98	0.94	0.93
	49.15	2.4	2.21
12e-4	38.08	0.87	0.72
	51.15	3.2	3.50
18e-4	48.16	1.7	2.41

5.2.4 Simulated leak rates

As described in Section 4.4.2, the leak rate is dependent on the void volume fraction and the current wall thickness. A necessary parameter to achieve a prediction for the leak rate is the reference area, which must be determined to have as accurate a prediction as possible. The leak rate of the deformed sheet is one scalar value for the whole model. Therefore it is chosen to determine the leak rate of a formed sheet outside the FE simulation. The results, which are written to a database file, can be used to calculate the leak rate as a function of the element thicknesses, the void volume fractions and the elemental areas. The expression for the leak rate was presented in Section 4.4.2, see Equation (4.22). The result of leak rate calculation according to this equation has to be multiplied by the element area and divided by the reference area, in order to find the leak rate for the whole element. The summation of all element leak rates is the leak rate of the deformed sheet.

The leak rates resulting from the simulations are presented in Table 5.7 and Table 5.8. For four values of the backpressure the bulge height is determined where the leak rate equals 10^{-8} and 10^{0} mbar l/s. The reference area as given in Section 5.2.2 is used in these simulations. The simulations correspond very well with the values for the leak reached in the free bulge experiments. It can be concluded that the higher the target strain rate, the lower the bulge height which can be reached at a predefined value of the leak rate. The difference in bulge height between $6 \cdot 10^{-4}$ and $12 \cdot 10^{-4}$ s^{-1} is not so large, but at a target strain rate of $18 \cdot 10^{-4}$ s^{-1}, the bulge heights are significantly lower at the same leak rate value. This is what was to be expected, since earlier in this chapter it was concluded that the optimal strain rate lies between the first two values, being $8.3 \cdot 10^{-4}$ s^{-1}.

Table 5.7: Bulge height values at which a leak of 10^{-8} mbar l/s is reached, simulation versus experiment. Four backpressure values are used: 0, 14, 22 and 30 bar

$\dot{\bar{\varepsilon}}_{\text{target}}$ [s^{-1}]	BP00	BP14	BP22	BP30
$6 \cdot 10^{-4}$	32.68	37.76	42.18	45.32
$12 \cdot 10^{-4}$	31.59	36.88	41.57	44.98
$18 \cdot 10^{-4}$	31.12	35.86	38.88	41.23
experiment	31.31	34.47	39.23	44.82

Table 5.8: Bulge height values at which a leak of 10^{-1} mbar l/s is reached, simulation versus experiment. Four backpressure values are used: 0, 14, 22 and 30 bar

$\dot{\bar{\varepsilon}}_{\text{target}}$ [s^{-1}]	BP00	BP14	BP22	BP30
$6 \cdot 10^{-4}$	38.45	42.90	48.09	51.53
$12 \cdot 10^{-4}$	37.25	41.75	47.34	50.68
$18 \cdot 10^{-4}$	35.13	39.79	42.74	46.78
experiment	37.93	40.04	46.50	49.24

5.2.5 Bulge shapes

In Figure 4.3, it was seen that the forming of the bulge by using a built-in ABAQUS material model leads to instabilities during forming. When using the user-defined material model, these instabilities do not occur. Especially for the simulations where a backpressure has been applied, the bulge shape much more conforms to the shape as found in the experiments. Figure 5.13 shows the bulge shape when the user-defined material is used. This is mainly a result of the use of the Hosford

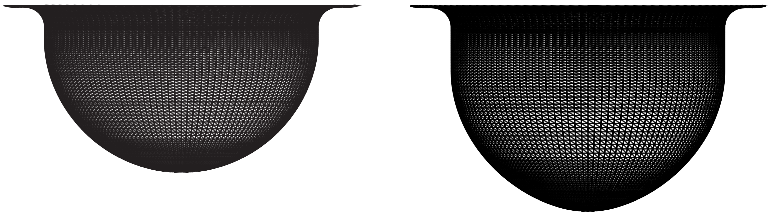

Figure 5.13: Bulge shapes in two stages of the free bulge simulations by applying the user-defined material model. For visualization reasons, the mesh of Figure 5.8 has been revolved.

yield criterion instead of the von Mises yield criterion. The areas on the side of the bulge, near the flange, are in a plane strain state. This region flows earlier when the Hosford yield criterion is applied, with an exponent higher than 2; in this case $n = 8$.

5.3 Die bulge simulations

Simulations of the die bulge experiments are carried out to find a value for the friction coefficient between the sheet and the die. In the experiments, two lubricant types were use: graphite and Molykote. Molykote clearly resulted in a lower friction coefficient, as was concluded in Section 3.4.3. The desired aim is to ensure that the resulting sheet thickness is evenly distributed. This situation is achieved better if Molykote is used as a lubricant, rather than graphite. In the case of graphite as a lubricant, the resulting sheet thickness in the middle of the specimens is considerably higher than the thickness in the cavities. Because of the lower friction coefficient caused by Molykote as a lubricant, only these experiments will be verified within the simulations. From these simulations, the ratio between the mid wall and side wall thickness is calculated and compared with the measured values from the experiments, refer to Tables 3.10 and 3.11. Simulations are carried out without and with the application of a backpressure.

The finite element mesh used for the free bulge simulations can also be used for the die bulge simulations, with the same element type and description. However, since the final shape of the bulges has a higher complexity than the shapes from the free bulge simulations, the elements are smaller. The cylindrical die which is used in the free bulge simulations will be replaced by the die as designed for the die bulge experiments. The die bulge FE model is shown in Figure 5.14.

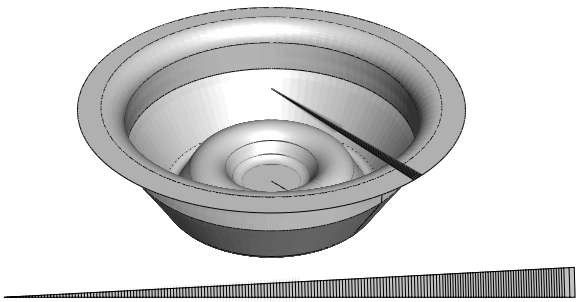

Figure 5.14: FE model used for the die bulge simulations, below a detailed representation of the mesh of the sheet.

5.3.1 Die bulge simulations without backpressure

Because the friction coefficient is not known beforehand, simulations will be carried out for different values of this coefficient. The chosen values at which the experiments are carried out, are also used in these simulations; this concerns a series of five coefficients: 0.04, 0.08, 0.12, 0.16 and 0.20. Each simulation covers a friction coefficient and one of the three target strain rates, resulting in 15 FE simulations. From the experiments, it was already concluded that the friction coefficient must be about 0.12.

The design of the die is such that the ratio of the mid wall and cavity wall thickness is a measure for the friction coefficient. The results of the FE simulations at the five aforementioned friction coefficients are presented in Figure 5.15. For each

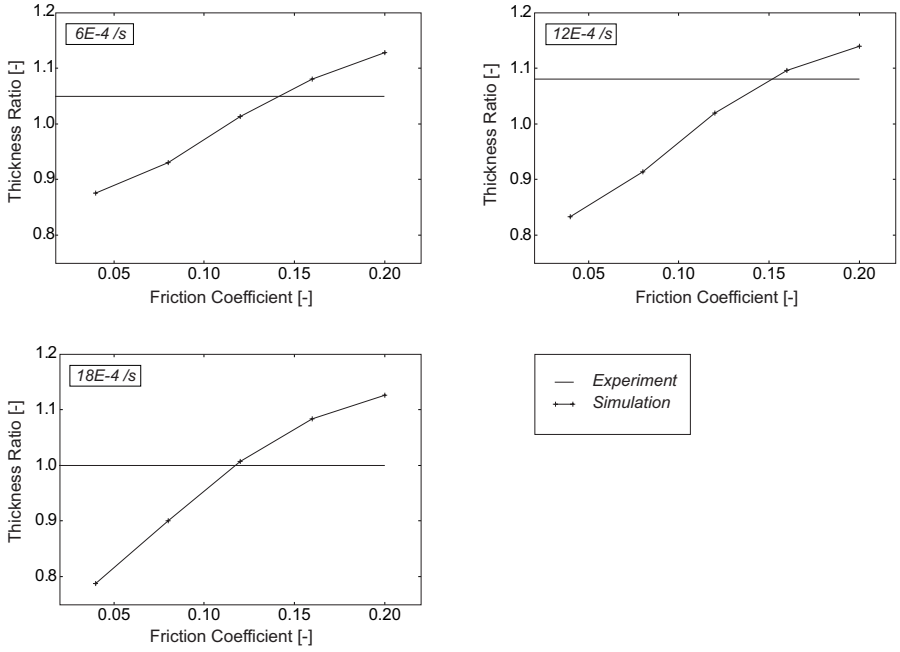

Figure 5.15: Thickness ratios of the die bulge test, for each of the three target strain rates; no backpressure.

value of the target strain rate, the friction coefficient is estimated by determining the intersection point between the simulated line and the value measured in the experiments. From the graphs, it follows that the friction coefficient for each of the target strain rates reads 0.14, 0.15 and 0.12, respectively. On average, the friction coefficient is 0.14.

5.3.2 Die bulge simulations with 30 bar backpressure

The same simulations have been done with the application of a backpressure of 30 bar, of which the results are shown in Figure 5.16. These graphs show a much more

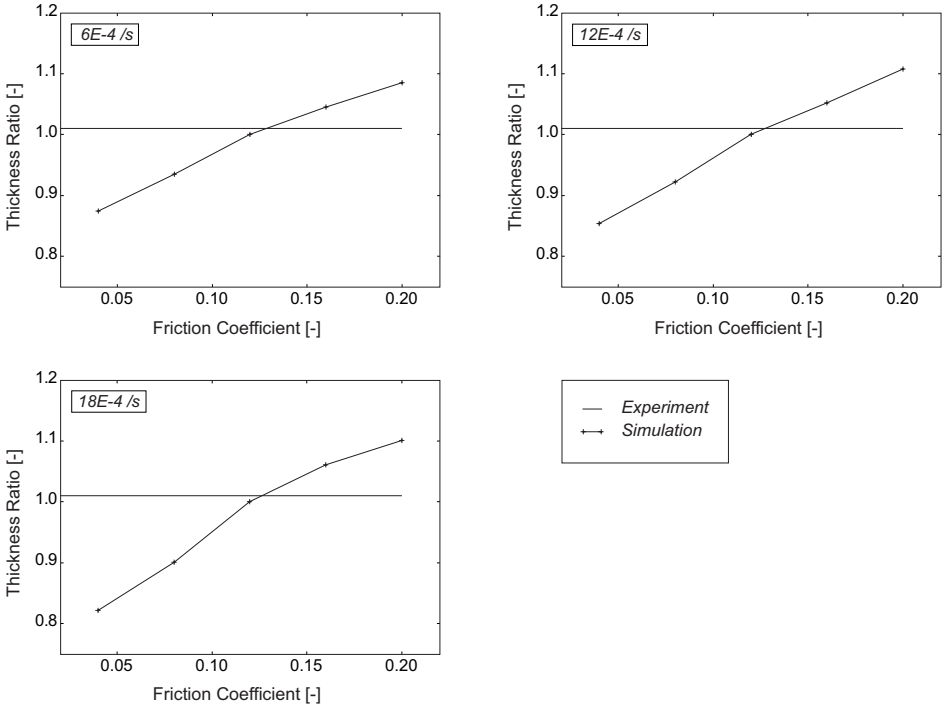

Figure 5.16: Thickness ratios of the die bulge test, for each of the three target strain rates; 30 bar backpressure.

consistent behavior in terms of the friction coefficient, than when no backpressure is applied. All three graphs show that the value for the friction coefficient is 0.13. Since in the remainder of this research all calculations will be carried out on the RF Foil by applying a backpressure of 30 bar during deformation, a friction coefficient of 0.13 will be used in all calculations.

5.3.3 Die bulge leak rate simulations

Two sets of simulations have been performed to validate the leak rate predictions, i.e. with and without the application of a backpressure. In the case of the simulations without the application of a backpressure, a value for the friction coefficient of 0.14 will be used. If a backpressure of 30 bar is applied, the friction coefficient

in the simulations will be set to 0.13. The simulation results are presented in Table 5.9, where they are compared with the experimentally found values for the maximum cavity height.

Table 5.9: Maximum cavity height (with no leak) at three different strain rates, simulation versus experiment. Values are in mm.

$\dot{\bar{\varepsilon}}_{\text{target}}$	$6{\cdot}10^{-4}$ s^{-1}	$12{\cdot}10^{-4}$ s^{-1}	$18{\cdot}10^{-4}$ s^{-1}
Exp: Max. height (No BP)	23.5	25.2	24.1
Sim: Max. height (No BP)	24.1	24.5	23.3
Exp: Max. height (30 bar BP)	24.4	26.9	25.3
Sim: Max. height (30 bar BP)	24.9	26.7	25.5

The numbers in the table give the maximum cavity height in case no leak is present. The simulation results approximate the experimental results with reasonable accuracy when no backpressure is applied. The simulation results with the application of a 30 bar backpressure show a somewhat higher accuracy. The difference between these two accuracies is not high enough to be significantly different. The reason for this is the fact that the leak rate measurements show a high variance.

5.4 Summary and conclusions

To describe the mechanical properties under uniaxial stress conditions, 12 parameters are necessary. These parameters can describe the uniaxial behavior in terms of initial flow stress, hardening stress and softening stress. The softening stress is dependent on the void volume fraction, which can also be predicted with the material model. Three extra parameters describe the uniaxial stress conditions in case a backpressure is applied. The plane stress conditions are described with two extra parameters, which account for the void growth in case of a non-uniaxial stress condition. The void volume fraction can be predicted under conditions without and with the application of a backpressure. All results obtained within the simulations are accurate enough to state that the material model can be used to perform superplastic forming simulations with ALNOVI-1. This is true for simulations with or without the use of a die, and also with or without the application of a backpressure during the deformation process.

Unfortunately, the material model needed an extra parameter to predict the void volume fraction when a backpressure is applied. It is a multiplier without any physical background inside the material model to adjust the void volume fraction

to the correct value, dependent on the backpressure. On the other hand, it is an additional parameter, used for determining the right void volume fraction. This adaptation works well and can be used to predict the leak rate of the simulation model.

One of the most important features of the developed material model is that the leak rate can be predicted. From both the free and the die bulge simulations, it is clear that the leak rate can be predicted in an acceptable way. Note, however, that the leak rate measurements from the experiments show relatively high deviations.

The best simulation results are obtained when a 30 bar backpressure is present, for all three target strain rates a friction coefficient of 0.13 is found. In the case of superplastic forming simulations this value seems realistic, see also Section 3.4.3.

An interesting thing to see is the following. The manufactured RF Foil had many problems with the leak tightness, and a leak was already present if the resulting sheet thickness was lower than 0.17 mm. From the die bulge simulations, it followed that the formed shapes which did not show a leak, showed a minimum wall thickness of about 0.12 mm. This is an indication that if the RF Foil is manufactured by means of superplastic forming, a thinner foil can be made which is leak-tight. The following chapter is dedicated to this subject: the optimization of the RF Foil with respect to the radiation length (which is mostly dependent on the sheet thickness), with the leak tightness as its most important constraint.

All parameter values as extracted from the verification simulations are summarized in Table 5.10. In Appendix C, an example is given of an ABAQUS input file to analyze the forming behavior in case of a die bulge simulation with an application of 30 bar backpressure.

Table 5.10: Parameter values used in the UMAT, leak rate calculated according to Equation (4.22).

a	0.89208	c_1	0.015	n_1	5.24	R	0.7081
b	9.8721E-4	c_2	0.141	n_2	0.946	n	8
c	-2.2093	c_3	0.0148	n_3	1.272	A_{ref}	1.35E-4
d	2.4235E-2	c_4	0.0098	x_1	1.674E-2	μ	0.13
$\Delta\sigma$	3.21	c_5	0.0184	x_2	-3.042E-2		
$(\varepsilon_0 \cdot \dot{\varepsilon}$	1.36E-4	ε_{tr}	0.74	x_3	0.0476		

6. Optimization of the RF Foil

In Chapter 1, the properties of the current RF Foil, to be used in the LHCb VeLo detector, are discussed. The current design is the product of a trial-and-error procedure, which resulted in an RF Foil that met the requirements. However, this is believed not to be an optimal design. If the percentual radiation length of the RF Foil could be made smaller, then the measurement error of the detectors placed in the RF Box (to recall: The RF Foil is the top sheet of the RF Box) would be smaller. This reduction in radiation length, which means in general a reduction in the resulting sheet thickness, is restricted to a set of requirements, also mentioned in Chapter 1.

In the optimization problem of the RF Foil, the percentual radiation length is chosen as the objective function. In simple terms, this is the probability that a particle trajectory is measured incorrectly. This objective function must be minimized by finding optimal settings of the design variables while satisfying a set of constraints. Section 6.1 gives a general overview and some solution algorithms used in optimization theory.

A program developed at the Twente University by M. Bonte, called OptForm, uses an optimization methodology that will be used in the RF Foil optimization procedure. One of the mathematical techniques that is used in the optimization algorithm is the Response Surface Methodology (RSM) [11, 58]. A description of the optimization strategy will be presented in Section 6.2.

In order to calculate the percentual radiation length (the objective function), a procedure has been programmed which is based on the finite element model of the deformed sheet. This radiation length is a direct result of the averaged traversed path of a particle through the sheet, emerging from a fixed point. The calculation procedure of the radiation length is described in Section 6.3.

The value of the objective function is determined by the settings of the design variables. In order to have a limited number of design variables, the design of the current RF Foil has to be parameterized. The settings of the design variables of this parameterized model determine the value of the objective function. This objective function value must be determined by means of an FE calculation. The parameterization of the RF Foil is covered in Section 6.4.

The ranges of the design variables are bounded, for instance, due to the fact

that the RF Box must contain a well-defined set of silicon detectors. Impossible or limited combinations of design variable settings result in a set of explicit constraints. More complex defined constraints, such as the leak rate or the mechanical stiffness, are called implicit constraints. The value of these constraints must be determined by means of FE analyses. The constraints on the RF Foil are described in Section 6.5.

All FE simulations to be carried out on the RF Foil to determine the value of the responses are computationally expensive if the whole RF Foil (or a quarter because of double symmetry) has to be analyzed for each design. Therefore, a simplified model is used which represents the whole RF Foil. Analyzing this simplified model will save a considerable amount of simulation time. The results of the simulations on this simplified model will be translated to corresponding results for the whole RF Foil. The translation procedure is discussed together with the discussion of the design variables and the constraints in Section 6.4 and 6.5.

The objective function, design variables and constraints are used as an input for OptForm. This program is used to help in developing an optimized RF Foil. This is the subject of Section 6.6.

6.1 Optimization theory: a brief description

This section presents a short introduction to optimization theory, in so far applicable to the optimization problem concerning the RF Foil. This means that a single objective function is sufficient to deal with. The value of this function is determined by the value of the design variables, subject to implicit or explicit constraints.

6.1.1 Description of the optimization problem

Figure 6.1 shows an example of an optimization problem in a graph, where two design variables x_1 and x_2 determine the value of the objective function f. In the area which is bounded by the five constraints g_1 to g_5, the minimum value of the objective function is found to be equal to f_{opt}. This is the case if the two design variables are equal to x_1^* and x_2^*.

The procedure to find the optimal values for the design variables must in many cases be determined numerically. An optimization algorithm has to determine in an iterative way where the optimum is situated. Figure 6.2 depicts the general optimization procedure to reach a satisfactory minimum value of the objective function. Starting from an initial design, an optimization algorithm should improve the design until a minimum value for the objective function is found. In that case, the resulting design can be considered optimal.

Three questions can be asked:

- how do you choose an initial design? If the design is a technological innovation, a solution for this question is hard to find, since there is no experience

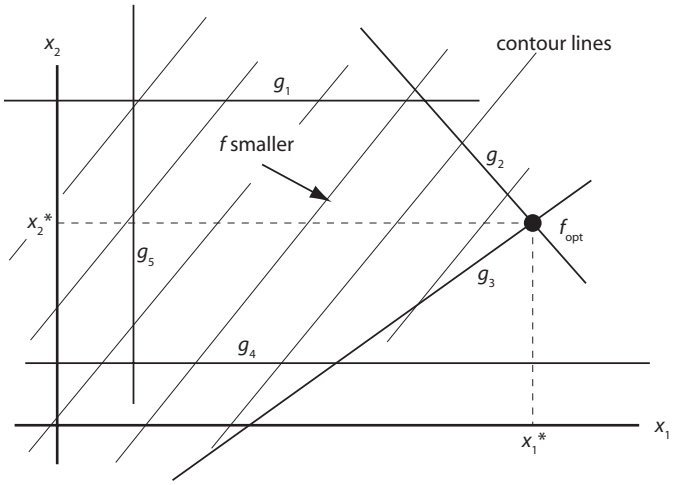

Figure 6.1: Graph showing the contour lines of the objective function f as function of the design variables x_1 and x_2, subject to constraints.

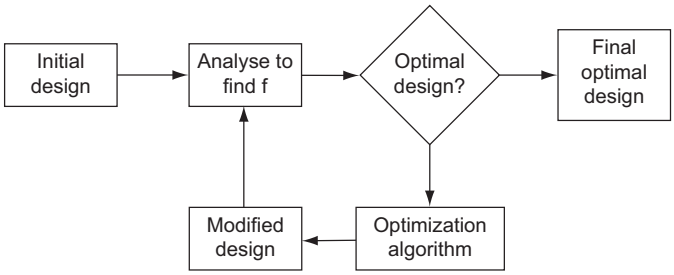

Figure 6.2: General solution scheme for optimization problems.

in designs of this type. A good initial design requires design skills;

- how can the design be improved at each stage of the optimization process? Characteristics can be contradictory, leading to a decline in one property while improving another property;

- when can the process be ended, to consider the design sufficient enough to conclude that it is optimized? What is the convergence norm and how is it known that a global minimum has been reached instead of a local minimum?

6.1.2 Characterization of the optimization problem

In general, an optimization problem is much more complex than as presented in Figure 6.1; this is also the case for the optimization of the RF Foil. Answering the three questions mentioned above will be a complex task and may depend heavily on the character of the optimization problem.

In Figure 6.1, the objective function and the constraints are linear functions of the design variables. This is not always the case. These functions may even not be known beforehand. Secondly, the optimum point which is found may be a local or global minimum, but the search is always for the global minimum. The existence of local minima means that the problem is non-convex. In the third case, the design variables do not have to be continuous. An example of a non-continuous (discrete) variable is the initial sheet thickness of which the product is made. In the last case, extra complexity may be involved if the value of the objective function can only be derived from (finite element) simulations; the problem is then simulation-based. This kind of optimization can introduce numerical noise [30, 38], which can affect and distract from the optimal solution.

6.1.3 Optimization algorithms

Dependent on the character of the optimization problem, an optimization algorithm should be chosen. This algorithm should find the minimum of the objective function in an efficient and effective way. The optimization problem in Figure 6.1 is relatively easy to solve, for instance by using Lagrange multipliers to incorporate the constraints into the objective function. If the global optimum did not lie on a line representing a constraint (in other words: no constraints are active), then at the optimum point

$$\nabla f = 0 \tag{6.1}$$

If one or more of n constraints are active, then the Lagrange multipliers λ_j ($j = 1$ to n) are incorporated into this equation as

$$\nabla f + \sum_{j=1}^{n} \lambda_j \nabla h_j = 0 \tag{6.2}$$

with h_j being the equality constraint j. An equality constraint is always defined as

$$h_j = 0 \tag{6.3}$$

where an inequality constraint is written as

$$g_i \leq 0 \tag{6.4}$$

In the case of a solution type with Lagrange multipliers involved, inequality constraints are treated as equality constraints. If the optimization problem is more

complex, several other algorithms are available to solve this problem. A few are mentioned in [1, 77], and briefly described below.

Method of Conjugate Directions This method is based on the method of Steepest Descent, where in a point defined by a set of design variables not only the objective function is determined, but also the derivative of this function with respect to the design variables. The method of Steepest Descent gives a search direction for the improved design. This method does not converge very fast, the Method of Conjugate Directions results in faster convergence. Here, not only the first derivatives are used, but also the second derivatives (Hessian). This gives better information about the search direction for the improved design.

This method works very well if the objective function is quadratically dependent on the design variables, but this method can quickly lose its accuracy if higher order dependencies are present. This method is a *line search* method, where the search direction is determined first, after which the search distance is determined.

Trust Region methods Around a point representing a design, a quadratic model is built of the objective function. This quadratic model is believed to be accurate enough within a region, called the Trust Region. Within this region, the quadratic model is minimized. At this new minimized point (i.e. the new design), the objective function value is evaluated and compared with the value according to the quadratic model. The deviation between these two numbers determines the accuracy of the quadratic model and the Trust Region size in the next iteration.

In the Trust Region method, the search distance is determined first, after which the search direction is calculated. So, this is contrary to the line search method. The main drawback of the Trust Region Method is if the quadratic model is not adequate enough, many iterations may be necessary to obtain considerably smaller subspaces.

Genetic algorithms Genetic algorithms are based on the principle of survival of the fittest. It is an evolutionary algorithm where there is not one initial design, but a population of initial designs. All the members of this population have their own value for the objective function. The members of this population are called the first generation. In the second generation, also a set of designs, for each of the new designs ('children') two parents are chosen. The smaller the objective function of a member of the first generation, the higher the chance that it will become a parent for the second generation.

This method is inspired by the evolution theory, and can be extended with characteristics from this theory, as mutations and cross-overs. Each next generation will generally consist of fitter members than the previous generation. The main drawback of this method is that many objective function evaluations are necessary in each generation to derive the members of the next generation.

Metamodeling techniques These statistical optimization methods can be used for very complex optimization problems. They are sequential in nature, that means that a fixed sequence of steps has to be taken to improve the design in order to find the optimal design with the lowest value of the objective function. The first step is a screening step to explore the bounds of the design space. This step is also used to determine which design variables have the highest impact on the objective function value. In the second step, a so-called Design Of Experiments (DOE) is established, consisting of a set of well-defined designs within the design space. After evaluating the objective function values of these designs, a series of expressions can be fitted through these points (designs). Statistical tools are used to test the validity of the expressions. The minimum in the expression with the highest quality of fit is searched for (or more minima if there are local minima), and a new DOE may be established in a smaller region. One of the mathematical tools to describe a metamodel is the *Response Surface Methodology* (RSM).

This method requires a considerable amount of objective function evaluations, so it is of crucial importance that an effective DOE is made. The nature of RSM is that this amount of evaluations can give much information on the way the objective behaves under a variation in the design variables. A major disadvantage arises if the equations to fit the data are far from reality.

The main reasons to choose this method in this project are

- a metamodeling techniques is a relatively effective method to distinguish between local and global minima;
- metamodeling techniques are effective methods for complex optimization problems where the value of the objective function is not an analytical function, or if this function is not known;
- with the application of e.g. genetic algorithms, the aspect 'luck' plays a role. This is far less likely if a mathematical tool such as RSM is used.

The next section describes more elaborately the theory of RSM.

6.2 Optimization strategy

Each set of design variables results in one value for the objective function, in Response Surface Methodology (RSM) [11, 58] also called *response*. The RSM creates a number of designs for which the response is evaluated. The whole set of responses can be graphically depicted, for instance if only two design variables are influencing the response. Fig 6.3 shows an example of the response y as function of two variables x_1 and x_2. A predetermined space defined by upper and lower limits on x_1 and x_2 is explored in a series of points. A surface function will then be fitted through the obtained response values (objective function and constraints),

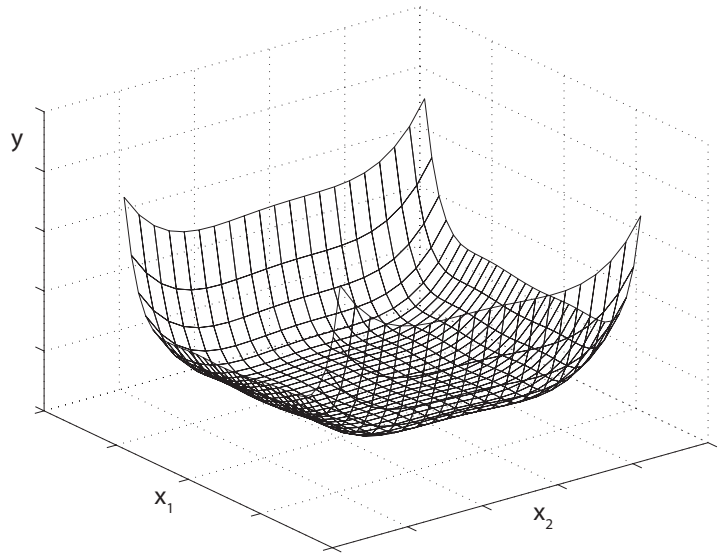

Figure 6.3: Response y as a function of the design variables x_1 and x_2.

this surface is called a metamodel of the original model. The optimal design is then found by minimizing this fitting function. Since this function will generally deviate from the real situation, it may be necessary to redo an RSM step on a smaller region around this point.

6.2.1 Screening experiment

Before exploring the design space, a screening step is done where the bounds of the design variables are explored. This step is especially important if many design variables are involved. The screening step can determine which design variables have the highest impact on the response. Design variables with low impact will have fixed values in the subsequent metamodeling steps.

The way the screening is performed is that the corner points of the design space will be evaluated. In the case of two or three variables, the number of evaluations is not too high, see Figure 6.4. Two variables require four objective function evaluations, three variables require eight evaluations. In general, k variables require 2^k design evaluations in case all corner points are considered. This situation is called

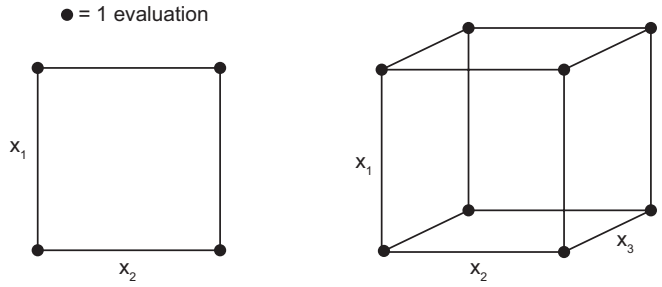

Figure 6.4: Two design variables require four corner evaluations, three design variables require eight.

a *full factorial design*. If k becomes larger, then very quickly the number of objective function evaluations will become too large to be efficient for the optimization method.

In the case of many design variables, a selection of design evaluations must be made, thereby making it a *fractional factorial design*. For example, a fractional factorial design in the case of three design variables is depicted in Figure 6.5, where four instead of eight points are evaluated. Here, the number of objective function evaluations is 2^{k-1}. In general, a fractional factorial design consists of 2^{k-p} evaluations, where the value of p is dependent on k, and also on the interactions between the design variables.

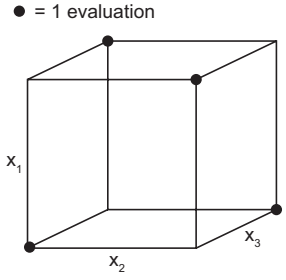

Figure 6.5: Fractional factorial design in the case of three design variables.

The result of the screening experiment is a table or graph (Pareto plot) in which the design variables are ordered from highest to least influence on the value of the objective function. The design variables with a relatively high impact are used in the subsequent stages of the RSM optimization procedure.

6.2.2 Design of Experiments

The first step, after the screening step has been performed, is to explore the design region within the limits of the design variable settings. At several points within this region, the value of the objective function is evaluated. The distribution of points in the region to be evaluated, is called the Design of Experiments (DOE). A method to determine the points to be evaluated is the *Spacefilling Latin Hypercube Design* [67]. The design space is filled with designs such that the minimum distance between all points is maximized. After evaluating all the response values from these designs, a set of fitting equations is available which can be used to represent the responses as closely as possible. Examples of these functions are a linear function (with or without interaction terms between the design variables), an elliptic function and a quadratic function. Another type of metamodel is called *Kriging*, which is also described in the next section. The equation which results in the best fit is used as the optimal metamodel. This metamodel will then be minimized.

If this minimized point is not satisfactory, a new DOE is established, either in a smaller region, or new points within the existing region will be added. After evaluating, the responses are fitted again in a suitable function. The DOE process should be repeated as often as necessary, in order to find the global optimum.

6.2.3 Fitting a model

In many cases, it is not known beforehand if the current DOE is in the region of the optimum. It should then be tested which of the function types is best to use. After fitting the obtained responses from a DOE with one of the function types, the quality of this fitting function has to be evaluated. To determine the quality of fit, several techniques are available for this test. The most common one is the Analysis of Variance (ANOVA). Within this method, the quality of the fit can be determined by a set of numbers, a few of them are:

- the standard deviation between the observed (evaluated) objective function value and the fitted function values;
- the coefficient of multiple determination R^2: this number is a function of the error sum of squares SS_E and the total sum of squares SS_T. The error sum of squares is the sum of the squares of differences between the evaluated value and the predicted value by the metamodel. The total sum of squares is the sum of the squares of differences between the evaluated value and the mean value of the responses. The total number of squares can be partitioned into an error part (SS_E) and a part due to the metamodel (SS_R). The coefficient of multiple determination is written as

$$R^2 = 1 - \frac{SS_E}{SS_T} \tag{6.5}$$

The closer this value to 1, the better the fit;

- because the coefficient of multiple determination increases when more terms in the metamodel are added, this value is not always a good measure. Therefore an adjusted value is defined, which does not necessarily increase if the number of terms is increased, this is called R^2_{adj}. It is even possible that this value decreases if unnecessary terms are added. This value is defined by

$$R^2_{\text{adj}} = 1 - \frac{n-1}{n-p}(1-R^2) \tag{6.6}$$

  where n is the total number of observations and p is the number of model parameters (degrees of freedom) for the function type to be used. The denominator in Equation (6.6) decreases with the number of model parameters, the term $(1-R^2)$ increases with the number of model parameters;

- the $RMSE$ (Root Mean Square Error) value: this is a value which is dependent on SS_E and is defined as

$$RMSE = \sqrt{\frac{SS_E}{n-k-1}} \tag{6.7}$$

  where k is the number of regression variables. The $RMSE$ should be as low as possible, indicating that the squared sum of errors is low, combined with a low number of regression parameters.

Kriging A function fit like a linear or a quadratic equation always shows an error, not only in the unknown points, but also in the known points where the objective function values have been evaluated. Kriging interpolation is a technique where the fitted function goes through the known points, so the error in these points is zero. At unknown values in between the known values for the objective function, the value f^* is estimated as a function of (all n) known values as

$$f^* = \sum_{i=1}^{n} \lambda_i f_i \tag{6.8}$$

where λ_i is a weight factor for the known value f_i, the sum of all these weight factors is equal to 1. In theory, all n function values are taken into account but this can take too much effort if n is large. Therefore, a limited number of values of points in the vicinity of the point in consideration is taken into account. Figure 6.6 shows the difference between an RSM (in this case quadratic) and a Kriging interpolation function. Also, a gray colored confidence interval is shown for the Kriging procedure for the intermediate points. This can give insight in the phenomenon whether a local or the global minimum is situated between two known points. In the case of

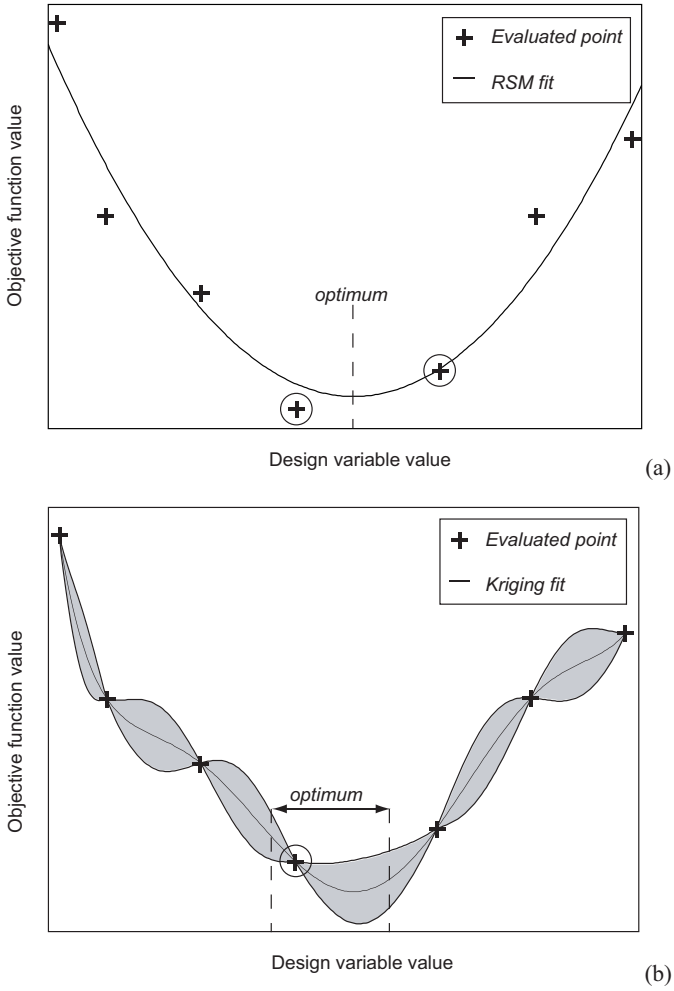

Figure 6.6: Quadratic (a) and Kriging (b) function fit of sampled points, the Kriging fit is extended with a confidence interval in between two known points.

the quadratic fit, the optimum is found between the two circled evaluation points. In the case of the Kriging fit, there is a chance that the global optimum is situated left of the circled evaluation points.

At a point where the function value has not been evaluated, this value can be estimated by Kriging. This estimate is based on the function value of the evaluated points in the neighborhood of the point to be estimated. If this estimate is based

on a constant mean value of the function value of the known points, then this is called zeroth order Kriging. It is also possible to fit the mean by using a linear (first order Kriging) or a parabolic (second order Kriging) trend of the mean value.

6.3 RF Foil optimization goal

Particles traveling through matter lose part of their kinetic energy. In order to measure these particles with a detector, the reduction of kinetic energy should be as low as possible, to ensure that the measurement is accurate. This means that a particle should pass through as little material as possible on its way to the detector. If the direction of this particle is not known, but the origin is known, then an average distance can be calculated representing the amount of matter which is traversed. This will be called the *average traversed path* as seen from a point. This point is called the interaction point, or IP. The combination of average traversed path and the material type which is traversed determines the radiation length of a part, which is the optimization goal for the RF Foil.

This section describes the method with which the percentual radiation length can be calculated. This method is based on the deformed configuration of the finite element model, taking into account the elemental thicknesses and surface areas.

6.3.1 Definition of the view factor

Calculation of view factors is a common technique in the field of thermal radiation, where two flat surfaces radiate heat towards each other. The amount of heat radiated from a surface A_i to a surface A_j depends on the field of view of surface A_j as seen from surface A_i. In other words, this is the fraction of the total view angle (4π) which is occupied by the other flat surface. This is called the view factor F_{ij} and is defined as [52]:

$$F_{ij} = \frac{1}{A_i} \int_{A_i} \int_{A_j} \frac{\cos\theta_i \cos\theta_j}{\pi S^2} \mathrm{d}A_i \mathrm{d}A_j \tag{6.9}$$

in which A_i and A_j are the surface areas of the elements e_i and e_j respectively. The variables θ_i and θ_j are the angles between the surface and the normal vector of the other element. The distance between the differential elements dA_i and dA_j is S. If one of the surfaces, say A_i, is assumed to be a point i (so it has no surface area), then Equation (6.9) simplifies to

$$F_j = \int_{A_j} \frac{\cos\theta_j}{\pi S^2} \mathrm{d}A_j \tag{6.10}$$

because the integral over A_i of $\mathrm{d}A_i$ is equal to 1. Since the view direction from this degenerated point can be considered as pointed towards A_j, also $\cos\theta_i$ is equal to

1. If A_j is a small enough surface with respect to the distance S to this point i, for instance if this surface is a finite element far enough from i, then the integral over A_j of $\mathrm{d}A_j$ is equal to its surface area A_j, so:

$$F_j = \frac{A_j \cos\theta_j}{\pi S^2} \tag{6.11}$$

The distance S should represent the average distance from point i to the surface A_j. Taking the midpoint of A_j can give inaccurate results, this can be seen if the normal of the element is pointed towards i. The midpoint is the closest point, this gives a systematic error in the distance calculation. A better method is to calculate an average distance based on the midpoint and the four corner points (in the case of quadrilateral elements) as

$$S = \frac{\sum_{j=1}^{4}(d_j^e + 4d_{\mathrm{m}}^e)}{8} \tag{6.12}$$

where d_j^e is the distance from point i to the corner point j of element e and d_{m}^e is the distance from point i to the midpoint of element e.

6.3.2 Calculation of the averaged traversed path

The average traversed path $\hat{t}$ is dependent on the view factor and on the thickness of the traversed element. Figure 6.7 shows a particle emerging from the interaction point IP, crossing element e. The picture shows a 2-dimensional situation. The traversed path through the element is t_θ. This path length is dependent on the orientation ϕ of the element with respect to IP and the angle θ_e. If the traversed

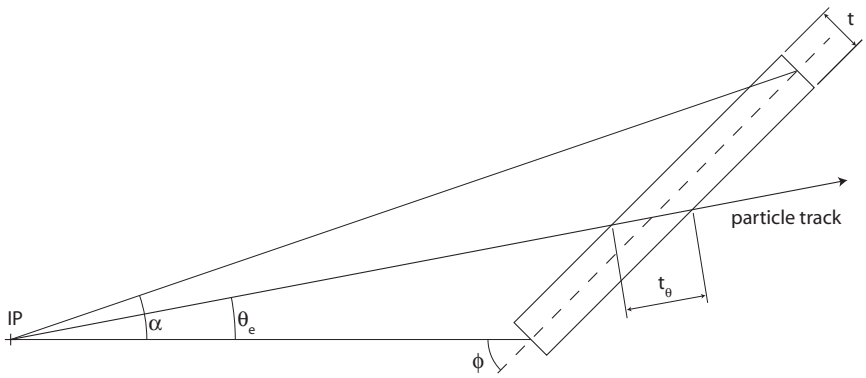

Figure 6.7: Particle crossing element e, the traversed path is t_θ.

path through the element is averaged over a full circle around IP, then the average traversed path $\hat{t}$ is

$$\hat{t} = \frac{1}{2\pi} \int_0^{\alpha} \frac{t}{\sin(\phi - \theta_e)} \mathrm{d}\theta_e \tag{6.13}$$

In three dimensions, in the case of shell elements, this method to calculate the average traversed path becomes very cumbersome. A simplification can be made, of which the underlying assumption is supported by Figure 6.8.

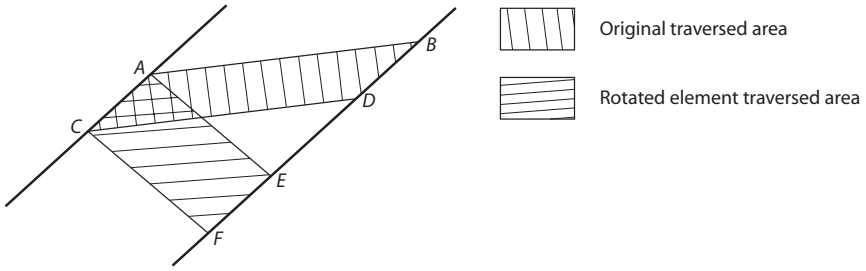

Figure 6.8: Both hatched areas are the same, being the length AC times the thickness t.

If α is not too large, then the surface area of both hatched regions in the figure are the same, because the lines AB and CD, which point towards the interaction point, can then be considered parallel. The same holds for the lines AE and CF. If these areas are the same, this would mean that the average traversed path of this element would not change if this element is rotated. This also accounts for a 3-dimensional situation, where the traversed volume does not change if the element were rotated. Calculation becomes easier if the element is then rotated in such a way that the element normal points towards the direction of the interaction point. Then $\cos\theta_j$ in Equation (6.11) becomes 1. The average traversed path then becomes

$$\hat{t} = F_{j(\mathrm{IP})} \cdot t \tag{6.14}$$

where $F_{j(\mathrm{IP})}$ is the view factor of the rotated element of which the normal points towards IP. So, substituting Equation (6.11) into Equation (6.14) results in

$$\hat{t} = \frac{A_j t}{\pi S^2} \tag{6.15}$$

The element area can be calculated as a function of the coordinates of the element corner nodes. Figure 6.9 shows an element with four corner nodes 1 to 4. The element is divided into four triangles. The coordinates of the midpoint MP are the average of the corresponding coordinates of the four corner nodes. The lengths

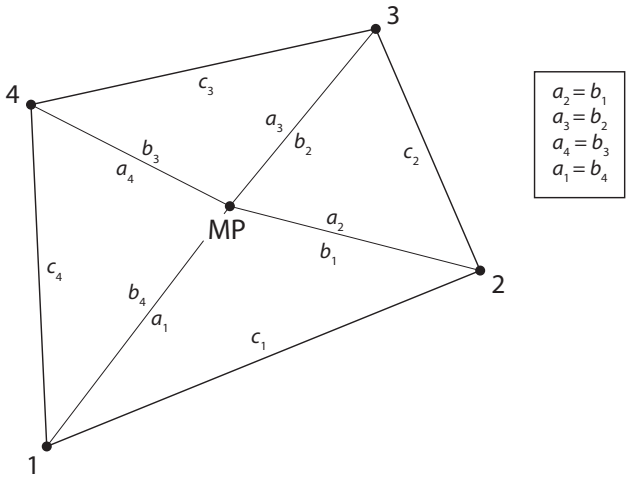

Figure 6.9: One element with four corner nodes 1 to 4, used to calculate the element area.

of the element edges and the distances from the midpoint to the corner nodes are shown in the figure. The element area A_e is now calculated as follows:

$$s_i = \frac{1}{2}(a_i + b_i + c_i) \qquad i = 1..4 \tag{6.16}$$

$$A_i = \sqrt{s_i(s_i - a_i) \cdot (s_i - b_i) \cdot (s_i - c_i)} \qquad i = 1..4 \tag{6.17}$$

$$A_e = \sum_{i=1}^{4} A_i \tag{6.18}$$

6.3.3 Calculation of the radiation length

The determination of the percentual radiation length is now relatively easy, since this number is linearly related to the averaged traversed path. For definitions of the radiation length and percentual radiation length, see Section 1.2.1. The contribution of element e to the percentual radiation length $X_{0(e)}(\%)$ is

$$X_{0(e)}(\%) = \frac{\hat{t}}{X_0} \tag{6.19}$$

where X_0 is the material radiation length, which is 89 mm for aluminum. The overall percentual radiation length of the deformed structure is

$$X_0(\%) = \sum_{e=1}^{\#elements} X_{0(e)}(\%) \tag{6.20}$$

The value of $X_0(\%)$ is the number which has to be minimized. In other words: the objective function is $F_{\text{obj}} = X_0(\%)$.

6.4 RF Foil design variables

Since the design of the RF Box has been merely a process of trial and error, the dimensioning of this box is not suitable for parameterization. There are too many geometric entities to make the RF Box an efficient design to be used in an optimization procedure. This section describes a way to parameterize the RF Box, in particular the RF Foil, to reduce the number of design variables. In Chapter 1, it was explained that the RF Foil is the top sheet of the RF Box. The main characteristics of the RF Box must be maintained, in order to fulfill its main functions (containing the detectors, minimizing wake field suppression). In this section, the parameterization is described step by step, thereby producing a list of design variables to be used in the optimization procedure.

6.4.1 Dimensioning of the RF Foil

The box, especially the RF Foil, should consist of a set of parameters which mainly characterize the geometry. The dimensioning of the box must be such that it can contain the silicon detectors. Two rows of these detectors, each in its own RF Box, should overlap when two boxes are situated correctly with respect to each other. An assembly of two of these boxes should leave a free channel for the accelerator beam to pass through.

Figure 6.10 shows how the geometry can be parameterized, a quarter of the simplified foil has been displayed, due to double symmetry of the foil. Also, for simulation efficiency reasons, not the whole length of the foil is modeled, but only a model which is comparable to the one which was shown in Figure 1.5. Two dimensions in the figure are not a variable. One fixed dimension is the pitch from detector to detector, which is 30 mm. The other fixed dimension is due to the silicon detector dimensions. The dimensions as shown in the figure have the following functions and limits:

- The dimension H_1 is the corrugation height. The minimum height is determined by the positioning of the silicon sensors. This height is the same as in the current design of the RF Foil, i.e. 10 mm. The maximum corrugation

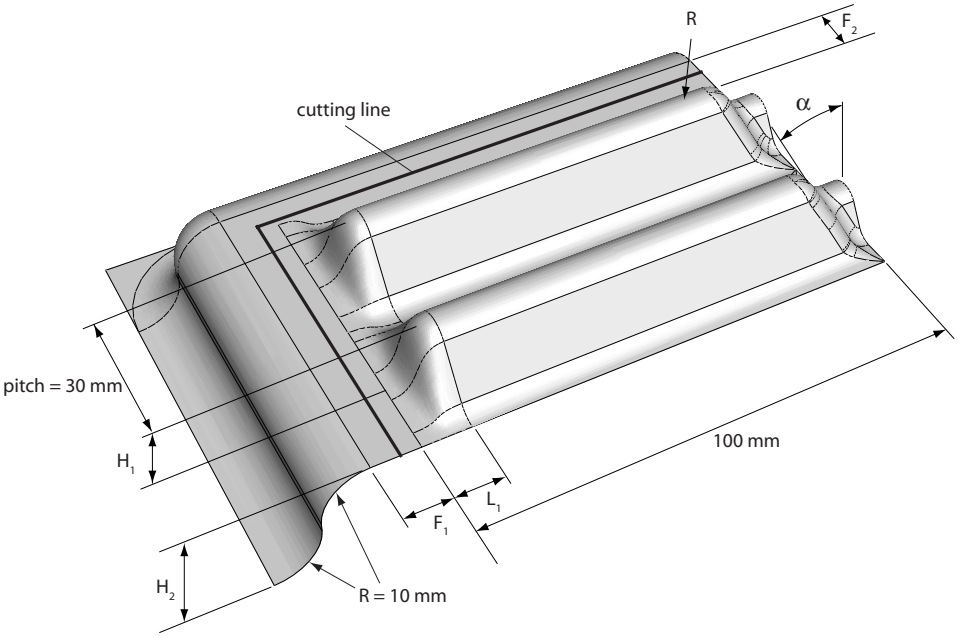

Figure 6.10: Main dimensions of the RF Foil.

height is determined by the ability to suppress wake fields, and is maximized to 20 mm. To apply and to provide some safety, the maximum corrugation height is chosen to be 15 mm.

- The dimension H_2 is a parameter which is responsible for the average sheet thickness of the deformed sheet. If no extra height were applied, then the deformed sheet would be too thick, since the maximum cavity depth is relatively low. This cavity depth is increased by this parameter. A minimum is chosen of 30 mm, the maximum height is in principle not bounded, but will be chosen here to be 70 mm.

- The dimension F_1 determines the sheet thickness distribution in the length direction of the corrugations. A low value means that in the midline of the RF Foil (where the proton beam line is running), the thickness is relatively high. More towards the outer edge of the RF Foil, the sheet thickness would then be relatively low. Increasing this dimension will lead to a better distribution. The minimum value is 10 mm, the maximum value is 50 mm.

- The dimension F_2 has generally the same function as the previous one. The

difference is that this dimension mainly takes care of the thickness distribution between the separate corrugations. Especially the thickness in the first corrugation is determined by this dimension. Just as with F_1, the range of this dimension is 10 to 50 mm.

- The dimension α has a more local function. It is the draft angle at the endcap side at the position of the beam line. This dimension has an influence on the local thickness in the top end of the corrugations. The minimum angle is 10^o, the maximum value is 30^o. Making this angle larger will result in missing too much detection space.

- The dimension L_1 has the same function as α, but then on the other endcap side of the corrugations. This dimension ranges from 10 to 15 mm, keeping in mind the geometry of the detecting silicon sensors.

- The dimension R is the radius of the long side of the corrugations. Since the pitch between the corrugations is fixed at 30 mm, this dimension is not only a fillet radius, but it also has an effect on the draft angle on the side walls of the corrugations. The radius R ranges between 4 and 6 mm.

The model shown in Figure 6.10 has to be cut along the bold lines to result in the part that will contribute to the RF Foil. So, the dimensions H_2, F_1 and F_2 are only used to obtain a well-defined thickness distribution within the area bounded by these bold lines. The dimensions of the trimmed area are 105 x 65 mm.

6.4.2 Radiation length of the simplified model

The model shown in Figure 6.10 shows a simplified version of the full RF Foil. All calculations concerning the optimization of the RF Foil will be carried out with this simplified model. The results in terms of the radiation length of the simplified model should be translated into a radiation length of the full RF Foil. This is done by determining a multiplication factor. The radiation length of the RF Foil is then calculated by multiplying the radiation length of the simplified model by this factor.

The radiation length of the simplified model is only determined for the part that falls within the area that contributes to the RF Foil (105 x 65 mm). The full RF Foil has 23 instead of four corrugations, so the total surface area is (23/4) times larger than the surface area of the simplified model. This does not mean that the radiation length is (23/4) times larger for the full RF Foil, since a large part of this foil is situated relatively far away from the interaction point. This means that for equal surface areas, the view factor at these higher distances is lower, and thus the average traversed path.

An analytical solution cannot be found for this complex structure. The radiation lengths have therefore been calculated numerically. Both a set of simplified

models and a set of full RF Foils (each one by one with the same values of the parameterized dimensions and the thickness) were meshed into finite elements. The results of these radiation length calculations showed that the average multiplication factor is 3.20, see Table 6.1 for an overview of four configurations. These configurations are determined by a fractional factorial design with three design variables, compare with Figure 6.5. The assumed average sheet thickness is 0.25 mm, as is the case for the current RF Foil, but the ratio is independent of this thickness.

Table 6.1: Radiation length calculations for four configurations of the simplified (X_0^{s}) and the corresponding full (X_0^{f}) RF Foil model.

#	H_1	R	α	X_0^{s}	X_0^{f}	ratio
1	15	4	10	2.440	7.891	3.24
2	10	6	10	2.243	7.044	3.14
3	10	4	30	2.275	7.188	3.16
4	15	6	30	2.313	7.586	3.28

6.4.3 Neglected design variables

The initial sheet thickness used is 0.3 mm, in order to produce an RF Foil which is as thin as possible, but without showing a leak. This is the minimum sheet thickness which can be provided, and is therefore used in the optimization procedure. However, it should not be neglected that it may be possible that, for instance, the thickness distribution for an initial sheet thickness of, say, 0.5 mm, will lead to a better objective function value. This possibility should only be studied if the results for an initial sheet thickness of 0.3 mm are not satisfactory. The initial sheet thickness is an example of a discrete design variable.

The second neglected design variable is not a product dimension, this is the target strain rate. In Chapter 4, the optimal target strain rate was calculated as $8.3{\cdot}10^{-4}\ \mathrm{s}^{-1}$. This value will be used as target value for the optimization procedure.

The third design variable not taken into account, but which could be used, is the value of the applied backpressure. Since all experiments show that an increase of the backpressure will positively influence the results (lower void volume fractions at corresponding equivalent plastic strain values), the applied backpressure during the optimization procedure is always 30 bar.

6.5 Constraints on the RF Foil

In Section 1.5, the requirements on the RF Foil were described. In total, five requirements were presented which are acting as constraints on the design of the RF Foil. These are the constraints concerning:

- the leak tightness of the formed sheet, as a maximum value of the overall leak rate;
- a sufficient wake field suppression. It was already concluded that this constraint is incorporated into the dimensioning of the parameterized model, so it will not be discussed again in this section.;
- the maximum displacement as a result of a 2 mbar overpressure;
- the maximum stress as a result of a 6 mbar overpressure;
- the first natural frequency of the RF Foil.

These constraints, and the impact on the design variables, are described in this section.

6.5.1 Leak rate constraint

The requirement on the current RF Foil is that for an overpressure of 25 mbar He, the maximum allowable value for the leak rate is $1 \cdot 10^{-8}$ mbar·l/s. From Equation (4.21), it follows that the leak rate is proportional to the overpressure Δp. All the specimens formed during the bulge experiments were leak tested at an overpressure of 1 bar He (i.e. atmospheric pressure). The leak rate implementation according to Equation (4.22) is referenced to this 1 bar overpressure. This means that the maximum allowable leak rate at 1 bar overpressure is then (1 bar/25 mbar)$\cdot 1 \cdot 10^{-8}$ mbar·l/s $= 4 \cdot 10^{-7}$ mbar·l/s.

The simplified model is about six times smaller than the full RF Foil. This means that about one sixth of this leak rate is allowable in the simplified version of the foil. Therefore, the maximum leak rate in the simplified model will be constrained to $7 \cdot 10^{-8}$ mbar·l/s.

6.5.2 Mechanical constraints

Just as with the leak rate and the radiation length, the mechanical constraints also have to be translated from the full RF Foil to the simplified model. This has been done the same way as was carried out with the radiation length calculations. For a set of dimensions for the parameterized model, calculations have been done on the simplified model and the full RF Foil model. The material properties used are those of AA5083 at room temperature, since this is the temperature at operating

conditions. Under this condition, ALNOVI-1 has a Young's Modulus of 69 GPa and the density is 2700 kg/m^3. The maximum allowable stress in the material before failure is 160 MPa. The calculations resulted in factors to be used as multiplication on the values calculated for the simplified model.

- the displacement is assumed to be the result of elastic deformation, the maximum allowable displacement is 1 mm. The deformations in both the simplified model and the full RF Foil model have been calculated in different combinations of the design variable parameters. An average multiplication factor of 5.22 is found. This means that the maximum allowable displacement in the simplified model with a 2 mbar pressure acting on it is 0.192 mm.
- The maximum stress in the structure may not exceed the yield limit. This means that in the full RF Foil, an equivalent stress of 160 MPa may not be exceeded. The same procedure has been followed as with the calculation of the deformation multiplication factor. This led to an average multiplication factor on the stress of 6.0. This means that in the simplified model, the stress may not exceed 27 MPa under a pressure load of 6 mbar.
- Also, the ratio of the first natural frequencies were calculated between the simplified and the full RF Foil model. This led to a multiplication factor of 0.52, the first natural frequency of the simplified model is almost twice as high. The minimum allowable natural frequency of the full RF Foil is 50 Hz. This means that the first natural frequency of the simplified model should be at least 96 Hz.

6.6 Optimization results

The optimization problem now can be formulated as:

- minimization of the objective function, which is the percentual radiation length;
- minimize this function by finding an optimal combination of seven design variables: H_1, H_2, F_1, F_2, α, L_1 and R.
- the optimization problem is subject to four constraints, concerning leak tightness after the forming process, elastic deformation caused by overpressure, stress limit caused by overpressure and the first natural frequency.

In this section, the results of the optimization procedure are presented. For this procedure, OptForm has been used in the main part. The results of the screening Design of Experiments were used to determine the design variables which have the highest influence on the value of the objective function and/or the constraints. With this information, a Design of Experiments considering the remaining design

variables was established, of which the results were used to create a metamodel fit through the responses. OptForm provides seven fitting function types, of which four are RSM functions: linear without and with interaction terms, elliptic and quadratic. Also three Kriging types of fit are available: 0-th, first and second order. The quality of fit determines which one will be used to determine the optimum.

6.6.1 Screening Design of Experiments

With the seven design variables, a fractional factorial design was established in OptForm. A total of eight designs created by OptForm had to be evaluated, Table 6.2 shows the eight designs.

Table 6.2: Design variable settings for the Screening Design of Experiments.

Des. Variable	H_1	H_2	F_1	F_2	α	R	L_1
	10	30	10	50	30	6	10
	10	30	50	50	10	4	15
	10	70	10	10	30	4	15
	10	70	50	10	10	6	10
	15	30	10	10	10	6	15
	15	30	50	10	30	4	10
	15	70	10	50	10	4	10
	15	70	50	50	30	6	15

First, a few of these simulations have been done to obtain information concerning the pressure to be applied during the forming process. It seemed that the dimension H_2 mainly determined the pressure application in time. A linear pressure rise in time is sufficient to be sure that the target strain rate will nowhere in the model be exceeded too much (i.e. more than 20%). The best fit to accomplish this target by the pressure p in time t (in seconds) turned out to be

$$p = (3.2 - 0.025H_2)\frac{t}{1500} \quad \text{bar} \tag{6.21}$$

With this pressure rise, for each of the designs the value for the objective function and the constraints are calculated. In the case of the radiation length, the value of the objective function is the radiation length of the corresponding full RF Foil, by using the multiplication factor of 3.20.

All constraints $g_i, i = 1..4$ must be defined such that the value of a constraint for a specific design is negative if the constraint is met, and positive if the constraint is

violated. Keeping the multiplication factors in mind as determined in the previous section, the values for the constraints are:

$$\text{leak rate } L: \qquad g_1 = \log(L) - \log(7 \cdot 10^{-8}) \tag{6.22}$$

$$\text{deformation } u: \qquad g_2 = 5.22u - 1 \tag{6.23}$$

$$\text{stress } \sigma: \qquad g_3 = \frac{6.0\sigma - 160}{160} \tag{6.24}$$

$$\text{first natural frequency } f: \qquad g_4 = 1 - \frac{0.52f}{50} \tag{6.25}$$

The constant term of 160 in Equation (6.24) represents the uniaxial yield stress in the material at room temperature.

Table 6.3 summarizes the results from the finite element calculations of each of the screening designs. The table contains, besides the values for the objective function and the constraints, the minimum, maximum and average value of the resulting sheet thickness.

Table 6.3: Results of the screening Design of Experiments.

DOE	F_{obj}	g_1	g_2	g_3	g_4	$t_{\min}$	$t_{\max}$	t_{avg}
1	5.216	-2.845	-0.553	-0.739	-1.632	0.167	0.251	0.208
2	5.158	-2.845	-0.583	-0.738	-1.667	0.180	0.257	0.219
3	3.446	2.980	1.673	0.031	-0.488	0.076	0.162	0.111
4	3.670	1.770	0.485	-0.321	-0.793	0.092	0.168	0.126
5	4.874	0.792	-0.365	-0.573	-1.168	0.111	0.223	0.165
6	5.117	0.227	-0.384	-0.574	-1.249	0.110	0.233	0.175
7	3.763	4.176	0.221	-0.071	-0.853	0.063	0.176	0.121
8	3.946	2.037	0.188	-0.352	-0.743	0.086	0.187	0.132

Two remarks have to be made about this table. Firstly, g_4 is always negative. This means that the first natural frequency of all the design points is always higher than 96 Hz. The constraint concerning the first natural frequency is always met, indicating that this constraint will never be active regardless of valid combinations of the design variables.

Secondly, if g_1 is negative, all other constraint values are negative. This would mean that the leak rate constraint is the only active constraint. Since g_1 is only negative in the first two designs of the screening, it is too early to say that this will always be the case.

In the subsequent stage of the optimization process, it is not desirable that all design variables will be involved, since this will then become computationally

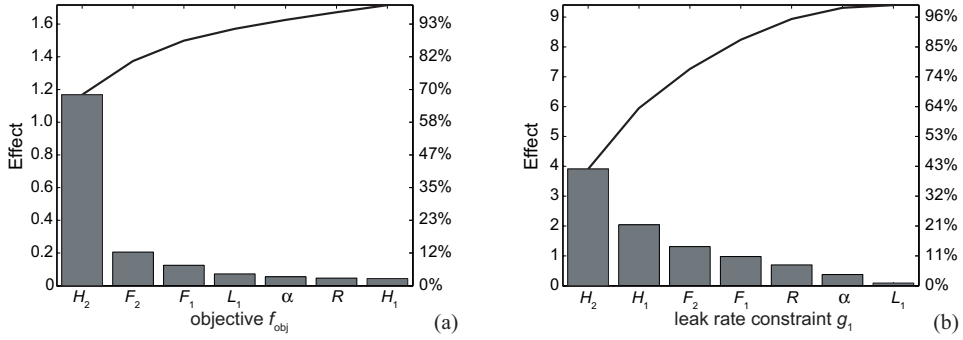

Figure 6.11: Pareto plots of (a): the objective function and (b): the leak rate constraint.

very expensive. To determine which design variables mostly influence the objective function and the constraints (especially the leak rate constraint), Optform is used to create *Pareto plots*. Two of these plots are shown in Figure 6.11, one for the objective function and one for the leak rate constraint. These Pareto plots show that the value of the objective function is mainly determined by the dimension H_2, all other dimensions have a significantly lower influence. In the case of the leak rate constraint, the dimension H_1 also has a significant impact. This can be explained by the fact that this dimension, representing the corrugation height, will lead to a higher degree of thinning in the corrugations if this dimension increases. Thinning within the corrugations has hardly any influence on the radiation length, since no material is added into the corrugations. Also, the dimensions F_1 and F_2 contribute significantly to the leak rate constraint. Therefore, the four dimensions H_1, H_2, F_1 and F_2 will be the design variables in the remaining steps of the optimization process. The fillet radius R will be set to the maximum value of 6 mm. The two remaining dimensions α and L_1 will be set to the value that gives the most space inside the RF Box for the silicon sensors: 10^o and 10 mm, respectively. Figure 6.12 shows the effect of these three remaining dimensions on the objective function value and constraint g_1. The dimensions L_1 and α have a very small effect, the radius R has a higher effect on the constraint g_1, and has its best value at 6 mm.

6.6.2 RF Foil Design of Experiments

From the screening step of the optimization procedure, four design variables were left to be determined in the remainder of the optimization procedure. A Design of Experiments (DOE) has to reveal the relationship between the design variables and the objective function. A global minimum for this function should be found while satisfying the constraints. A set of 40 designs was created by a Latin Hypercube

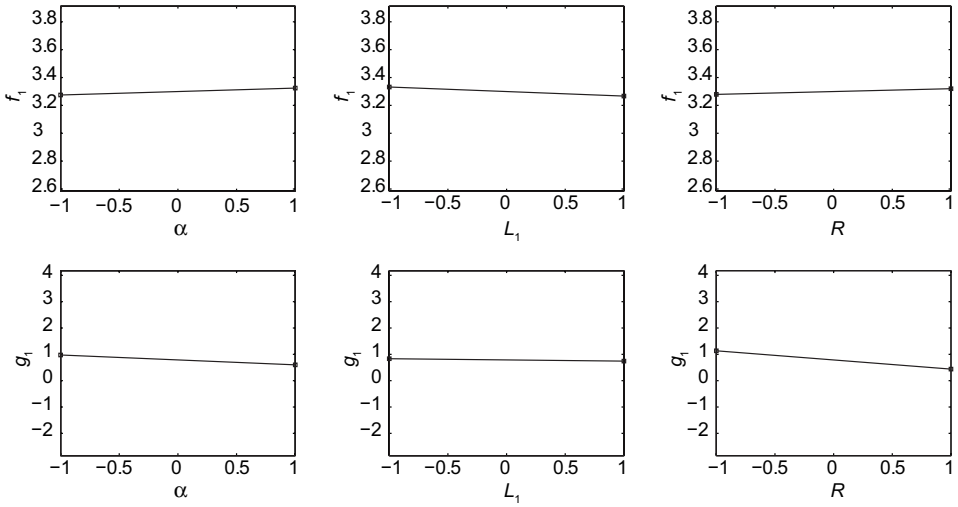

Figure 6.12: Effects of the three remaining dimensions on the objective function value and the leak rate constraint.

Space filling method, the number of designs being ten times the number of design variables.

A summary of the five best designs (i.e. lowest objective function value while satisfying all constraints) is presented in Table 6.4. This table shows the values of the design variable settings, the objective function value (i.e. the radiation length of the corresponding full RF Foil), and the value of the leak rate constraint.

Table 6.4: The five best designs in the DOE step.

H_1	H_2	F_1	F_2	F_{obj}	g_1	g_2	g_3
10.153	59.845	48.656	49.409	**4.746**	-0.012	-0.246	-0.505
10.531	51.538	44.119	45.100	**4.906**	-0.333	-0.327	-0.562
11.135	36.863	20.994	10.216	**4.970**	-0.171	-0.400	-0.571
10.676	43.666	26.208	31.362	**4.995**	-0.355	-0.334	-0.561
11.597	39.892	12.202	34.232	**4.998**	-0.093	-0.443	-0.576

The constraint g_4 is not included in the table, since this value was negative for all 40 DOE points. From all evaluations of the designs within the DOE, there was no positive value found for the constraints g_2 and g_3 if the value for g_1 was negative.

This means that the constraints g_2 and g_3 are never active. So, if the leak rate constraint is satisfied, then the displacement and stress constraint are automatically satisfied. It was already concluded that the constraint g_4 is always satisfied. This means that the first natural frequency is always above 96 Hz, regardless of the design variable settings.

The evaluated designs in terms of the objective functions and the constraint values are fitted to the set of functions available in OptForm. The quality of fit is expressed in the R^2 and R^2_{adj} value and the RMSE value. Table 6.5 summarizes these values for the fitting expressions available in OptForm.

Table 6.5: Quality of fit for the objective function and the leak constraint of the seven fitting functions.

Objective function F_{obj}			
Function type	R^2	R^2_{adj}	RMSE
linear (no interaction)	0.9917	0.9908	0.04971
linear (with interaction)	0.9944	0.9926	0.03763
elliptic	0.9934	0.9917	0.03976
quadratic	0.9966	0.9947	0.03175
Kriging (order 0)	0.6316	0.5666	0.2619
Kriging (order 1)	0.9867	0.9823	0.04975
Kriging (order 2)	0.9890	0.9780	0.4525
Leak rate constraint g_1			
Function type	R^2	R^2_{adj}	RMSE
linear (no interaction)	0.8967	0.8863	0.5154
linear (with interaction)	0.9354	0.9139	0.4484
elliptic	0.9260	0.9075	0.4649
quadratic	0.9453	0.9159	0.4433
Kriging (order 0)	0.6976	0.6443	0.8300
Kriging (order 1)	0.8501	0.8001	0.5844
Kriging (order 2)	0.7449	0.4897	0.7625

From this table, the Kriging fits are in general less accurate than the four RSM fits, especially for the leak rate constraint. The quadratic fit is in both cases (objective and leak rate constraint) the best option. In the case of the Kriging options, the first order Kriging objective fitting function also seems accurate. Figure 6.13 shows the plots with the evaluated and the predicted response; Figure 6.13(a) for the objective function in the case of quadratic fitting, Figure 6.13(b) for the leak

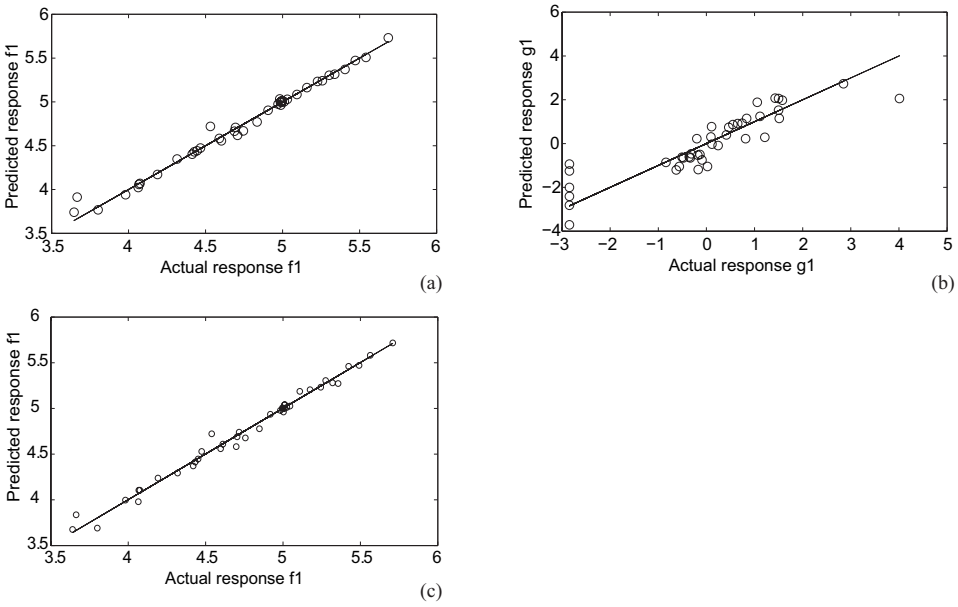

Figure 6.13: Cross validation plots showing the evaluated versus the predicted response; (a): quadratic fit of the objective function, (b): quadratic fit of the leak rate constraint, (c): first order Kriging fit of the objective function.

rate constraint in the case of quadratic fitting and Figure 6.13(c) for the objective function in the case of first order Kriging fitting.

In the case of the quadratic fit function, the responses at each design point are predicted using this function fit, and compared with the actual value as extracted from the FE simulations. In the case of the Kriging function fit in Figure 6.13(c), a predicted response is based on the fitting Kriging function of all design points, except for the point to be predicted.

6.6.3 Optimal RF Foil design

With the fits determined in the previous section, the optimum design can be determined within the limits of the design variables and taking into account the leak rate constraint (as it was concluded that this is the only active constraint). OptForm is able to predict the optimum design using the function fits. Two options are discussed here:

- finding the optimum with a quadratic function fit for both the objective function and the leak rate constraint (case 1);

- finding the optimum with a first order Kriging function fit for the objective function and a quadratic function fit for the leak rate constraint (case 2).

Table 6.6: Optimum designs for cases 1 and 2.

dimension	H_1	H_2	F_1	F_2	F_{obj}
case 1	10.415	64.677	50.000	50.000	4.4960
case 2	10.426	64.650	50.000	50.000	4.4960

Table 6.6 lists the values of the design variables for both optima in cases 1 and 2. In both cases, the value for the objective function in the optimum point is 4.4960, which is the radiation length of the full RF Foil. This value is reached when both dimensions F_1 and F_2 are at their maximum value. As can be seen, both designs are almost the same. The optimal value for H_1 between both cases differs 0.011 mm, this difference is 0.027 mm for the dimension H_2. Evaluating both optima by means of FE analyses shows that in both cases, the value of the leak rate constraint is slightly positive. This constraint value decreases if H_2 decreases, and has a value of -0.036 if $H_2 = 62.0$ mm. The value for the objective function is then 4.699. The fact that the optimum is found when both F_1 and F_2 are at their maximum value gives the impression that even lower values for the objective function would be possible if the maximum values for F_1 and F_2 are increased. Therefore, an extra set of eight designs was evaluated. Within these designs, these two dimensions are set equal to each other. Table 6.7 gives an overview of the evaluated designs with the value for the objective function and the leak rate constraint.

Table 6.7: Extra evaluated designs for F_i exceeding 50 mm, $i = 1, 2$.

DOE#	H_2	F_i	F_{obj}	g_1
1	62.0	50	4.699	-0.036
2	66.0	57.5	4.663	-0.006
3	66.4	61.5	4.703	-0.136
4	70.0	65.0	4.640	0.021
5	68.5	66.0	4.698	-0.142
6	70.2	67.5	4.665	-0.064
7	72.4	70.0	4.633	0.014
8	70.3	70.0	4.695	-0.153

These results imply that the value of the objective function would decrease continuously if the dimensions H_2, F_1 and F_2 increase. That this cannot be true can be seen from the fact that there is at least a minimum amount of material necessary to satisfy the constraints. Since the leak rate constraint is the only active constraint, one could say that the ideal situation is one where the whole RF Foil has the same sheet thickness everywhere in the model. This thickness would just be on the limit of what is acceptable for the leak rate.

The following has been done to propose a design that can be called an optimum:

- within the small region that has been evaluated, the objective function F_{obj} and the leak rate constraint g_1 have been fitted to the two dimensions H_2 and F, where F stands for both flange dimensions F_1 and F_2. Linear fits have been found which show very good accordance with the observed values

$$F_{\text{obj}} = -0.0299H_2 + 0.0124F + 5.93 \qquad (R^2_{\text{adj}} = 0.9854) \tag{6.26}$$

$$g_1 = 0.0810H_2 - 0.0397F - 3.07 \qquad (R^2_{\text{adj}} = 0.9972) \tag{6.27}$$

- if the value of H_2 is set to a maximum of 72.5 mm (since a value of 72.4 mm was the maximum value in the re-evaluation), then from the leak rate constraint it follows that the value for F is 70.555 mm, in case this constraint is set to zero.

- The value for the objective function is calculated according to Equation (6.26). This leads to a value of the radiation length of the optimized RF Foil of 4.6%. This value is considerably lower than the radiation length of 8.2% which was obtained from the current RF Foil design.

- The optimal design as proposed here was finally evaluated by an FE analysis. The result of this analysis is that the value for the objective function is 4.64 and the value for the leak rate constraint -0.011.

Figure 6.14 shows the sheet thickness of the deformed part. In the FE model, the outer edge of the sheet (2 edges) were pinned, the other two edges were constrained by symmetry conditions. The resulting values of the die dimensions are also summarized in Figure 6.14. The minimum sheet thickness is 0.127 mm, the maximum thickness is 0.205 mm and the average thickness is 0.166 mm. The analysis stopped, as all other analyses concerning the optimization simulations, at the maximum deformation time of 2000 seconds. At that point in time, full contact was achieved between the sheet and the die in all cases. A final remark must be made. Increasing the values for H_2, F_1 and F_2 more and more would lead to an ever decreasing value for the radiation length. The limit is then where the sheet thickness combined with the void volume fraction in the material is just sufficient to satisfy the leak rate constraint, i.e. $g_1 = 0$. The program which has been used to calculate the radiation length and the leak rate has been used to determine the

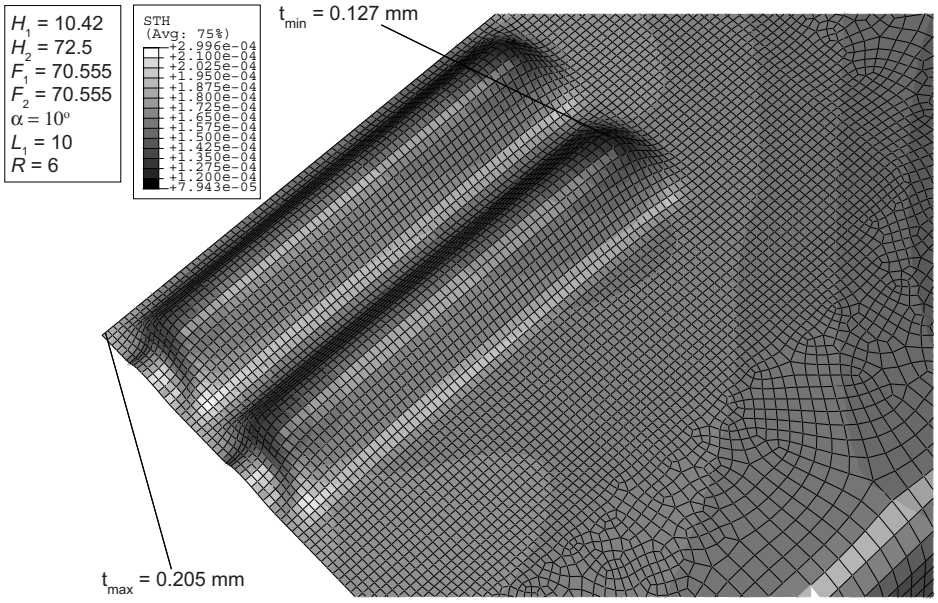

Figure 6.14: Resulting sheet thickness distribution after superplastic forming of the optimized design. The values in the table of dimensions are in mm.

minimum evenly distributed thickness (and accompanying void volume fraction, assuming an average stress situation which is uniaxial). This calculation resulted in a sheet thickness of 0.158 mm. The radiation length in this case is 4.1% X_0, which is 12% lower than the radiation length of the optimized model. It must be noted, however, that this value of 4.1% is a theoretical minimum.

6.7 Summary and conclusions

The geometry of the RF Foil has been parameterized such that a set of seven dimensions determines the shape to be optimized. Three of these dimensions (H_2, F_1 and F_2) do not appear in the final product. The function of these dimensions is to achieve more thinning in the sheet and a more even distribution of the thickness of the foil. These three dimensions, together with the corrugation height, mainly determine the value of the objective function and of the leak rate constraint.

The radiation length of the current RF Foil is 8.2% X_0, this has been based on calculations where the average resulting sheet thickness is 0.25 mm. The optimized foil has a radiation length of 4.6% X_0, which is a decrease with respect to the current design of 43%. Most of the decrease in radiation length comes from the reduction

in average sheet thickness, which was reduced from 0.25 to 0.166 mm.

From the total set of constraints (leak rate, wake field suppression, mechanical), the leak rate constraint g_1 is the only active constraint. If this constraint is satisfied, then all other constraints are satisfied. The wake field suppression was already satisfied by limiting the corrugation height H_1.

Increasing the dimensions H_2, F_1 and F_2 will lead to a decrease in the radiation length. There is, of course, a limit which is an ideal situation if the sheet were to have a uniformly distributed thickness. The lower limit on the radiation length is in this case 4.1% X_0. The sheet thickness should then be 0.158 mm everywhere in the model. A radiation length of 4.6% X_0 can be called an excellent solution, since this is not much higher than the theoretical minimum (13% higher).

7. Conclusions and recommendations

This chapter describes the conclusions and recommendations of this research. The goal of the project, i.e. reducing the radiation length of the current RF Foil, has been achieved. Three major stages to achieve this goal are distinguished: material experiments, material modeling and geometric optimization.

Material experiments Two types of experiments have been performed: tensile experiments and bulge experiments. The tensile experiments revealed the uniaxial properties, while the bulge experiments revealed the plane stress properties, the leak rate behavior and the friction between the sheet and the die.

Tensile experiments were performed where two parameters could be influenced: the temperature and the cross head velocity. The temperature was a continuous variable, the optimal temperature for superplasticity was found to be 520 °C. At this temperature, the maximum elongation was reached at all tested drawing velocities. This drawing velocity was however not a continuous variable. From the velocities at which the specimens were tested, an optimal plastic strain rate of $8.3{\cdot}10^{-4}$ s^{-1} was finally found. This would correspond to a drawing velocity of 1.4 mm/min.

The bulge experiments were performed by using a dedicated design for this purpose. The results of these experiments in terms of bulge height were highly reproducible, due to the program written in LabVIEW to control the temperature and separate pressures within the experimental setup. During the bulge experiments, it was possible to apply a hydrostatic pressure (backpressure) during the forming process. This backpressure had a beneficial effect on the maximum plastic strain that could be reached and on the leak rate.

Material modeling The uniaxial tests could not be performed with the application of a backpressure, and at a drawing velocity corresponding to the optimal superplastic strain rate for ALNOVI-1. It was, however, possible to develop a material model which describes the mechanical behavior accurately enough. Since one of the most important features of the model is the leak rate prediction, and since

this leak rate shows a relatively high variance, further refinement would not increase the predictability of the leak rate. Therefore, the developed material model is considered accurate enough to predict the mechanical behavior of ALNOVI-1.

This does not mean that the mechanical behavior is predicted in the most efficient way. Because of the high strain rate sensitivity, the material behaves somewhere between a solid and a fluid. It was chosen here to use a material model based on solid mechanics, which led to satisfactory results.

Geometrical optimization The current geometry of the RF Foil has been parameterized and optimized with respect to radiation length. The optimized procedure revealed that the leak rate constraint was the only active constraint. This led to a design with an average thickness of 0.166 mm. This is well below the average thickness of the current RF Foil, which means that the optimization procedure was successful. This is not far above the theoretical value of the minimum average thickness (with respect to the leak rate) of 0.158 mm.

The goal of this research was to reduce the radiation length of the RF Foil, while making it possible to predict the leak rate of a deformed sheet by numerical analysis. This goal was achieved by developing a material model which describes the mechanical behavior including a leak rate prediction in an accurate way. This material model was used to employ an optimization strategy in order to minimize the radiation length of the current RF Foil. This radiation length decreased from 8.2% X_0 to 4.6% X_0, the leak rate constraint was met in this case. This is a considerable improvement with respect to the current RF Foil.

Other topological solutions may be possible which may lead to even lower radiation lengths. If the design will cover most of the view angle as seen from the interaction point, optimization can be reached in two ways:

- trying to find a procedure which will lead to even lower wall thicknesses without introducing leak. In the case of Superplastic Forming, and as mentioned earlier, higher backpressures may be applied, leading to lower void volume fractions at the same equivalent plastic strain values;

- designing a shape such that the average number of crossings through the walls will be reduced. With the current design, a particle may travel many times through the material until a detector is hit. This is especially the case for particles traveling almost parallel to the beam line. The radiation length may then be decreased by developing a design where these particles will hit fewer walls before hitting a detector.

Recommendations for future work Four recommendations are given here for future research, in order to investigate whether a further improvement of the radiation length is possible.

1. A recommendation with respect to the bulge experiments concerns the following. The setup of the bulge experiments was designed to withstand a maximum hydrostatic pressure of 30 bar. Experiments were performed at three different backpressure values: 14, 22 and 30 bar. Because the difference in results (increase in maximum bulge height and thus plastic strain) was considerable between 22 and 30 bar backpressure, it would be interesting to know what the effect on the material would be if even higher backpressure values were to be used.

2. A topological optimization of the RF Foil instead of only a geometric optimization procedure may reduce the radiation length even further. To reduce the average number of crossings through the wall of the RF Foil, it can be imagined that two (or more) detectors are positioned in one corrugation. The cross-sectional view of the RF Foil can possibly look like what is presented in Figure 7.1(a). In the most extreme case, half of the detectors is positioned within a corrugation, as is presented in Figure 7.1(b).

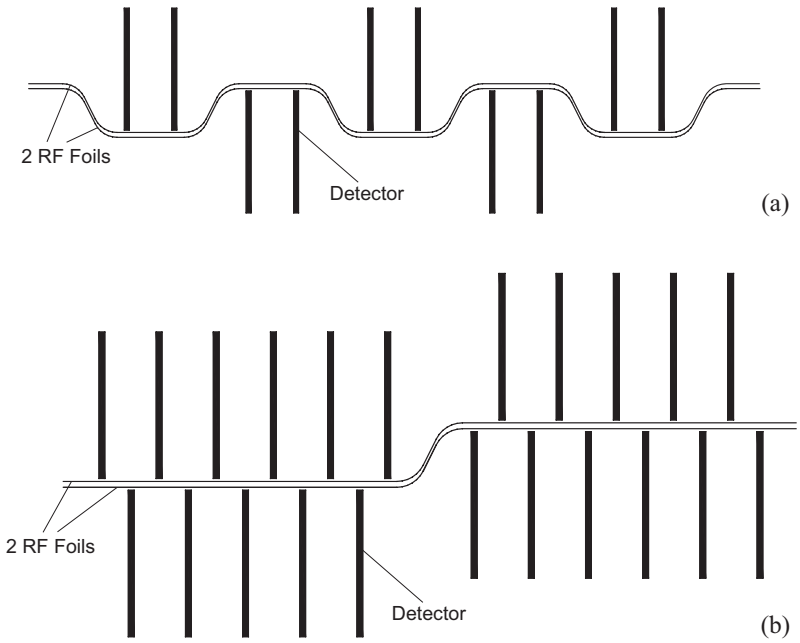

Figure 7.1: Topological solutions for further decrease of the radiation length: (a) two detectors per corrugation; (b) half of the detectors in each 'corrugation'.

With this topology, the maximum number of crossings will be decreased significantly. With this geometry, however, the elastic stiffness decreases with respect to the current geometry, because the stiffening corrugations have disappeared. But since the constraint concerning the elastic stiffness was never active, it is worthwhile taking a look at this solution.

3. This research only focused on the manufacturing of the RF Foil by means of Superplastic Forming. This forming process is an attractive process, because the number of products to be made is very low (2 pieces). Also, the plastic strains which can be reached are very high and so a large amount of thinning can be reached. It may be possible to produce these foils in a different manner, by a new method like incremental forming. Especially the latter possibility can be investigated in the future as an alternative manufacturing method.

4. A problem with severe thinning in superplastic materials is the growth and coalescence of voids, and therefore gas leak. The material leaks before it fails in terms of fracture. The question is whether leaks can be mended, for instance by filling the voids with a secondary material. It is known that the metal gallium can diffuse to voids under certain conditions [80].

A. Control scheme of the bulge experiments

A software program was written in LabVIEW to control an entire bulge test. This appendix describes the procedure followed by this piece of software, which was written at Nikhef. A sheet was positioned inside the experimental setup, on top of the Bottom Container. After positioning this setup in the oven and closing the oven door, the software program was started. Below is a description of the steps which were followed. The abbreviations V1 to V7 correspond with the labels depicted in Figure 3.9.

- When the program starts, the temperature will be constantly monitored while the setup heats up. The temperature at which the sheet should be deformed is 520 °C. If the thermocouple readout shows a value of 420 °C, the heater band injects extra power to the setup to accelerate the temperature rise. This heater band is controlled by a PID, which takes care that the target temperature will not be exceeded. During this step, V6 ad V7 are opened while all other valves are closed. With V6 open, there will be no pressure difference between the Top and Bottom Container. With V7 open, the pressure in the Top and Bottom Container is the same as the atmospheric pressure. If the target temperature has been reached, a waiting time of five minutes is applied to be sure that the whole setup has reached this target temperature.

- The Pressure Bag will be filled with gas until a pressure is reached which is 10 bar above the entered backpressure value. This is done by opening and closing V5. In this way, the aluminum sheet will be clamped on its outer boundary in the stainless steel setup.

- A backpressure will be applied to the Top and Bottom Container by opening V1 and V3. At the beginning of this step, V7 will be closed. To ensure that no pressure difference will develop between the Top and Bottom Container, V6 stays open.

- The forming pressure is applied by closing V1 and V6 at the beginning of this step and by keeping V3 open. Since the forming pressure has to be

applied very slowly, V3 and V4 work together in order to approximate as closely as possible the target pressure in time. During the forming process, the volume of the Top Container decreases, because the sheet is deformed upwards. Because the backpressure should not change, V2 is opened to relieve any overpressure.

- If the time limit has been reached, the forming pressure will be released by closing all valves and then opening V6. This equalizes the pressure between the Top and Bottom Container. This will temporarily increase the backpressure a small amount, but this will not affect the outcome of the experiment, since this time span is very small, and there is no forming pressure left. In this step, the band heater will be shut off.

- With V6 opened, the backpressure will be released two seconds later, by opening V7. Once atmospheric pressure has been reached, the test is finished.

- A leak detection module has been built inside the program. If, during the forming stage, the sheet should fail by local fracture, then it will become more and more difficult to maintain the target forming pressure, since the hole actually takes over the function of an opened valve V6. The backpressure will increase, so V2 is opened constantly. V3 has to stay opened in order to try to maintain the pressure difference. These two valves are adjusted such that a hole in the sheet leads to a non-reversible pressure difference drop, this drop will be detected by the program. The software will then stop the test by closing all valves, except V6 and V7.

The pressure in the Pressure Bag has to be released manually after the program stops running. The furnace can then be opened and the formed sheet can be taken out of the Top Container by cooling the sheet with pressurized air. The sheet will detach from the Top Container since the shrinkage of the sheet is higher due to the higher thermal expansion coefficient of aluminum with respect to stainless steel.
Besides this process, some safety has also been built into the program. If the pressure in one of the pressure vessels exceeds a predefined limit value, then the experiment is stopped immediately, by opening the valves V6 and V7, and closing all other valves. This will release all the gas which is trapped at that moment in the experiment. In the case of a computer crash or a power failure, all valves will immediately return to their default, closed, position. Pressures will then not increase anymore; they have to be released manually.

B. First and second derivative of the universal superplastic curve

The material parameters necessary to describe the initial yield stress as a function of the plastic strain rate (a, b, c and d) are fitted into the universal superplastic curve according to

$$\log \sigma_{y0} = \frac{1}{a + b \cdot \exp(c \log \dot{\varepsilon})} + d \tag{B.1}$$

The second derivative of this relationship $\partial^2 \log \sigma_{y0} / \partial \log \dot{\varepsilon}^2$ is necessary to determine the strain rate at which optimal superplasticity is reached, This must be equal to zero in that case. The slope $\partial \log \sigma_{y0} / \partial \log \dot{\varepsilon}$, which is the strain rate sensitivity m is then at its maximum. For written convenience, set s equal to $\log \sigma_{y0}$ and e equal to $\log \dot{\varepsilon}$. Then

$$s = \frac{1}{a + b \cdot \exp(ce)} + d \tag{B.2}$$

Then

$$\frac{\partial s}{\partial e} = \frac{-bc \cdot \exp(ce)}{[a + b \cdot \exp(ce)]^2} \tag{B.3}$$

To calculate $\partial^2 s / \partial e^2$, use the formula

$$\frac{\partial (f(x)/g(x))}{\partial x} = -\frac{f(x)}{g(x)^2} \cdot \frac{\partial g(x)}{\partial x} + \frac{\partial f(x)}{\partial x} \cdot \frac{1}{g(x)} \tag{B.4}$$

Then

$$\frac{\partial^2 s}{\partial e^2} = \frac{bc \cdot \exp(ce)}{[a + b \cdot \exp(ce)]^4} \cdot 2[a + b \cdot \exp(ce)] \cdot bc \cdot \exp(ce) - \frac{bc^2 \cdot \exp(ce)}{a + b \cdot \exp(ce)^2} \tag{B.5}$$

$$= \frac{2[bc \cdot \exp(ce)]^2}{[a + b \cdot \exp()ce]^3} - \frac{bc^2 \cdot \exp(ce)}{[a + b \cdot \exp(ce)]^2} \tag{B.6}$$

This must be equal to zero, giving

$$\frac{2b \cdot \exp(ce)}{a + b \cdot \exp(ce)} = 1 \tag{B.7}$$

Working out this equation eventually gives for $\log \dot{\varepsilon}$:

$$\log \dot{\varepsilon} = \frac{1}{c} \ln(\frac{a}{b}) \tag{B.8}$$

By substituting this value in the equation for the first derivative, it is found that the strain rate sensitivity m at this point is

$$m_{\text{opt}} = \frac{-c}{4a} \tag{B.9}$$

C. Example of an input file

Below, an example of an input file is shown, concerning a free bulge simulation with an application of 30 bar backpressure during forming.

1. Heading	`*Heading`
	`** Job name:  press6e4BP30 Model name:  FreeBulge`
	`*Preprint, echo=NO, model=NO, history=NO, contact=NO`

2. Sheet definition	`** PARTS`
	`*Part, name=Sheetpart`
	`*Node`
	`1, -0.000299588864, 1.57007871e-05, 0.`
	`...`
	`213, -0.0439550392, 0.00230358588, 0.`
	`*Element, type=M3D3`
	`1, 1, 2, 3`
	`*Element, type=M3D4R`
	` 2, 2, 1, 12, 89`
	`...`
	`106, 191, 190, 7, 6`

3. Material	`** MATERIALS`
	`*Material, name=ALNOVI-1`
	`*Depvar`
	`15,`
	`*User Material, constants=0`
	`*User Defined Field`

4. Section definition	```** Section: ALNOVIsheet *Membrane Section, elset=_PickedSet4, material=ALNOVI-1 0.0008, 5 *Hourglass Stiffness 1.0e6,,,1.0e-1 *End Part *Initial Conditions, type=field, variable=1```
5. Die definition	```*Surface, type=REVOLUTION, name=DieInner START, 0., 0. LINE, 0.027, 0. CIRCL, 0.035, 0.008, 0.027, 0.008 LINE, 0.035, 0.065 CIRCL, 0.04, 0.07, 0.04, 0.065 LINE, 0.0455, 0.07 *Rigid Body, ref node=Die-1-RefPt_, analytical surface=DieInner```
6. Contact definition	```*Surface, type=ELEMENT, name=PSheetContact _PSheetContact_SPOS, SPOS _PSheetContact_SNEG, SNEG ** INTERACTION PROPERTIES *Surface Interaction, name=Sheet2Die *Friction 0.15, ** INTERACTIONS ** Interaction: DiePsheet *Contact Pair, interaction=Sheet2Die PSheetContact, Die-1.DieInner```
7. Boundary conditions	```** BOUNDARY CONDITIONS ** Name: FixDie Type: Symmetry/Antisymmetry/Encastre *Boundary DieRfPt, ENCASTRE ** Name: PMidBC Type: Displacement/Rotation *Boundary PSheetMidPt, 1, 1 PSheetMidPt, 3, 3 PSheetMidPt, 4, 4 PSheetMidPt, 5, 5 PSheetMidPt, 6, 6 ** Name: PSheetOuterEdge Type: Symmetry/Antisymmetry/Encastre *Boundary POuterEdge, PINNED ** Name: PSymmOBLEdge Type: Displacement/Rotation *Boundary```

	PSymmOBLEdge, 3, 3 PSymmOBLEdge, 4, 4 PSymmOBLEdge, 5, 5 ** Name: PSymmZ Type: Symmetry/Antisymmetry/Encastre *Boundary PSymmZEdge, ZSYMM
8. Amplitude definition	*Amplitude, name=hydr 0., 1.0, 3600., 1.0 *Amplitude, name=P6E4 0., 0., 50., 0.095, 100., 0.165, 150., 0.245 200., 0.35, 250., 0.45, 300., 0.565, 350., 0.705 400., 0.835, 450., 0.985, 500., 1.13, 550., 1.27 600., 1.395, 650., 1.51, 700., 1.605, 750., 1.665 800., 1.71, 825., 1.725, 850., 1.73, 875., 1.725 900., 1.715, 950., 1.685, 1000., 1.625, 1050., 1.55 1100., 1.455, 1150., 1.35, 1200., 1.25, 1300., 1.055 1400., 0.875, 1500., 0.745, 1600., 0.665, 1650., 0.64 1700., 0.585, 1800., 0.51, 2000., 0.435, 2400., 0.365 3000., 0.32, 3600., 0.3
9. Static step	** STEP: Forming step *Step, name="Forming step", nlgeom=YES, inc=2000 *Static 1.0, 3600., 1e-04, 10. *Field, variable=1, amplitude=hydr PSheetSurf, 30.0
10. Loads	** LOADS *Initial Conditions, type=stress, unbalanced stress=step PSheetSurf,5.0e3,5.0e3 ** Name: SheetLoad Type: Pressure *Dsload, amplitude=P6E4 PSheetLoad, P, 100000.
11. Output requests	*Output, field *Node Output U, *Element Output, elset=PSheetSurf, directions=YES S, STH, SDV *Output, history *Element Output, elset=PSheetMidElmt STH, SDV *Node Output, nset=PSheetMidPt U2, *EL PRINT, Elset=PSheetSurf, Frequency=20000 SDV9

1. Model header, including job name and model name.

2. Definition of the sheet geometry in terms of 213 nodes, 106 four-noded quadrilateral, reduced integration, membrane elements and one three-noded triangular membrane element.

3. Material definition, where the user defined material ALNOVI-1 is called. There are 15 state variables defined, the user defined field is meant to define a field where the backpressure can be stored.

4. Section definition: a 0.8 mm thin membrane section with hourglass stiffness control. The initial conditions are the backpressure values on all the elements.

5. The die is an analytical rigid, which is defined by a set of lines and circles which are revolved to obtain a 3-dimensional geometry. A reference point is defined to which boundary conditions can be applied later.

6. Contact is established by defining contact surfaces. A friction coefficient of 0.15 has been applied.

7. The die is fixed in all displacements and rotations. The outer edge of the sheet has been pinned (fixed in all translations). One of the side edges of the sheet has symmetry boundary conditions with respect to the global Z axis. The other side on the edge has symmetry boundary conditions with respect to an oblique, user defined, coordinate system.

8. Two amplitudes must be defined. One is called *hydr* and is a multiplication factor for the hydrostatic pressure. The other amplitude, called *P6E4*, defines the forming pressure as a function of time.

9. A static step has been defined, with an initial increment size of 1 second, a maximum increment size of 10 seconds and a minimum increment size of 1.0E-4 seconds. The total forming time is 3600 seconds, the backpressure has been set to 30 bar.

10. Before the forming load is applied, an in-plane stress is necessary to prevent initial ill-conditioning due to the fact that membrane elements have been used. A pressure load of 100000 Pa (= 1 bar), multiplied with the forming pressure amplitude, has been applied.

11. The field output is in terms of the displacements, the stress, the sheet thickness and the state variables. The requested history output concerns the displacement of the midpoint of the sheet as a function of time. State variable 9 (the void volume fraction) has been written, only in the last increment, for all elements to the results file.

Acknowledgments

This chapter provides the only opportunity for me in this thesis to violate some rules that apply to writing scientific reports. Whereas in scientific writing it is not allowed to use personal pronouns like 'I', 'you', 'he' or 'she', in these three pages, I will almost only use them. Also, storytelling is not considered to be scientific, for instance 'and then ... happened'. However, I am going to tell you a story now.

It all started in the spring of 2004. Then the idea of starting a PhD research project came up during a so-called POP meeting (Persoonlijk OntwikkelingsProfiel or Personal Development Profile), and it was suggested by the Nikhef HR manager Teus van Egdom. He advised me to discuss the idea with Frank Linde as coordinator of the ATLAS project in order to get his opinion and his suggestions for subjects to study. He supported the idea, and later that year, when Frank became the director of Nikhef, he gave me the freedom to choose a subject myself as long as there was a relation with one of the running projects at Nikhef at the time. In talking to several people, around five topics were suggested. The idea of simulating the deformation process of the RF Foil and trying to understand and predict the leak rate of a formed RF Foil came from Rob Klöpping and this became the basis of my research project. Frank agreed and on the first day of his directorship he traveled to the University of Twente in Enschede for a meeting with professor Han Huétink. Han readily agreed to be my supervisor of this PhD research and he appointed a very motivated young staff member of his faculty to be my daily tutor and assistant supervisor, Timo Meinders. Teus, Frank and Rob, thank you very much for giving me the opportunity to start this PhD research. Han and Timo, thank you very much for all your support and expertise during the five years that I spent on the thesis. It has always been a great pleasure to visit you and the university. I particularly enjoyed your 'Twente' sense of humor and the relaxed atmosphere that goes along with it.

Since Enschede is too far away to work on a daily basis, the home base for my work remained Amsterdam. Bob van Eijk was the supervisor at Nikhef and I thank you for all the good tips you provided when I needed them. It was also at Nikhef where the majority of the mechanical experiments were done. The bulge experiments consumed a major part of the five-year period and it was very inspiring

to experience that our own design of the bulge test setup worked perfectly fine right from the beginning, without any major problems. I said 'our design' on purpose because I could not have realized it without the help of Berend Munneke, who helped with his expertise and who really put a lot of effort in the design. He not only helped with designing but he was also of great help in the experiments themselves, where he spent many hours in assisting and never seemed to be tired to press another series of bulges. Berend, thank you very much for your enthusiasm, contribution and support.

With respect to the bulge experiments, a few more people must be mentioned. The most difficult part of the experimental setup was the manufacturing of the stainless steel pressure vessels which had to be placed inside the furnace. Joop Rövekamp did the major part of the manufacturing and I thank you very much for your time and patience and for thinking along with regard to certain details of the design. Martijn Woldman, a student of Twente University got interested in Nikhef and my project in particular. He saved me a lot of time by assisting in the experiments. Thank you Martijn for your help. An important part of the experiments was measuring the leak tightness of the bulges and in order to be able to do that correctly, they had to be cleaned thoroughly when they came out of the experiment. And with thoroughly, I really mean thoroughly. With the great help and experience of Peter Thobe we managed to have all the molecules that had to leave the bulge surface, to leave indeed. Thank you Peter for helping and sharing your experience.

But before even the bulge experiments could start, the results of the tensile experiments had to be known. These experiments were done at the University of Groningen where I got the opportunity to perform the tests at the faculty of Jef de Hosson. He was willing to let me do the tensile tests in one of his labs and he asked two people to help me with the start up: Antony Kazantzis and Zhenguo Chen. As real scientists, they did not stop there but also thought along in order to carry out the experiments in the best way. Jef, Antony and Zhenguo, thank you very much for offering me your facilities, knowledge and help. And finally, of course, at the very basis of all material experiments, the material itself with which the tests are performed is essential. I therefore like to thank Kumi Kawase of the company Furukawa Sky Aluminium in Japan for sending me a considerable amount of ALNOVI-1 free of charge.

Then the writing of the PhD thesis itself. This is a constant process of adding, removing and changing text and figures. The comments and suggestions made by the reading committee proved to be very helpful and led to the draft thesis. Besides Han and Timo I should thank Jan-Harmen Wiebenga for the critical review on the chapters I wrote. I would also like to thank Semih Perdahcıoğlu for reading Chapter 4, and Marcel Merk for the remarks on the physics side of the thesis (Chapter 1). Finally, thanks to Vivien Cook for proofreading all chapters (except this one!) and reviewing the thesis on English spelling and grammar. The draft thesis could then

be turned into the final thesis, of which this book is proof. It was finalized thanks to some last, extra remarks of the examiners. Besides the people I already thanked for all their help, I would also like to thank Richard Wood from Swansea University in Wales and Remko Akkerman in this context, for their willingness to take place in the examination committee.

And now it is time to change to Dutch.
Behalve de inhoudelijke en administratieve hulp, is er ook heel veel steun en interesse geweest van familie en vrienden. In die twee termen zit overigens een grote overlap. Om de familie en een groot deel van de vriendenkring te noemen, maak ik gebruik van de term 'grootfamilie' waarin iedereen zit die zich aangesproken voelt door de achternaam Snippe, van der Veen, Moens, Hammecher, Hooman, Besseling, Berendsen, Streppel en Ribeiro. Allen hebben zeer grote interesse getoond in hetgeen ik deed, en een veelgehoorde vraag was of ik het nog een keer wilde uitleggen. Dat deed ik graag.

Maar ik wil er natuurlijk een aantal mensen uitlichten. Ten eerste wil ik mijn zus Solveg en haar vriend René bedanken voor de gastvrijheid en gezelligheid die ik genoten heb in de tijd dat ik materiaalexperimenten deed op de universiteit van Groningen. Natuurlijk hebben we elkaar in die vijf jaar veel vaker gezien, maar jullie huis was een geweldige plek om te verblijven in die periodes.

Vele anderen hielpen bij het verzetten van de zinnen door nachtelijke drink- en spelletjessessies op geregelde tijden (Tineke en Willem, Bas en Carlos). Zinnen werden ook verzet door het spelen van muziek, dit heeft een extra impuls gekregen toen ik als basgitarist werd opgenomen in de band die, tijdens het ter perse gaan van dit proefschrift, nog steeds naamloos door het leven gaat.

Lest best Vier mensen wil ik graag onder dit kopje scharen, twee daarvan zijn al eerder genoemd. Aangezien zij naast alle hulp en interesse de zware taak van paranimf op zich hebben willen nemen, mogen ze nog een keer genoemd: Berend Munneke en Carlos Ribeiro, dank jullie wel voor het willen vervullen van deze taak! Eerder heb ik al de mensen genoemd zonder wie ik nooit aan een promotie had kunnen werken, maar er missen er nog twee: mijn vriendin Dorien en onze zoon Jasper. Dankzij hun begrip en medewerking heb ik de vele extra uren die ik aan mijn promotie heb moeten besteden ook zonder probleem kunnen besteden. Ik heb van hen veel interesse en steun mogen ervaren en Dorien heeft door de jaren heen ook veel geholpen met het corrigeren van mijn teksten in het Engels en is mede daardoor ook aardig op de hoogte van de hoofdlijnen van mijn onderzoek. Allebei superveel bedankt en een dikke kus!

Bibliography

[1] J. Arora. *Introduction to Optimum Design*. Elsevier Academic Press, 2nd edition, 2004.

[2] M. Ashby and R. Verrall. Diffusion-accommodated flow and superplasticity. *Acta Metallurgica*, 21:149–163, 1973.

[3] D. Bae and A. Ghosh. Grain size and temperature dependence of superplastic deformation in an Al-Mg alloy under isostructural condition. *Acta Materialia*, 48:1207–1228, 2000.

[4] D. Bae and A. Ghosh. Cavity growth during superplastic flow in an Al-Mg alloy: I. Experimental study. *Acta Materialia*, 50:993–1009, 2002.

[5] D. Bae and A. Ghosh. Cavity growth in a superplastic Al-Mg alloy: II. An improved plasticity based model. *Acta Materialia*, 50:1011–29, 2002.

[6] N. v. Bakel. *The silicon vertex detector for LHCb: interaction with the LHC beams and the design of a radiation hard front-end chip*. PhD thesis, Vrije Universiteit Amsterdam, 2004.

[7] N. v. Bakel, J. v. d. Brand, and M. Ferro-Luzzi. A first study of wake fields in the LHCb vertex detector. Technical report, NIKHEF, 1999. LHCb note 99-041/VELO.

[8] N. v. Bakel, J. v. d. Brand, and M. Ferro-Luzzi. Wake fields in the LHCb vertex detector: alternative designs for the wake field suppressor. Technical report, VU Amsterdam, 1999. lhcb-99-044.

[9] F. Barlat, J. Brem, J. Yoon, K. Chung, D. R.E., D. Lege, S.-H. Pourboghrat, and E. Choi. Plane stress yield function for aluminum alloy sheets - part 1: theory. *International Journal of Plasticity*, 19:1297–1319, 2003.

[10] J. Bonet, A. Gil, R. Wood, R. Said, and R. Curtis. Simulating superplastic forming. *Computer Methods in Applied Mechanics and Engineering*, 195:6580–603, 2006.

[11] M. Bonte. *Optimisation Strategies for Metal Forming Processes*. PhD thesis, Twente University, 2007.

[12] A. v. d. Boogaard. *Thermally Enhanced Forming of Aluminium Sheets: Modelling and Experiments*. PhD thesis, Twente University, 2002.

[13] L. Carrino, G. Giuliano, and N. Ucciardello. Analysis of void growth in superplastic materials. *Journal of Materials Processing Technology*, 155:1273–1279, 2004.

[14] CERN. LHCb VeLo Technical Design Report. Technical Report 2001-011, CERN, 2001.

[15] N. Chandra. Constitutive behavior of superplastic materials. *Intl. Journal of Non-Linear Mechanics*, 37:461–484, 2002.

[16] Y. Chen, K. Kibble, R. Hall, and X. Huang. Numerical analysis of superplastic blow forming of Ti-6Al-4V alloys. *Materials and Design*, 22:679–685, 2001.

[17] Z. Chen and T. P.F. A study of post-form static and fatigue properties of superplastic 7475-SPF and 5083-SPF aluminium alloys. *Journal of Materials Processing Technology*, 148:204–219, 2004.

[18] Z. Chen and P. Thomson. Friction against superplastic aluminium alloys. *Wear*, 201:227–232, 1996.

[19] A. Chezan and J. De Hosson. Superplastic behavior of coarse-grained aluminum alloys. *Materials Science and Engineering A*, 410-411:120–123, 2005.

[20] A. Chokshi and A. Mukherjee. The influence of hydrostatic pressure on grain boundary sliding in superplasticity: implications for cavitation. *Materials Science and Engineering A*, 171:47–54, 1993.

[21] R. Cleveland, A. Ghosh, and J. Bradley. Comparison of superplastic behavior in two 5083 aluminum alloys. *Materials Science and Engineering A*, 351:228–236, 2003.

[22] G. Cornfield and R. Johnson. The forming of superplastic sheet metal. *International Journal of Mechanical Sciences*, 12:479–490, 1970.

[23] T. Courtney. *Mechanical Behavior of Materials*. Mc Graw-Hill, 1990.

[24] F. Dunne and N. Petrinic. *Introduction to Computational Plasticity*. OXFORD University Press, 2005.

[25] Furukawa Sky Aluminium Ltd. Superplastic 5083 aluminium alloy sheet ALNOVI-1 was approved by airbus. Furukawa Review 26, 2004.

[26] F. Giordano, A. Natale, and M. Calvagni. Numerical Simulation of the Super Plastic Forming Process of the EFA - 2000 Under Carriage Door. Technical Report 2001-117, Alenia Aerospazio, 2001.

[27] D. Groom et al. Particle physics booklet. Springer, Particle Data Group, 2000.

[28] J. Hedworth and M. Stowell. The Measurement of Strain-Rate Sensitivity in Superplastic Alloys. *Journal of Materials Science*, 6:1061–1069, 1971.

[29] R. Hierck. *Optimisation of the LHCb detector*. PhD thesis, Vrije Universiteit Amsterdam, 2003.

[30] R. Hino, A. Sasaki, F. Yoshida, and V. Totopov. A new algorithm for reduction of number of press-forming stages in forging processes using numerical optimization and fe simulation. *International Journal of Mechanical Sciences*, 50:974–983, 2008.

[31] M. Hojjati, M. Zoorabadi, and S. Hosseinipour. Optimization of superplastic hydroforming process of aluminium alloy 5083. *Journal of Materials Processing Technology*, 205:482–488, 2008.

[32] W. Hosford. Yield locus of randomly oriented fcc metals according to the Bishop-Hill theory. *Metallurgical Transactions*, 4:1416–1417, 1973.

[33] W. Hosford. Comments on anisotropic yield criteria. *International Journal of Mechanical Sciences*, 27:423–427, 1985.

[34] J. Huétink et al. *Mechanics of Forming Processes*. Graduate School Engineering Mechanics, 2003.

[35] J. Huétink and T. Meinders. *Solid Mechanics II: Plasticity*. Universiteit-Twente, 2005.

[36] M. Jain, M. Chaturvedi, N. Richards, and N. Goel. Strain rate sensitivity effects with forming characteristics of superplastic Ti6Al4V. *Materials Science and Engineering A*, 138(2):205–211, 1991.

[37] O. Kaibyshev. Fundamental aspects of superplastic deformation. *Materials Science and Engineering A*, 324:96–102, 2002.

[38] F. v. Keulen, R. Haftka, and N. Kim. Review of options for structural design sensitivity analysis. part 1: Linear systems. *Computer Methods in Applies Mechanics and Engineering*, 194:3213–3243, 2005.

[39] M. Khaleel, H. Zbib, and E. Nyberg. Constitutive modeling of deformation and damage in superplastic materials. *Intl. Journal of Plasticity*, 17:277–296, 2001.

[40] M. Kraan. *http://www.nikhef.nl/pub/departments/mt/projects/lhcb-vertex/*. Nikhef, 2010.

[41] G. Krallics and J. Lenard. An examination of the accumulative roll-bonding process. *Journal of Materials Processing Technology*, 152(2):154–161, 2004.

[42] M. Lagos and H. Luque. Two-phase theory for the superplastic flow. *International Journal of Plasticity*, 17:369–386, 2001.

[43] T. Langdon. The mechanical properties of superplastic material. *Metallurgical and Materials Transactions A*, 13(5):689–701, 1982.

[44] T. Langdon. Creep at low stresses: an evaluation of diffusion creep and Harper-Dorn creep as viable creep mechanisms. *Metallurgical and Materials Transactions A*, 33:249–259, 2002.

[45] D. Lassance, F. Scheyvaerts, and T. Pardoen. Growth and coalescence of penny-shaped voids in metallic alloys. *Engineering Fracture Mechanics*, 73:1009–1034, 2006.

[46] H. Lee, J. Yoon, C. Park, Y. Ko, D. Shin, and C. Lee. A study on diffusion bonding of superplastic Ti-6Al-4V ELI grade. *Journal of Materials Processing Technology*, 187-188:526–529, 2007.

[47] S. Lee, J. Yoon, and D. Yang. A stress integration algorithm for plane stress elastoplasticity and its applications to explicit finite element analysis of sheet metal forming processes. *Computers & Structures*, 66:301–311, 1998.

[48] G. Li, M. Tan, and K. Liew. Three-dimensional modeling and simulation of superplastic forming. *Journal of Materials Processing Technology*, 150:76–83, 2004.

[49] J. Libby and T. Ruf. The material distribution in a realistic VELO design. Technical report, CERN, 2001. LHCb 2001-019 VELO.

[50] J. Lin and T. Dean. Modelling of microstructure evolution in hot forming using unified constitutive equations. *Journal of Materials Processing Technology*, 167:354–362, 2005.

[51] S. Luckey Jr., P. Friedman, and K. Weinmann. Correlation of finite element analysis to superplastic forming experiments. *Journal of Materials Processing Technology*, 194:30–37, 2007.

[52] J. MacFarlane. VISRAD- a 3-D view factor code and design tool for high-energy density physics experiments. *Journal of Quantitative Spectroscopy & Radiative Transfer*, 81:287–300, 2003.

[53] R. Mahidhara and A. Mukherjee. Mechanisms of cavity growth in a fine-grained 7475 al superplastic alloy. *Materials and Design*, 16(6):343–348, 1995.

[54] K. Mattiasson and M. Sigvant. An evaluation of some recent yield criteria for industrial simulations of sheet forming processes. *International Journal of Mechanical Sciences*, 2007.

[55] M. Meier. The Hall-Petch relationship. Department of Chemical Engineering and Materials Science, University of California, Davis, September 2004.

[56] F. Mohamed. The role of boundaries during superplastic deformaton. *Surface and Interface Analysis*, 31:532–546, 2001.

[57] F. Mohamed. The role of impurities during creep and superplasticity at very low stresses. *Metallurgical and Materials Transactions A*, 33(2):261–278, 2002.

[58] R. Myers and D. Montgomery. *Response Surface Methodology: Process and Product Optimization Using Designed Experiments*. Wiley, 2nd edition, 2002.

[59] T. Naka, Y. Nakayama, T. Uemori, R. Hino, and F. Yoshida. Effects on temperature on yield locus for 5083 aluminium alloy sheet. *Journal of Materials Processing Technology*, 140:494–499, 2003.

[60] A. Needleman. An analysis of ductile rupture in notched bars. *J. Mech. Phys. Solids*, 32(6):461–490, 1984.

[61] K. Padmanabhan. On the evaluation of the activation energy for superplastic flow. *Journal of Materials Science*, 16(2):531–533, 1981.

[62] K. Padmanabhan, R. Vasin, and F. Enikeev. *Superplastic Flow: Phenomenology and Mechanics*. Springer, 2001.

[63] R. Peerlings. Plasticity of porous materials. EM Graduate Course Micromechanics, Ch11, 2004.

[64] J. Pilling. Superplasticity in Crystalline Solids, from http://home.comcast.net/∼brandihampson/sp/index.html. Technical report, Michigan Technological University.

[65] J. Pilling, N. Ridley, and M. Islam. On the modelling of diffusion bonding in materials: superplastic super alpha-2. *Materials Science and Engineering A*, 205:72–78, 1996.

[66] A. Pye. Superplastic forming of aluminium alloys. *Materials & Design*, 2(6):304–309, 1981.

[67] N. Queipo, R. Haftka, W. Shyy, T. Goel, R. Vaidyanathan, and P. Tucker. Surrogate-based analysis and optimization. *Progress in Aerospace Sciences*, 41:1–28, 2005.

[68] A. Ragab. Modeling the effect of cavitation on tensile failure of superplastic alloys. *Materials Science and Engineering A*, 454-455:614–622, 2007.

[69] N. Ridley, P. Bate, and B. Zhang. Material modelling data for superplastic forming optimisation. *Materials Science and Engineering A*, 410:100–104, 2005.

[70] S. Semiatin, V. Seetharaman, et al. Cavitation during hot tension testing of Ti-6Al-4V. *Materials Science and Engineering A*, 256:92–110, 1998.

[71] V. Senthil Kumar, D. Viswanathan, and S. Natarajan. Theoretical prediction and FEM analysis of superplastic forming of AA7475 aluminium alloy in a hemispherical die. *Journal of Materials Processing Technology*, 173:247–251, 2006.

[72] J. Simo and T. Hughes. *Computational Inelasticity*. Springer-Verlag, 1998.

[73] Simulia. *ABAQUS Analysis User's Manual*. 2007.

[74] Simulia. *ABAQUS Theory Manual*. 2007.

[75] Simulia. *ABAQUS User Subroutines and Parametric Studies*. 2007.

[76] W. Soer, A. Chezan, and J. De Hosson. Deformation and reconstruction mechanisms in coarse-grained superplastic almg alloys. *Acta Materialia*, 54:3827–3833, 2006.

[77] W. Swann. A survey of non-linear optimization techniques. *FEBS Letters*, 2:S39–S55, 1969.

[78] C. Syn, M. O'Brien, D. Lesuer, and O. Sherby. An Analysis of Gas Pressure Forming of Superplastic AL 5083 Alloy. *LIMAT-2001 Int'l Conference on Light Materials for Transportations Systems*, (UCRL-JC-135190), May 2001.

[79] D. Tabor. *Gases, liquids and solids*. Cambridge, 2nd edition, 1985.

[80] W. Tsai, Y. Hwu, C. Chen, L. Chang, J. Je, H. Lin, and G. Margaritondo. Grain boundary imaging, gallium diffusion and the fracture behavior of Al-Zn Alloy - An in situ study. *Nuclear Instruments and Methods in Physics Research B*, 199:457–463, 2003.

[81] R. Valiev and O. Kaibyshev. On the quantitative evaluation of superplastic flow mechanisms. *Acta Metallurgica*, 31(12):2121–2128, 1983.

[82] R. Vasin, F. Enikeev, M. Mazurski, and O. Munirova. Mechanical modelling of the universal superplastic curve. *Journal of Materials Science*, 35:2455–2466, 2000.

[83] R. Verma, A. Ghosh, S. Kim, and C. Kim. Grain refinement and superplasticity in 5083 Al. *Materials Science and Engineering A*, 191:143–150, 1995.

[84] W. Williams. *Nuclear and Particle Physics.* Oxford Science Publications, 1997.

[85] H. Xing, C. Wang, et al. Recent developments in the mechanics of superplasticity and its applications. *Journal of Materials Processing Technology*, 151:196–202, 2004.

[86] J. Yoon, F. Barlat, R. Dick, K. Chung, and T. Kang. Plane stress yield function for aluminum alloy sheets - Part II: FE formulation and its implementation. *International Journal of Plasticity*, 20:495–522, 2004.

[87] J. Yoon, D. Yang, and K. Chung. Elasto-plastic finite element method based on incremental deformation theory and continuum based shell elements for planar anisotropic sheet materials. *Comput. Methods Appl. Mech. Engrg.*, 174:23–56, 1999.

[88] H. Young and R. Freedman. *University Physics.* Addison Wesley, 9th edition, 1996.